RICE UNIVERSITY

Timescale and Latitudinal dependence of Glacial Erosion Rates from Patagonia and Antarctic Peninsula Tidewater Glaciers (46°-65° S)

by

Rodrigo Alejandro Fernandez-Vasquez

A THESIS SUBMITTED
IN PARTIAL FULFILLMENT OF THE
REQUIREMENTS FOR THE DEGREE

Doctor of Philosophy

APPROVED, THESIS COMMITTEE

John Anderson
W. Maurice Ewing Professor in Oceanograpy, Department of Earth Science

Dale Sawyer
Professor, Department of Earth Science

Brandon E. Dugan
Assistant Professor, Department of Earth Science

Philip Bedient
Herman Brown Professor of Engineering, Dept of Civil and Environmental Engineering

HOUSTON, TEXAS
November 2011

Abstract

Timescale and Latitudinal dependence of Glacial Erosion Rates from Patagonia and Antarctic Peninsula Tidewater Glaciers (46°-65° S)

by

Rodrigo Alejandro Fernandez-Vasquez

I use time-constrained sediment volumes delivered by glaciers calving into Marinelli Fjord (55°S), an outlet glacier of the Cordillera Darwin Ice Cap, Southern Patagonia, to determine erosion rates across different timescales. These results indicate that modern sediment yields and erosion rates from temperate tidewater glaciers can exceed long-term values over the time of deglaciation after the LGM (centennial and millennial time scales) by up to two orders of magnitude. In northern Patagonia (Gualas glacier area, 46.5°S), an overall increase in sediment production in the late Holocene is interpreted as result of a sharp increase in centennial timescale precipitation (intensified westerly winds).

Erosion rates values span two orders of magnitude from 0.03 mm/yr for Lapeyrere Bay at Anver Island (~64.5°S), up to 1.09 mm/yr for San Rafael glacier at northern Patagonia (~46.5°S). Rates from the Antarctic Peninsula glaciers are in general lower than the temperate Patagonian glaciers. A good correlation of erosion rates and modern (estimated sea level annual 1970 temperature) sea level annual temperature was found.

Latitudinal decrease of millenial <Er> is interpreted as result of decreasing annual temperature although decreasing in annual precipitation is suggested. The pattern of thermochronology ages from other studies (Thompson et al., 2010; Guenthner et al., 2010), along with the values of 10^3 and 10^6 years timescales erosion rates from this study, indicate that long-term glacial erosion decreases significantly its efficiency with latitude, implying that long-term glacial cover acts as a protective blanket, hindering erosion and allowing mountain growth.

We conclude that the pattern of erosion rate decrease with timescale reflects the sensitivity of glaciers to climate variability. Temperate glaciers have higher sensitivity and greater response amplitude to climatic stress than subpolar or polar glaciers. This results in a decrease in erosion rates (sediment production) with latitude, and also in a decrease of erosion rate gradients with timescale.

Acknowledgments

I would like to thank my advisor Dr. John Anderson for his support and guidance during my time at Rice. I want to thanks also those who served on my thesis and proposal committees, including Dr. Dale Sawyer, Dr. Brandon Dugan, Dr. Andre Droxler, Dr. Jerry Dickens and Dr. Philip Bedient.

I am very grateful of the many co-workers and friends that helped me to carry to a good end my endeavour at Rice. Many thanks to my friends Lizette Leon-Rodriguez, Maximiliano Bezada, Karem Lopez, Davin Wallace, Becky Minzoni, Alex Kirshner, Travis Stolldorf, Winnie Yu, Bora Song and Ulyana Horodyskyj. My friends Sarita Martinez and Nicholas Voronov gave me great support and the feeling of having the comfort of a family which was invaluable during my early years in US. I would like to give special thanks to all the supportive staff of the Rice University Earth Science Department: Soookie Sanchez, Mary Ann Lebar, Pat Jordan, Roger Romero, Sandra Flechsig, Bonnie Hoffman and Lee Willson.

Nothing would have been possible without the unconditional support of my wife Mariela Gonzalez and my parents Benito Fernandez and Miriam Vasquez, to whom I dedicate this work.

As always and ever, I thank the Tao, Zen and AIKIDO.

Contents

List of Figures

Chapter 2

Chapter 3

Chapter 4

List of Tables

Chapter 2

Chapter 3

Chapter 4

Chapter 1

Introduction

1.1 Overview

Glaciers play a key role in the coupling between tectonics and climate through a number of processes and temporal/spatial scales, ranging from short-term glacial advances and retreats, millennial-scale glacial cycles to million year-scale orogenies, and global climate changes. In particular, glacier erosion might be a first-order control on mountain range exhumation and isostatic processes through the evacuation and removal of crustal material from orogens and its subsequent transport to continental margins (e.g. Molnar et al., 1990; Montgomery et al., 2001; Blisniuk et al., 2006). Comprehensive compilations of glacier erosion rates have been published recently (Hallet et al., 1996; Elverhøi et al., 1998; Koppes et al., 2009; Delmas et al., 2009). These compilations show that erosion rates vary over several orders of magnitude, that they are generally higher than fluvial erosion rates and suggest that drainage basin area might be a first-order control on their relative magnitude. However, with few exceptions, these estimates are based on modern observations (last few decades) of sediment fluxes, and may not be representative of long-term (centennial, millennial or million-year time scales) trends (Harbor, 1992, 1993; Harbor and Warburton, 1993; Hallet et al., 1996, Delmas et al., 2009).

Most of the sediment produced by modern tidewater glaciers is deposited within fjords and bays, with only minor sediment bypass. This contrasts with the LGM pattern when sediment was delivered by glaciers and ice sheets to the continental shelf and beyond (Powell, 1984; Anderson et al., 2002). The sequestration of sediments within fjords is supported by models and empirical data that show rapid decay in sedimentation rates away from the ice front, (Syvistki 1989; Gilbert et al., 1993; Andrews et al., 1994; and references therein). However, actual sediment accumulation rates within fjords will vary in response to factors such as the relative size of the drainage versus the accumulation basin, the nature of sediment transport (underflow versus overflow, icebergs, turbidity currents etc), local winds, tides, seafloor bathymetry, and marine current circulation patterns. Thus, accumulation rates do not necessarily reflect the nature of the glacial processes involved in the production and delivery of sediments. Sediment yields are calculated from the total volume of sediments deposited over a certain period of time averaged over the area of the drainage basin. Thus, variations in sediment yields do not depend on the processes of sediment transport and deposition. Instead, they can be related directly to properties of glaciers that control erosion and sediment transport (e.g. ice speed, temperature, melting and/or calving rates).

Our results indicate that millennial scale accumulation rates for Patagonian and Antarctic Peninsula glaciers are within the same order of magnitude ($\sim 10^0$ mm/yr) regardless their different thermal state and climate setting. We interpret this as being due to a modulated expression of the so called "Sadler effect" (i.e. accumulation rates are timespan dependent; Sadler, 1999), this is that at millennial timescales the relative proportion of hiatuses vs accumulation periods in the sedimentary section results in

similar (low) accumulation rates. Particularly, in the Antarctic systems, accumulation rates are ~10^0 mm/yr regardless of the time span of deposition (i.e. no "Saddler effect"). This indicates that the same accumulation dynamics (sedimentation versus non deposition or erosion) have dominated the Antarctic fjords and bays at millennial timescales during most of the Holocene. On the contrary, in Patagonia, proximal basins are in general well isolated and have short timescale (decadal-centennial) sedimentary records and high accumulation rates, whereas medial (more distal) basins have millennial scale sedimentary records and low accumulation rates. This produces a noticeable "Saddler effect". We hypothesize that the "Saddler effect" in the accumulation rates from the Patagonian systems is produced because prominent Neoglacial advances and recent post Little Ice Age retreat has left well isolated proximal basins that trap sediments very efficiently, which along with high sediment yields, produces high decadal accumulation rates. There is no such organization of basins in the Antarctic Peninsula fjords and bays and no such clear manifestation of Neoglacial advances or morphologies.

We use time-constrained sediment volumes delivered by glaciers calving into fjords and bays of Patagonia and the Antarctic Peninsula to determine sediment yields and erosion rates across different timescales and a broad latitudinal range. Sediment volumes were derived using a dense grid of high- and low-frequency single channel seismic data and swath bathymetry data along with piston and Kasten cores.

Our results show that erosion rates values span two orders of magnitude from 0.03 mm/yr for Lapeyrere Bay at Anver Island (~64.5°S), up to 1.09 mm/yr for San Rafael glacier at northern Patagonia (~46.5°S). Rates from the Antarctic Peninsula glaciers are in general lower than the temperate Patagonian glaciers. A good correlation of erosion

rates and modern (estimated sea level annual 1970 temperature) sea level annual temperature was found. Latitudinal decrease of millenial <Er> is interpreted as result of decreasing annual temperature although decreasing in annual precipitation is suggested. The pattern of thermochronology ages from other studies (Thompson et al., 2010; Guenthner et al., 2010), along with the values of 10^3 and 10^6 years timescales erosion rates from this study, indicate that long-term glacial erosion decreases significantly its efficiency with latitude, implying that long-term glacial cover acts as a protective blanket, hindering erosion and allowing mountain growth.

The overall conclusion is that the pattern of erosion rate decrease with timescale reflects the sensitivity of glaciers to climate variability. Temperate glaciers have higher sensitivity and greater response amplitude to climatic stress than subpolar or polar glaciers. This results in a decrease in erosion rates (sediment production) with latitude, and also in a decrease of erosion rate gradients with timescale.

1.2 Layout of the thesis

This work is organized in three main chapters (chapters 2, 3 and 4) that correspond to research papers that have been published and/or submitted to peer-reviewed journals. Each chapter contains its own introduction, methods, results, discussion, and conclusions. A general list of references is given after chapter 4. At the end, there are three appendixes (A, B, C) that correspond to material supplementary to each chapter respectively.

Chapter 2 shows the results of a study conducted in Marinelli glacier area (Cordillera Darwin, Southern Patagonia, Chile). This study shows that modern sediment yields and erosion rates from temperate tidewater glaciers can exceed long-term values over the time of deglaciation after the LGM (centennial and millennial time scales) by up to two orders of magnitude. For instance, considering the low exhumation rates of Cordillera Darwin (~0.07 mm/y average for the last 30 Ma), modern erosion rates could be up to three orders of magnitude higher than rates over geological time. This study also suggests that different regions are characterized by different patterns of erosion rate change with time scale, which reflects the sensitivity of glaciers to climate variability.

Chapter 3 shows the result of a study aiming to understand the origine of the Late Holocene increase in sediment fluxes (erosion rates) as indicated by the decrease of erosion rates with timescale found by the study presented in Chapter 2. We focus on the Holocene sedimentary record of Golfo Elefantes in central western Patagonia (46.5°S). Most of the sediment supplied to this gulf is generated by Gualas Glacier and delivered to the gulf by Gualas River. Our data indicates an order of magnitude increase of sediment discharge Golfo Elefantes in the late Holocene (~<1.4-4.3 ka) compared to early Holocene-late Pleistocene (~4.3-11.3 ka). This increased sediment flux is interpreted to represent increased precipitation related to intensification of the westerly winds in the area.

Finally, Chapter 4 shows the results of a study aim to identify first-order control mechanism(s) and magnitude of millennial time scales erosion rates and accumulation rates, comparing glacier-fjord systems across a broad latitudinal transect, from central

Patagonia (46°S) to the Antarctic Peninsula (65°S). The three glacier-fjord areas in Patagonia are San Rafael and Gualas glaciers area (~46.5° S), Europa glacier area (~50.5° S) and Marinelli glacier area (~55° S). In the northern Antarctic Peninsula (<65° S), the studied areas are Maxwell Bay (~62.2° S), Herbert Sound (~64° S) and Lapeyrere and Andvord bays (~64.5° S). The results of this study show that a latitudinal decrease of millenial <Er> which is interpreted as result of decreasing annual temperature (although the decrease in annual precipitation might also be an influential factor). The pattern of thermochronology ages (Thompson et al., 2010; Guenthner et al., 2010), as well as the values of 10^3 and 10^6 years timescales erosion rates from this study, indicate that long-term glacial erosion decreases significantly its efficiency with latitude, implying that long-term glacial cover acts as a protective blanket, hindering erosion and allowing mountain growth as previously suggested by other researchers.

Chapter 2

Timescale dependence of glacial erosion rates, a case study of Marinelli Glacier, Cordillera Darwin, southern Patagonia

Rodrigo A. Fernandez[1], John B. Anderson[1], Julia S. Wellner[2] and Bernard Hallet[3]

[1] Rice University, Earth Science Department, 6100 Main St, MS126, Houston, Texas 77005, USA

[2] University of Houston, Department of Earth and Atmospheric Sciences, Houston, Texas 77204, USA

[3] Department of Earth and Space Sciences and Quaternary Research Center, Box 351310, University of Washington, Seattle, Washington 98195-1310, USA

Published March 2011:

Journal of Geophysical Research-Earth Surface 116, F01020, doi: 10.1029/2010JF001685

Abstract

Erosion rates have been estimated for a number of glaciated basins around the world, mostly based on modern observations (last few decades) of sediment fluxes to fjords. We use time-constrained sediment volumes delivered by glaciers calving into Marinelli Fjord (55°S), an outlet glacier of the Cordillera Darwin Ice Cap, Southern Patagonian Andes in Tierra del Fuego Island, to determine erosion rates across different timescales. Sediment volumes are derived using a dense grid of high- and low-frequency single-channel seismic data and swath bathymetry data along with piston and Kasten cores. Our results show dramatic differences in erosion rates over different timescales. Erosion rates at Marinelli Glacier diminish about 80% (or by factor of ~5) with each ten-fold increase in time span over which erosion rates are averaged: 29.3 mm/yr for the last 45 years, 5.3 mm/yr for the last 364 years and 0.5 mm/yr for the last 12500 years. These results indicate that modern sediment yields and erosion rates from temperate tidewater glaciers can exceed long-term values over the time of deglaciation after the LGM (centennial and millennial time scales) by up to two orders of magnitude. In view of the low exhumation rates of Cordillera Darwin (~0.07 mm/y average for the last 30 Ma), modern erosion rates could be up to three orders of magnitude higher than rates over geological time. We conclude that the pattern of erosion rate changes with time reflects the sensitivity of glaciers to climate variability.

2.1 Introduction

Glaciers have long been recognized as important sculptors of the landscape, especially in mountain ranges where spectacular valleys, fjords and peaks were excavated during glacial stages. They play a key role in the coupling between tectonics and climate through a number of processes and temporal/spatial scales, ranging from short-term glacial advances and retreats, millennial-scale glacial cycles to million year-scale orogenies, and global climate changes. In particular, glacier erosion might be a first-order control on mountain range exhumation and isostatic processes through the evacuation and removal of crustal material from orogens and its subsequent transport to continental margins (e.g. Molnar et al., 1990; Montgomery et al., 2001; Blisniuk et al., 2006).

Erosion rates and associated sediment yields have been estimated for a number of glaciated basins. A comprehensive compilation was given in Hallet et al. (1996) and was updated by Elverhøi et al. (1998), Koppes et al. (2009) and Delmas et al. (2009). With few exceptions, these estimates are based on modern observations (last few decades) of sediment fluxes, and may not be representative of long-term (centennial, millennial or million-year time scales) trends (Harbor, 1992, 1993; Harbor and Warburton, 1993; Hallet et al., 1996, Delmas et al., 2009). According to Koppes and Hallet (2002, 2006), contemporary high sediment yields from tidewater glaciers and associated high erosion rates might be the result of high ice fluxes associated with the retreat of modern glaciers from their last Neoglacial positions. They argue, based on a study of two Alaskan glaciers, that ice flow velocity is proportional to retreat rate, and thus proportional to sediment yields. Furthermore, Koppes and Hallet (2006) proposed that long-term erosion rates could be determined by extrapolating the relationship between short-term erosion

versus retreat rates to the steady state condition of no retreat; in this way they estimated that long-term erosion rates were approximately four times lower than modern values. This approach raises several questions: How accurate is the extrapolation of modern steady state conditions over long-time scales to obtain steady state erosion rates? How different are erosion rates at different time scales? Would this difference be the same for temperate and polar glaciers? To address these questions, observations are required that determine sediment flux over a range of time scales and climate zones. One approach is to examine the volume of sediments deposited in fjords, which are the main repositories for sediments eroded by tidewater glaciers.

Results from sedimentological investigations of subpolar to temperate fjords in Alaska and Greenland, and sub polar fjords in Antarctica, provide a framework for understanding sediment sequestration in fjords (e. g. Powell, 1984; Griffith and Anderson, 1989; Powell and Molnia, 1989; Syvitski, 1989; Gilbert, 1993; Andrews et al., 1994; Domack et al., 1994; Ashley and Smith, 2000). Regardless of the mechanism of sediment delivery to these fjords, the results of these studies indicate that, given certain conditions (shallow sills, up-fjord winds, open marine current influence etc.), most of the sediment produced by modern tidewater glaciers is deposited within fjords and bays, with only minor sediment bypass. This contrasts with the LGM pattern when sediment was delivered by glaciers and ice sheets to the continental shelf and beyond (Powell, 1984; Anderson et al., 2002). The sequestration of sediments within fjords is supported by models and empirical data that show rapid decay in sedimentation rates away from the ice front (Syvistki 1989; Gilbert et al., 1993; Andrews et al., 1994; and references therein). However, actual sediment accumulation rates within fjords will vary in response to

factors such as the relative size of the drainage versus the accumulation basin, the nature of sediment transport (underflow versus overflow, icebergs, turbidity currents etc), local winds, tides, seafloor bathymetry, and marine current circulation patterns. Thus, accumulation rates do not necessarily reflect the nature of the glacial processes involved in the production and delivery of sediments. Sediment yields are calculated from the total volume of sediments produced over a certain period of time averaged over the area of the drainage basin. Thus, variations in sediment yields do not depend on the processes of sediment transport and deposition or any parameter related to the basin morphology. Instead, they can be related directly to properties of glaciers that control erosion and sediment transport (e.g. ice speed, temperature, melting and/or calving rates).

In this paper we present the results of a study conducted in Marinelli fjord, where the tidewater margin of Marinelli Glacier (55°S) exists. Marinelli Glacier is an outlet glacier of the Cordillera Darwin Ice Cap, Austral Andes, Tierra del Fuego Island (Figure 2.2.1). A dense grid of single-channel seismic, swath bathymetry and oceanographic data along with piston and Kasten cores were collected from throughout the fjord. Radiocarbon age-constrained sediment volumes are used to estimate sediment yields and mean erosion rates over a range of timescales. The results show that there are two orders of magnitude difference between modern and millennial erosion rates. The methodology and evaluation of errors are also discussed.

2.2 Regional Background

2.2.1 Physical Setting

Cordillera Darwin (Figures 2.1 and 2.2) is a relatively small range located at the southern end of Tierra del Fuego Island in the Magallanes region of southern Chile. It extends 135 km from Agostini Fjord (west end) to Yendegaia Bay (east end). The average altitude is 612 m a.s.l., but several peaks exceed 2000 m, the highest being Mount Shipton (2488 m a.s.l.) located at the southern end of the Marinelli drainage basin (Figure 2.2).

Large scale weather patterns in the Magallanes region are controlled by the relative position and intensity of the southeastern Pacific Anticyclone and polar front depressions, as well as the orographic effects (Mercer, 1976; Schneider et al., 2003; DGF-CONAMA Professional Report, 2006) of the Southern Patagonian Andes. Climatic records are scanty and discontinuous, especially in the Cordillera Darwin area, but they allow delineation of some general patterns. The dominant wind direction is from the west with less frequent winds from the northwest, southwest and east (Schneider et al., 2003; Santana et al., 2006). Near sea level, weather stations shows similar mean daily temperature patterns throughout the region (Schneider et al., 2003; Santana et al., 2006, 2007), with temperatures varying from 0° to 15° C, indicating a regional control. Annual means range between 5.7° C in the Gran Campo Nevado area to 7° C at Punta Arenas. However, the DGF-CONAMA Professional Report (2006) shows a strong dependence of temperature with altitude. For instance, during the summer temperatures are around 11° C

at the eastern end of the region whereas Cordillera Darwin remains only a couple of degrees above zero. The rest of the year, large areas remain below 0° C, including elevated areas of the cordillera (Figure 2.3).

Precipitation records show a strong orographic pattern with several thousand millimeters of annual precipitation on the western islands of the Patagonian archipelago and only a few hundred millimeters on the lee side of the Southern Patagonian Andes, where precipitation is distributed equally throughout the year (Schneider et al., 2003; Santana et al., 2006, 2007). In the Cordillera Darwin, Porter et al. (2003) reported 1050 mm/year (minimum) at Bahia Pia (Figure 2.2), whereas other nearby locations to the south and to the NNW, such as Hoste and Diablo Islands and Canal Brecknock, have yielded precipitation values of ~1600 mm/yr and 6710 mm/yr respectively (Santana et al., 2006, 2007; Figure 2.2). According to the DGF-CONAMA Professional Report (2006), re-analysis models show that water equivalent precipitation does not show any important inter-seasonal variation (Figure 2.3); annual accumulation estimates average 3000-4000 mm within the Marinelli drainage basin and 4000-6000 mm in high areas of the Cordillera Darwin. Maximum precipitation occurs at the NNW side of the range (Figure 2.3).

2.2.2 Geology

Igneous rocks crop out along the axis of the Southern Patagonian Andes forming the South Patagonian Batholith, whose age spans almost 150 Ma from the Late Jurassic

to the Miocene (Hervé et al., 2000, 2007). Late Paleozoic to Late Triassic metamorphic complexes crop out at the western and eastern sides of the Patagonian Batholith, with only a few smaller and sparse outcrops in the middle (Hervé et al., 2003). The Cordillera Darwin forms the southern extension of the Southern Patagonian Andes. It is composed of a metamorphic basement complex consisting of metasedimentary and some metavolcanic rocks of supposed late Paleozoic to early Mesozoic age (Hervé et al., 1981). These Paleozoic-Mesozoic units are unconformably overlain by a sequence of submarine rhyolitic volcanic and volcanoclastic rocks corresponding to the Late Jurassic Tobifera Formation, which is metamorphosed to the upper amphibolite facies (Cunningham, 1995). Overlying this unit is a sequence of fine- to coarse-grained clastic sedimentary rocks that likely correlate to the Lower Cretaceous Yahgan Formation exposed south of the Cordillera Darwin.

The current drainage basin of Marinelli Glacier is composed of metamorphic basement rocks that are included in the regional unit known as the Eastern Andes Metamorphic Complex (EAMC; Hervé et al., 2003). Some localized outcrops of younger units, such as Late Cretaceous granitoids, occur in the drainage basin of tributary glaciers (SERNAGEOMIN, 1:1000000 Digital Map, 2003). However, during glacial expansions the drainage basin could include lateral valleys where bedrock is composed of acidic volcanic rocks of the Tobifera Formation, and some minor outcrops of the volcanoclastic Yahgan Formation.

With respect to exhumation rates that characterize Cordillera Darwin, relatively few studies have been done. Nelson (1982) estimated "uplift" rates (interpreted by us as exhumation rates) based on cooling histories of several geochronometers (Rb-Sr, K-Ar

and apatite, zircon and sphene fission tracks). This study yielded rates of 0.16-0.21 mm/y for the Late Cretaceous, followed by lower rates during the early Tertiary (0.04-0.2 mm/y), and a very slow average rate for the last 30 Ma (0.05-0.07 mm/y). A recent study by Gombosi et al. (2009) estimated slightly lower exhumation rates for the Oligocene to recent period (0.02-0.05 mm/y).

2.3 Marinelli Glacier Area

2.3.1 Glacial History

Extensive mapping and geochronological work in the Magallanes Region during the last two decades have revealed a complex landscape history since the Last Glacial Maximum (LGM). Clapperton et al. (1995) mapped 5 major moraine systems they believed to represent the last glacial cycle. They named the terminal position of each of these advances 'limit A - E' from distal to proximal with respect to the Patagonian Andes. Recent studies showed that the maximum ice extent during the last glacial cycle was reached at ~23-25 Cal ky BP, corresponding to limit "B" (Figure 2.2.1; McCulloch et al., 2005a, Kaplan et al., 2008). This implies that the Cordillera Darwin Icecap was much more extensive than today, covering most of Tierra del Fuego (e. g. Caldenius, 1932; Clapperton et al., 1995; Rabassa et al., 2000; Glasser et al., 2008). Ice from Marinelli Glacier flowed through the fjord where it merged with ice from Seno Almirantazgo and continued to flow north and east into the Bahia Inútil lobe. A subsequent re-advance of the glaciers in Tierra del Fuego (Advance C) reached its

maximum extent prior to 20 ka and was followed by another late glacial advance (D; Figure 2.2.1) ~17.6 ka whose end marks the beginning of the deglaciation of the region (McCulloch et al., 2005a; Sugden et al., 2005). This was followed by a new and less extensive final Late Glacial advance (E; Figure 2.2.1) that ended ~12 ka (Clapperton, 1995; McCulloch et al., 2005a; Sugden et al., 2005; Kaplan et al., 2008). Several authors have discussed whether or not this last event was in phase with the Younger Dryas or with the Antarctic Cold Reversal (McCulloch et al., 2000; Clapperton C., 2000; McCulloch et al., 2005a,b; Sugden et al., 2005; Kilian et al., 2007; and others).

Boyd et al. (2008) showed that the final retreat of Marinelli Glacier within its fjord occurred ~12.5 ka, and saw no evidence of a re-advance coeval with stage E (Clapperton, 1995; McCulloch et al., 2005a). Further to the north, studies of the Gran Campo Nevado Icecap by Kilian et al. (2007) indicated that Seno Skyring Glacier retreated rapidly around 17.5-15 ka, followed by slower retreat and/or stabilization at ~14 to 11 ka within the fjords.

Ema Glacier to the north and Fiordo Pía to the south are the glaciers closest to Marinelli for which the Holocene Neoglacial history is known. In these areas, a complex history of advance and retreat is evident, with as many as five different neoglacial advances during the last ~6000 years, with three of them being likely synchronous with advances described further to the north for outlet glaciers from the Patagonian Icefields (synchronous(?) advances: 5000-6000?, prior to 3135, ~1300; asynchronous advances: about 695 ^{14}C yrs BP and between 335 and 60 ^{14}C yrs; Strelin et al., 2008; Kuylenstierna et al., 1996). However, there is no direct evidence for these advances having taken place at Marinelli fjord.

Marinelli Glacier has undergone exceptionally rapid retreat during the 20th century (Holmlund and Fuenzalida, 1995). USAF aerial oblique photographs (1945) and early work by DeGasperi (1922; in Porter et al., 2003) show that the Marinelli Glacier front was located at the exposed morainal ridge near the point of convergence between Marinelli and Ainsworth Fjords (Figure 2.4), which is believed to have acted as a grounding line pinning point throughout the Holocene (Boyd et al., 2008). As Marinelli Glacier has been retreating over the last ~50 years, the 1945 ice front location could represent an advanced neoglacial position, possibly related to the Little Ice Age equivalent advances that have been described in other areas of Patagonia (e. g. Clapperton and Sudgen, 1988; Villalba 1994). Koppes et al. (2009) calculated the volume of sediments accumulated over the recently deglaciated fjord (Figure 2.4), and estimated a drainage-basin average erosion rate of ~4 mm/yr over the same period of time.

2.3.2 Depositional Basins

For the purpose of this work we named the series of basins where sediments from Marinelli Glacier are deposited based on their proximity to the glacier: Proximal, Medial and Outer Basin (Figure 2.4).

The Proximal Basin receives sediments directly from Marinelli Glacier, has restricted circulation and is connected to the sea by a few meters deep passage through a morainal ridge resting above a bedrock sill. This feature marks the maximum position of Marinelli Glacier during the last Neoglacial advance (Little Ice Age; Boyd et al., 2008).

The Medial Basin is a broad, 140-150 m deep basin that contains glacimarine sediments deposited during the post-LGM deglaciation. The basin is connected through a series of relatively narrow (<1 km) and shallow (<100 m) passages to the even deeper (~300 m) Outer Basin, where open marine circulation and/or tidal currents influence sedimentary processes (Figure 2.4).

2.4 Methods

Field work was conducted onboard the research vessel RV/IB Nathaniel B. Palmer during the austral fall of 2005. Multibeam swath bathymetry mapping, air gun seismic and chirp sub-bottom profiling, coring, and CTD data (CTD: Conductivity Temperature Depth: required for multibeam calibration) were collected during the cruise. The cores were opened, described and sampled onboard for shells needed for radiocarbon age determination.

Swath bathymetry mapping was conducted using a hull-mounted Simrad EM120 multibeam sonar system consisting of 120 beams using a 12 kHz source. The data were manually edited and processed onboard using the Unix suite MBSystem to remove anomalous beams and to produce real-time plots, working maps and gridded data files. These data were used to help plan core locations and to map the submarine geomorphology.

The seismic survey yielded a dense grid of 3.5 kHz sub-bottom profiler data and single-channel seismic lines. Two hull-mounted sub-bottom profiler systems (Knudsen

and Bathy2000) were used alternatively. The single channel seismic data were collected using a 50 cubic inch air gun coupled with a single-channel streamer. Seismic data were recorded using OYO DAS and Triton Elics data loggers, with minimal processing (bandpass filtering and gain adjustment). Within the Proximal Basin, seismic data were acquired using the Palmer's work boat "Cajun Cruncher", equipped with a 300J boomer and 1000J multi-element sparker and single-channel hydrophone streamer (here after referred to as "CC seismic data").

Thirty two cores including long jumbo piston cores (up to 15m) and short Kasten cores (up to 3m) were taken in the Medial and Outer basins, and in Ainsworth fjord. Core information was used to characterize the glacimarine sediments within the different basins, define units, and determine the age of acoustic units.

Sedimentation rates and the ages for the glacimarine units were estimated using the 31 radiocarbon dates from carbonate samples from the Medial Basin, the Outer Basin and Ainsworth fjord. The results of these analyses are presented by Boyd et al. (2008) and in Appendix A1. The volume of sediments accumulated in the Proximal basin after the retreat of Marinelli Glacier from its 1945 position was estimated from the CC seismic data by Koppes et al. (2009) and corrected in this work with our own parameters (source rock and sediment densities; see next sections).

2.5 Sediment Volume and Erosion Rate Determination

2.5.1 Basic Concepts and Parameters

Sediment volumes for the Medial Basin and Ainsworth fjord were estimated using three seismic data sets; low-frequency air gun, boomer and sparker, and high-frequency sub-bottom (chirp) profiler. Initial work involved mapping key acoustic surfaces. This was followed by the discrete digitization of each surface into equally spaced 3D points (latitude, longitude, time; spacing was ~120 m). Air-gun records comprise the majority of the seismic data used in this study and were collected along parallel lines across the basins and one axial line (Figure 2.4). The high-resolution sub-bottom profiler and CC seismic data were acquired at unequal spacing and used to fill gaps in the air gun seismic data. The seismically derived 3D data points produced the initial dataset for the volume calculation.

Additional 3D data points (latitude, longitude, altitude= 0m) for the sea surface and basement surface were obtained from Landsat TM+ tiles and SRTM digital elevation models at coastline locations. These data were merged with the seismic dataset. Once the final digital dataset was derived, several interpolation methods from the 3D Analyst tool of ArcGis 9.3 were tested to create 3D raster surfaces (pixel size ~50x50m^2) for each seismic surface.

Erosion rates, <Er> (m/yr), averaged over time, t (yr), corresponding to the oldest age of the sediment package, and drainage basin area, A_{dr} (m^2), were derived from sediment volume estimates according to:

(1) $\langle Er \rangle = (1/t)\,(1/A_{dr})\,Vol_{Rx}$, with $Vol_{Rx} = (\rho_{sed}/\rho_{source})\,Vol_{Sed}$

where,

ρ_{sed} = average density of the sediments, (kg/m^3).

Vol_{Sed} = volume of sediments considered, (m^3).

Vol_{Rx} = rock-equivalent volume of sediments, (m^3).

ρ_{source} = estimation of the average density of the source-rocks, (kg/m^3).

Vol_{Sed} corresponds to the geometrical estimate of sediment volume considering only Vp (P-wave velocity) as a control parameter, so it includes porosity. <Er> uses the concept of rock-equivalent volume (Vol_{Rx}), which corresponds to the volume of source rock that equals the mass of the volume of sediments under consideration (Vol_{sed}). Vol_{Rx} is then distributed over the entire drainage basin ($*1/A_{dr}$) and the time span of sedimentation ($*1/t$).

The drainage basin area (A_{dr}) was directly measured from SRTM and Landsat images considering the glaciated and non-glaciated areas that supplied sediments to the glacier during the time span t of deposition of the corresponding unit. The density used for the parental rock (ρ_{source}) was 2700 kg/m^3, which is a common value for metasedimentary and igneous rocks. The density of the sediment and the associated

characteristic p-wave velocity (ρ_{sed} and V_p respectively) were not directly measured, but intervals containing the most probable values were derived from previous studies.

For ρ_{sed} we chose the interval 1600-1800 kg/m^3 according to the values obtained for similar glacimarine sediments by the SHALDRIL project in Maxwell Bay, King George Island, Antarctica (Michalchuk et al., 2010), and the values for marine pelagic and turbidite silty sediments published by Hamilton (1982). Density and Vp data for sediments ranging from silty-clay to clayey-silt (see Appendix A2) are shown in Figure 2.5 (Hamilton, 1971, 1982 and Orsi, 1991). The graph shows that V_p increases with the sediment density following approximately a second order polynomial function; for the interval 1600-1800 kg/m^3 the velocity increases monotonically from 1563 to 1641 m/s. However, considering that this plot contains much less data than presented by Hamilton (1982), where a higher dispersion is observed due to the inclusion of a broader grain size distribution (roughly, velocity varies within a range of ~100 m/s for each density value), we believe that the best velocity estimate for a 1-layer model ranges between 1500-1700 m/s.

2.5.2 Numerical Approximations

In order to evaluate <Er> according to equation (1) using the 3D raster surfaces, we used the following expression:

(2) $Vol_{Sed} = \Sigma_{ij} P_A (D_{ij} - B_{ij})$

where,

P_A = pixel area, (m^2).

D_{ij} = pixel (i,j) depth relative to sea level of the unit boundary estimated from the interpolated seismic data, (m).

B_{ij} = pixel (i,j) depth of the sea floor calculated from the multibeam swath bathymetry survey, (m).

Expanding equation (2) yields:

(3) $Vol_{Sed} = (P_A V_p^{sed} \Sigma_{ij} T_{ij}^{s}) + (P_A V_p^{w} (\Sigma_{ij} T_{ij}^{w}) - P_A (\Sigma_{ij} B_{ij}))$

Where,

T_{ij}^{w} = Pixel (i,j) one-way travel time from sea level to the sea floor, (s).

T_{ij}^{s} = Pixel (i,j) one-way travel time from sea floor to the seismic surface, (s).

V_p^{w} = 1-layer equivalent P-wave velocity of the sea water, (m/s).

V_p^{sed} = 1-layer equivalent P-wave velocity of the sedimentary package considered, (m/s).

Equation (3) shows explicitly the dependence of the volume of sediments contained in a certain unit on the travel times obtained from the seismic profiles. The second term represents the capacity of the interpolation method to mimic the sea floor topography obtained from the swath bathymetry data, and is independent of the depth of the seismic surface that defines a particular sedimentary unit. The first term corresponds to the sediment volume that would be obtained using only seismic data to constrain the boundary surfaces of the unit. Notice that if the interpolation method and the density of

data produce a perfect match between the seafloor surface obtained from seismic and swath bathymetry data, the second term becomes null. V_p^w, was obtained from water column measurements (CTD), or approximated from the seismic profiles by choosing the best value that reproduces the swath bathymetry depths.

To estimate the uncertainty derived from the use of a particular interpolation method to produce the raster seismic surfaces (SS) implicit in equation (3), we tested several methods available in ArcGis 9.3. Our tests indicate that the Spline interpolation with the first derivative added to the curvature minimization criteria is the method that results in more realistic 3D surfaces and that produces the closest volume approximation (see Appendix A3).

2.6 Results

2.6.1 Seismic Units

For the Medial Basin, 68.6 km of seismic lines (Lines 25-33), corresponding to 601 (x,y,time) points (13.6 points/km^2), were interpreted following the Syvitski (1989) terminology. Three units overlie a basin-wide, continuous reflection that marks a sharp decrease in penetration and the end of recognizable stratification. This reflection is interpreted to represent the boundary between sedimentary strata and basement and will be referred as the "acoustic basement". From bottom to top (Figure 2.6) the three units are:

1. A basal unit (GFU, Gravity Flow Unit; Figure 2.6) is composed of high amplitude reflections and transparent layers about ~10m thick, onlapping acoustic basement and prograding toward and infilling topographic lows. The unit is capped by a ~10 m thick conformable layer. The only exception to this description occurs at a couple of proximal small basins next to the bedrock/morainal ridge that separates the Medial and the Proximal basins. There, onlapping basin-fill reflections indicate compaction of the glacimarine deposits. The reflections that onlap acoustic basement are interpreted as gravity flow deposits shed from a morainal bank when ice was grounded there. The ~10 m thick unit above the gravity flow unit might represent a proximal glacimarine layer or distal gravity flow deposits deposited during the retreat of the glacier front.
2. The middle unit (GMU, Glacimarine unit; Figure 2.6) is characterized by high amplitude reflections and transparent layers between 5-10 m thick that onlap the underlying unit. These layers are quasi horizontal in distal areas; closer to the bedrock/morainal ridge, they gradually thicken and dip increasingly toward the basin. The unit is thickest near the center of the basin (~105m) and within proximal small basins, and thins rapidly toward the outer basin. This indicates relatively efficient dispersal and sedimentation within the medial basin. Two subunits of GMU are recognized. They represent proximal to distal glacimarine sedimentation that began just after the retreat of the glacier from the ridge.
3. The youngest unit (HPU, Hemipelagic Unit; Figure 2.6) conformably overlies GMU. The unit is characterized by two high amplitude parallel reflections that follow the smooth topography formed at the end of GMU deposition. These high amplitude reflections bound two subunits with similar thickness (~5m) that are characterized by lower intensity and thinner parallel reflections. This is the only unit that was sampled and dated, and the ages range from 364 cal yr BP to present (Boyd et al., 2008; Appendix A3).

The isopach maps (Figure 2.7) show that GFU is discretely distributed, filling the deeper areas of the basin, indicating gravity flow sedimentation. The overlying unit (GMU) was deposited on smoother topography with more stable and gentle slopes, which, along with settling from suspension, produced a more uniformly distributed sedimentary package. Finally, the youngest unit (HPU) formed on an even smoother sea floor and its draping nature indicates sedimentation from widely dispersed sediment plumes (Figure 2.7). Noticeably, the seismic facies observed in the proximal basin by Koppes et al. (2009), resembles that of SFU and its transition to a GMU mode of sedimentation. This implies that when Marinelli Glacier advances it encounters a smoother basin floor than is assumed by some tidewater glacier models (e. g. Nick et al., 2007; Pfeffer, 2007).

Table 2.1 Evaluation of average erosion rates (<Er>) using equation (1) and the volumes calculated for the medial basin.

Unit	∑ Tij	Vp	Vol	ρ_seds	Vol(Rx)	Total Erosion	Time Span (T)	Sed Load	<Er>	<Er> Error
	[ms]	[m/s]	[m^3]	[kg/m^3]	[m^3]	[m]	[yr]	[m^3(rock)/yr]	[mm/yr]	[mm/yr]
HPU	116057.9	1500	4.2E+08	1600	2.6E+08	0.97	364	7.1E+05	2.66	0.93
GMU	573023.0	1600	2.3E+09	1700	1.5E+09	5.54	12500	1.2E+05	0.44	0.16
GFU	217689.0	1700	9.3E+08	1800	6.2E+08	2.31	100	6.2E+06	23.14	11.57

2.6.2 Erosion Rates

Table 1 shows the basin-wide average erosion rates (<Er>) required to produce the volume of sediment for the three identified units. A relatively small amount of sediments was deposited in Ainsworth Fjord (Figure 2.4) by Marinelli Glacier; they show reflectors that dip and thin away from the moraine that bounds the Proximal Basin. Thus, this volume of sediments, corresponding to about 3% and 4% of the total volume of

GMU and HPU respectively, was added to Vol_{Sed}. For HPU, the age of the sediments (t) was estimated based on sedimentation rates from cores taken in the Medial Basin (radiocarbon ages and sedimentation rates reported by Boyd et al. (2008) and in Appendix A3; sed. Rate = 28 mm/yr, thickness mode= 10.2 m, T = 364.3 yr). For GMU, t was estimated as the age of retreat from the outer part of the medial basin, which is manifested in outer basin cores by a change from ice proximal to ice distal facies at around 12.5 ka (Boyd et al., 2008). To obtain a rough and conservative estimate of the average erosion rate represented by GFU, whose age is unconstrained, we used t = 100 yr, which is twice as long as it took for Marinelli Glacier to retreat the same distance within the proximal basin.

2.6.3 Error Estimate

The standard deviation of the erosion rates obtained when testing the different interpolation methods used to derive the SS 3D raster surfaces is about 8% for HPU and GMU. However, maximum differences in <Er> are at least twice as high. For instance, a difference of ~21% is obtained when comparing the <Er> value obtained using the Spline (Regular) method with the value obtained from the Natural Neighbors or the Triangular Irregular Network method, which normally produced the minimum values. We chose the Spline (tension) method to create isopach maps and to calculate the sediment volumes for two reasons. First, it is the method that best approximates the sea floor topography. Second, this method least underestimates the volumes in question without creating exaggerated artifacts in areas of low coverage.

To estimate the error associated with our erosion rate calculations we used the variation of <Er> as a function of the uncertainty of each parameter involved in its calculation. The uncertainty of each parameter was considered to be the interval of likely values. For HPU, the uncertainty in V_p and sediment density (ρ_{sed}) (see Section 2.5) produces an uncertainty of about 11.7% in <Er>. Uncertainties of 3.4% and 20% are estimated, respectively, for the drainage area and time span (assuming ~20% error in the calculation of the medial basin sedimentation rate). The total uncertainty in <Er> considering these variables is 35% for HPU, which corresponds to 0.93 mm/yr ($<Er>_{HPU}$: 2.66 ± 0.93 mm/yr). For GMU a similar analysis yields a 37% uncertainty for our millennial <Er> ($<Er>_{GMU}$: 0.44 ± 0.16 mm/yr).

2.6.4 Integration of Time Scales

In our volume estimates we have not yet included the sediments deposited within the proximal basin, implying that our <Er> values are minimums. According to Koppes et al. (2009), $3.9x10^8$ m^3 of sediment accumulated in the proximal basin from 1960 to 2005. Using a density of 1800 kg/m^3 for these sediments, $2.60x10^8$ m^3 of rock equivalent sediment was deposited. Hereafter average erosion rates will be designated with a superscript number indicating their respective time span (T). These estimates imply an erosion rate of $<Er>^{45}$= 29 ± 11 mm/yr averaged over a drainage area of ~197 km^2 (the area covered by ice in 1960), for the 1960-2005 period (~37% error; Koppes et al., 2009). Adding this rock equivalent sediment volume to our calculations and using our error estimates, we obtain $<Er>^{364}$= 5.3± 1.9 mm/yr and $<Er>^{12500}$= 0.5± 0.2 mm/yr. Table 2 shows the final results for all the units.

Table 2.2 Results

Unit	Vp [m/s]	ρ_seds [kg/m^3]	A(dr) [Km^2]	Time Span (T) [yr]	Erosion rate [mm/yr]	Error [mm/yr]
PB	1680	1800	197.1	45	29.31	10.84
HPU	1500	1600	266.5	364	5.34	1.87
GMU	1600	1700	267.5	12500	0.52	0.19
GFU	1700	1800	268.5	100	23.14	11.57

2.7 Discussion

2.7.1 Conceptual Model and Limitations

Generally speaking, the calculation of drainage basin-wide erosion rates from sediment volumes relies on three first-order assumptions:

a) The system has been relatively closed since deglaciation and the amount of sediments escaping the fjord is significantly less (one or more orders of magnitude) than the sediment trapped there.

b) It is possible to estimate, with acceptable uncertainty, the amount of sediment deposited in the fjord from sources other than the main glacier, including side valley streams and gravity flows, and sediment delivered to the fjord from outside the basin by marine currents.

c) The change in sediment volume stored under the glacier is small compared to the sediment volume derived from the glacier

The approach is limited by:

a) Our inability to determine temporal and spatial variations in erosion rates within the drainage basin, since we can only calculate erosion rates averaged over specific intervals of deglaciation and over the entire drainage basin.
b) The technical difficulty or inability to sample the layers representing initial glacimarine sedimentation, due to the shallow penetration of our coring techniques; in our case we used the facies change in a different basin (Outer Basin) to estimate the initial retreat and beginning of glacimarine sedimentation in the Medial Basin.

Marinelli Glacier never re-advanced into the Medial Basin after it retreated from its late glacial position 12500 cal yr BP (Boyd et al., 2008). This is in contrast with other glaciers north of the Magallanes region that re-advanced in the late Holocene (e. g. Mercer, 1970; Aniya, 1995; Strelin et al., 2008). This might indicate that particularly favorable conditions (high AAR[1], lowered Equilibrium Line Altitude (ELA), high sediment yields, time etc.; e.g. Nick et al., 2007) would be required for ice to advance into the deep medial basin. Sedimentation rates for Marinelli Glacier pro-glacial basins show a decrease from 28 mm/yr (last ~364 years) in the Medial Basin to about 0.6-0.8 mm/yr (last ~1300 years) in the outer basin. In addition, the proximal basin rates obtained by Koppes et al. (2009), average ~3.5 m/yr for the period 1960-2005. These sedimentation rates indicate that each individual basin has acted as an effective sediment trap during each time span, preventing the escape of sediments to the next basin.

[1] AAR: Accumulation Area Ratio. It is defined as the ratio of accumulation area at the end of the melt season and total glacier area.

The amount of sediment from sources other than Marinelli Glacier is believed to be insignificant since none of the seismic profiles show any prograding wedges (small deltas and fans) along the sides of the fjord. This is consistent with the absence of large streams flowing into side valleys. The only other potential source of sediment to the fjord is Ainsworth Fjord, which currently has a small river at its head. Seismic profiles from Ainsworth Fjord indicate that most of the sediment entering the fjord is trapped there by a prominent sill at the juncture of the two fjords (Figure 2.4). The volume of sediment within the fjord is also small, accounting for less than 4% of the GMU volume of sediments in the medial basin.

Figure 2.8 illustrates how accumulation rates and the Equilibrium Line Altitude (ELA) would vary within the different basins during glacier retreat. High accumulation rates (10^3-10^4 mm/yr) due to frequent turbidity flows and other gravity flows, coupled with glacimarine sedimentation, characterize the proximal setting (Powell, 1984; Syvitski, 1989). The more distal basins are characterized by sedimentation from suspension, with episodic ice-rafting and sediment gravity flows from the steep flanks of the fjord. Sediments are expected to accumulate at rates a couple of orders of magnitude less than in the glacial-proximal setting (10^1-10^2 mm/yr). With continued glacial retreat, accumulation rates and grain size would decrease, although lag deposits may result from winnowing by tidal or oceanic currents. The glacier terminus is likely to linger at pinning points, retreating rapidly between these shallow regions much as it has since the 1960s.

2.7.2 Time-scale Dependence of Erosion Rates

Our results show dramatic differences in erosion rates, depending on the time span considered. The recent decadal erosion rate ($\langle Er \rangle^{45}$= 29.3± 10.8 mm/yr) is 5 times greater than the centennial rate ($\langle Er \rangle^{364}$= 5.34± 1.9 mm/yr) and 56 times greater than the millennial rate ($\langle Er \rangle^{12500}$= 0.52± 0.19 mm/yr). Figure 2.9 shows this difference in the context of the glacial erosion rates compiled by Hallet et al. (1996) and later modified by Koppes and Hallet (2006). The average Marinelli erosion rates for the last 45 years and the last 364 years are comparable to respectively, the modern and "long term" erosion rates estimated for Alaskan glaciers by Koppes and Hallet (2006). Thus, the Koppes and Hallet's (2006) "long term" erosion rates, which were derived assuming a steady state condition (no retreat) of the glaciers, are limited to the last glacial event (Little Ice Age). Erosion rates over longer time scales would include previous glacial cycles and periods of decreased ice extent, leaving them out of the scope of calculations based on recent glacial behavior. In this sense, the millennial scale (T=12500 yr) erosion rate of 0.52± 0.19 mm/yr represents an average over a variety of glacial conditions (percentage of glaciated area, mass balance, calving rate etc.) characterizing the longer period since glacier retreat from the Medial Basin. This erosion rate falls within the range of values of the "Global Glaciers" group from Hallet et al. (1996; Figure 2.2.10) suggesting that the glaciers within this group have in general a low erosion capacity compared with temperate Alaskan glaciers and Marinelli Glacier.

Several aspects of the dataset presented by Hallet et al. (1996) are intriguing. Figure 2.9 shows that within each geographical group of glaciers there is little correlation of erosion rates with drainage basin area as suggested by the overall dataset. Instead, as

other researchers have noted (e.g. Burbank, 2002), other factors such as the geological/geographical setting, climate, and relief should be more important, given the variety of glaciers included in the dataset. Furthermore, a detailed examination of the data raises the question of whether a simple comparison of diverse datasets is justifiable in view of the remarkable variety of methodologies used to determine erosion rates, and their influence on the results (Delmas et al., 2009). Other reasons include the lack of error estimates, the different time scales involved, the differences in the percentage of glacial cover and even the scope of the original studies (some of them measure sediment yields from an individual glacier whereas others include periglacially derived sediments).

Guided by our results for Marinelli Glacier, we propose that it would be instructive to present erosion rate data, in general, as function of the time scale over which the rates are averaged. Thus, if Er= f(t), then $\frac{1}{T}\int_0^T Er(t)\,dt$ represents the average erosion rate for the last T years over a certain area. Depending on the magnitude of T, this average erosion rate will include portions of, or a number of glacial cycles and variable degrees of glacierization. As T approaches million year time scales, we would expect values that compare with thermochronologicaly-derived exhumation rates for areas where tectonic exhumation is relatively small.

Figure 2.2.10 shows <Er> vs T for Marinelli Glacier and other glaciers where average erosion rates have been calculated by similar methods. Glaciers included in Figure 2.2.10 and Table 3, were monitored over periods longer than 30 years in order to have records that average out inter-annual natural variations. We have also selected only data generated by studies of basin-wide bedrock glacier erosion rather than sediment

erosion or local, site-specific erosion rates, and in which the methodology was presented with some detail. The "long term" erosion rates for Alaskan glaciers were derived from Koppes and Hallet (2006). The corresponding time span was arbitrarily calculated as T=10*T' in order to use a T value one order of magnitude higher than the original monitored time. In this way, we approximate centennial time-spans from the original decadal observations keeping constant the relative erosion rates and magnitudes (Table 3). This ten-fold arbitrary increase in time-spans is based on the assumption that the "long term" Alaskan rates estimated by Koppes and Hallet (2006) seem to represent the last centuries of glacial advance and retreat related to the Little Ice Age.

In general, average erosion rates diminish non-linearly with increasing time-span (Figure 2.2.10; Table 3). This is clearly shown for the only three areas (including this study) where erosion rates at different time scales have been estimated. For Marinelli Glacier, a power function relates <Er> and T:

(4) $\langle Er \rangle = 403\ T^{-0.71}$ where $\langle Er \rangle = 1/T \int_0^T Er(t)\ dt$

This means that with each ten-fold increase in time, <Er> should diminish about 80% (or by factor of 5.1). For example, a rate of 0.58 mm/yr for the last 10,000 yr would be only about 0.11 mm/yr for the last 100,000 years. Similar power law relations were found for Isfjorden and Kongsfjorden glaciers in Svalbard (Elverhøi, 1995, 1998), but <Er> are less sensitive to timescale (Figure 2.2.10). For these glaciers, a ten-fold increase in time span diminishes <Er> about 45% and 55%, corresponding to reductions by factors of 1.8 and 2.2 respectively. This is less than half the reduction observed at Marinelli Glacier. Thus, in Figure 2.2.10 where the X and Y axes are in log scale, the

power laws showing the variation of <Er> through time for Marinelli and Svalbard glaciers are represented by lines whose slopes (∂Log(<Er>)/∂Log(T)) provide a measure of how sensitive <Er> is to changes in the time scale under consideration.

The short term – long term pattern of erosion rates estimated for Alaskan glaciers (Figure 2.2.10; $<Er>_{Ak} = 94.41*T^{-0.42}$) is strikingly similar to that of Marinelli Glacier, both in terms of magnitude and gradient (∂Log(<Er>)/∂Log(T)). This could be caused, in part, by our somewhat arbitrary estimate of the duration of the interval represented by the long-term values provided by Koppes and Hallet (2006). However, variations of the multiplicative factor applied to make this estimation have a minimum effect on <Er> or the ∂Log(<Er>)/∂Log(T) ratio; for example if this factor varies within the interval (2 to 20). <Er> would decrease with T between 58-65% (corresponding to reduction factors between 2.4-2.9; see Appendix A4), which is still higher than the corresponding Svalbard values. Hence, in the following sections we will assume that the factor 10 in estimating the long-term timescale for the Alaskan glaciers results in a reasonable estimate of the pattern of variation of $<Er>_{Ak}$ through time.

Marinelli and the Alaskan glaciers, all temperate glaciers, also have higher <Er> values than those for Svalbard's subpolar glaciers at any timescale, converging over the long term and diverging by about two orders of magnitude in the shortest time span, three decades. The lower erosion rates associated with Svalbard glaciers are not surprising given the lower temperatures, precipitation and slope. However, the steeper log-slope of the temperate glaciers (Figure 2.2.10) implies that their erosion rates have increased in recent times faster than those of the subpolar glaciers of Svalbard since the beginning of the deglaciation. As some geological and geomorphological variables controlling glacier

erosion rates remain constant during deglaciation (e.g. bedrock lithology, fracture systems, subglacial topography etc.), this would imply a net increase in the effectiveness of glacier erosion processes related to glaciological variables such as ice dynamics, ice temperature, water availability, mass balance etc.. As these variables depend strongly on climate, which has varied in a complex pattern throughout the Holocene, these temperate glaciers have been more responsive to climate/ocean changes. In particular, if glacier erosion correlates with retreat rate, as Koppes et al. (2002, 2006) have recently suggested, the effectiveness of erosion by these temperate glaciers during the Late Holocene could be related to enhanced retreat rates and the number of neoglacial oscillations. One implication is that in Antarctica, where low ice temperatures and no significant neoglacial advances have been documented within fjords (Michalchuk et al., 2010), lower erosion rates and slope (∂Log(<Er>)/∂Log(T)) values are expected. Our preliminary estimates for the Antarctic Peninsula, which are based on the seismic stratigraphic work of Smith and Anderson (2010), show that rates of 0.05 mm/yr characterize the last 9.5 Ma (Figure 2.2.10). By extrapolation, rates for the late Pleistocene-Holocene deglaciation are within the range of 0.05-0.1 mm/yr.

Finally it is important to note that the data discussed here apply only to the late Pleistocene-Holocene deglaciation for which the chronology, geomorphology and glacial history of the study areas are relatively well constrained. Studies that address a wider variety of environments and timescales are necessary to clarify the time-dependent nature of glacial erosion. Determinations of glacial erosion rates in glaciated mountain ranges that deliver sediment directly to continental shelves are necessary to estimate million-

year scale erosion rates that include several full glacial cycles and time scales comparable to those of tectonic processes.

2.8 Conclusions

The volumes of sediment accumulated in Marinelli fjord since the LGM (Figure 2.5) yield erosion rates over a range of timescales spanning three orders of magnitude. In fjords with distinct, poorly connected basins, such as Marinelli fjord, each basin retains a sedimentary record spanning the time since the beginning of its deglaciation (Figure 2.8). Erosion rates associated with Marinelli Glacier diminish about 80% with each ten-fold increase in the time span over which rates are averaged: ~29.3 mm/yr for the last 45 years, ~5.3 mm/yr for the last 364 years and ~0.5 mm/yr for the last 12500 years. These results indicate that modern sediment yields and erosion rates from temperate tidewater glaciers can exceed long term values over the time of deglaciation (centennial and millennial time scales) by up to two orders of magnitude, and by up to three orders of magnitude for geological time scales (millions of years).

Average erosion rates in the Marinelli fjord drainage basin are approximated by the power law: $\langle Er \rangle = 402.78 * T^{-0.71}$; where $\langle Er \rangle = (1/T) * {}_0^T\int f(t)\, dt$. Similar power law dependence of <Er> with time-span "T" are associated with subpolar glaciers of Svalbard (Elverhøi, 1995, 1998). When erosion rate data are examined in a log-log plot, the slope (∂Log(<Er>)/∂Log(T)) gives an indication of the time average enhancement of glacial erosion in recent times. As erosion rate correlates with retreat rate (Koppes 2002, 2006),

we hypothesize that high ∂Log(<Er>)/∂Log(T) ratios could be related to enhanced retreat/advance rates and/or the number of neoglacial cycles experienced in any particular region during the Late Holocene. As the regional behavior of glaciers relates closely to climate and oceanographic conditions, ∂Log(<Er>)/∂Log(T) ratios ultimately reflect their sensitivity to regional climatic and oceanographic changes. Thus, in addition to lower values of <Er> at any given time span "T", polar regions such as Antarctica, where there is no evidence of widespread neoglacial advances, should have very low ∂Log(<Er>)/∂Log(T) ratios. In contrast, temperate regions, which more likely experienced a number of neoglacial advances, should have high <Er> values and high ∂Log(<Er>)/∂Log(T) ratios. Thus, temperate glacial settings will experience faster denudation rates at the time scale of glacial cycles.

2.9 Acknowledgements

This research was funded by the National Science Foundation, Office of Polar Programs grant number NSF/OPP 03-38137 to John Anderson and Julia Wellner, and grant NSF/OPP 03-38371 to Bernard Hallet. We thank the officers, crew, and scientist who sailed on the RV/IB Nathaniel B. Palmer during NBP05-05 in the Chilean Fjords. We would also like to thank the Instituto Antártico Chileno (INACH) for their support in obtaining permission to work in Chilean fjords. Lastly, we would like to thank Michele Koppes for insightful discussions of this work.

Table 2.3. Erosion rates and time span dataset (see Figure 2.10).

Location	Time Span [yr]	<Er> [mm/yr]	Reference
Marinelli	45	29.31	This study
Marinelli	364	5.34	This study
Marinelli	12500	0.52	This study
Vestfjorden, Norway	23500	1.70	Laberg et al, 2009
NE Scotland	2300000	0.03	Glasser & Hall, 1997
Kongsfjorden, Svalbard	30	0.87	Elverhøi, 1998
Kongsfjorden, Svalbard	9600	0.12	Elverhøi, 1998
Kongsfjorden, Svalbard	2900	0.20	Elverhøi, 1998
Kongsfjorden, Svalbard	8300	0.09	Elverhøi, 1998
Kongsfjorden, Svalbard	10400	0.14	Elverhøi, 1998
Isfjorden, Svalbard	2500	0.40	Elverhøi, 1995
Isfjorden, Svalbard	10000	0.25	Elverhøi, 1995
Isfjorden, Svalbard	13000	0.28	Elverhøi, 1995
Spitsbergen, Svalbard	9600	0.02	Svendsen, 1989
SE Alaska	33	45.22	Jordan, 1962[1]
SE Alaska	35	12.01	Powell, 1991[1]
SE Alaska	54	16.71	Molnia, 1985[1]
SE Alaska	80	15.99	Stravers and Syvitski, 1991[1]
SE Alaska	86	6.03	Merrand, 1994[1]
SE Alaska	87	47.24	Cai, 1994[1]
SE Alaska	700	13.71	Carlson, 1989[1]
SE Alaska_long term	330	11.31	after Koppes et al, 2006
SE Alaska_long term	350	3.00	after Koppes et al, 2006
SE Alaska_long term	540	4.18	after Koppes et al, 2006
SE Alaska_long term	800	4.00	after Koppes et al, 2006
SE Alaska_long term	860	1.51	after Koppes et al, 2006
SE Alaska_long term	870	11.81	after Koppes et al, 2006
SE Alaska_long term	7000	3.43	after Koppes et al, 2006
Exhumation rate C. Darwin	1000	0.05	Nelson, 1982
Iceland (SW-W-N)	10200	0.06	Geirsdotir, 2007
Western Antarctic Peninsula	2900000	0.05	Tyler, 2009
Western Antarctic Peninsula	5260000	0.05	Tyler, 2009
Western Antarctic Peninsula	9450000	0.05	Tyler, 2009
Exhumation rate C. Darwin	30Ma	0.05-0.07	Nelson, 1982

[1]Data from *Hallet et al.* [1996]. Long term erosion rates for Alaskan glaciers were calculated using data corrected according to *Koppes et al.* [2006], which involves dividing each value by a factor of 4, and considering 10 times the published time span (T'=T*10).

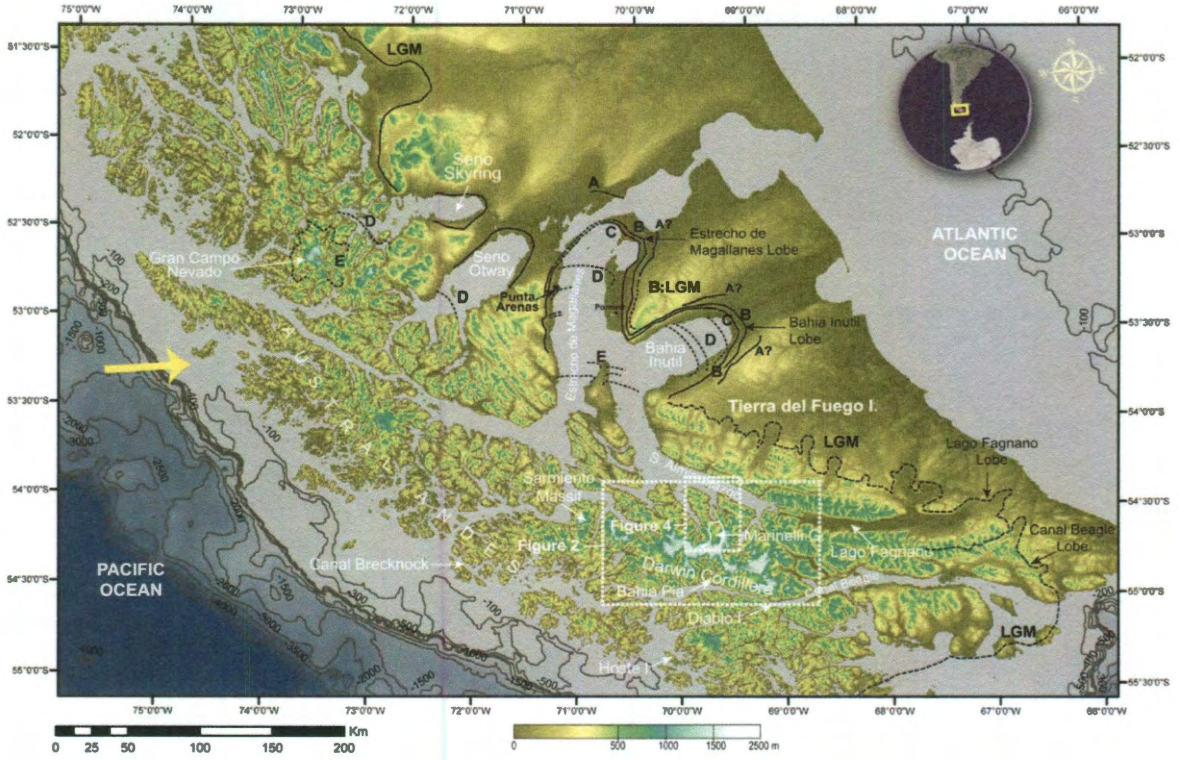

Figure 2.1 Relief of the Magallanes region showing the location of Cordillera Darwin (larger rectangle), Marinelli Glacier area (smaller rectangle) and main glacial limits (based on Marden, 1997, Coronato, 1999, Mc Culloch, 2005, Kaplan, 2007, Kilian, 2007, and Glasser 2008). LGM limit is indicated by thick black line and roughly corresponds to limits B and C mentioned in the text. Dashed lines indicate late glacial advances D and E. The yellow arrow indicates the mean wind direction (westerlies). Relief is based on a SRTM derived DEM (90x90m; geo. projection: South America Conic Conformal, South America 1956). Bathymetry is based on GEBCO (2003) data for the region with 100m (<-500m) and 500m (>-500m) contour intervals.

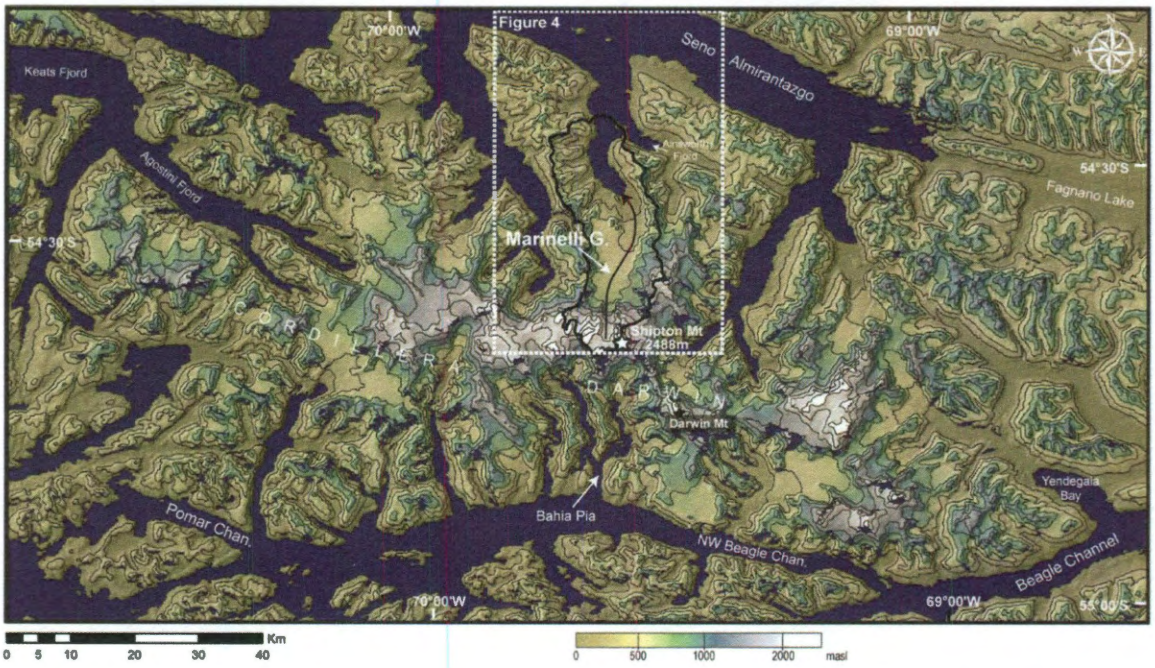

Figure 2.2 Cordillera Darwin relief and drainage basin area of Marinelli Glacier for the last neoglacial advance (Little Ice Age). Peaks above 2000m are shown in white. Contours are every 250m. The arrow indicates the approximate central axis of Marinelli Glacier for reference. The relief is based on a SRTM derived DEM (90x90m; geo. projection: Mercator UTM 19S, WGS1984).

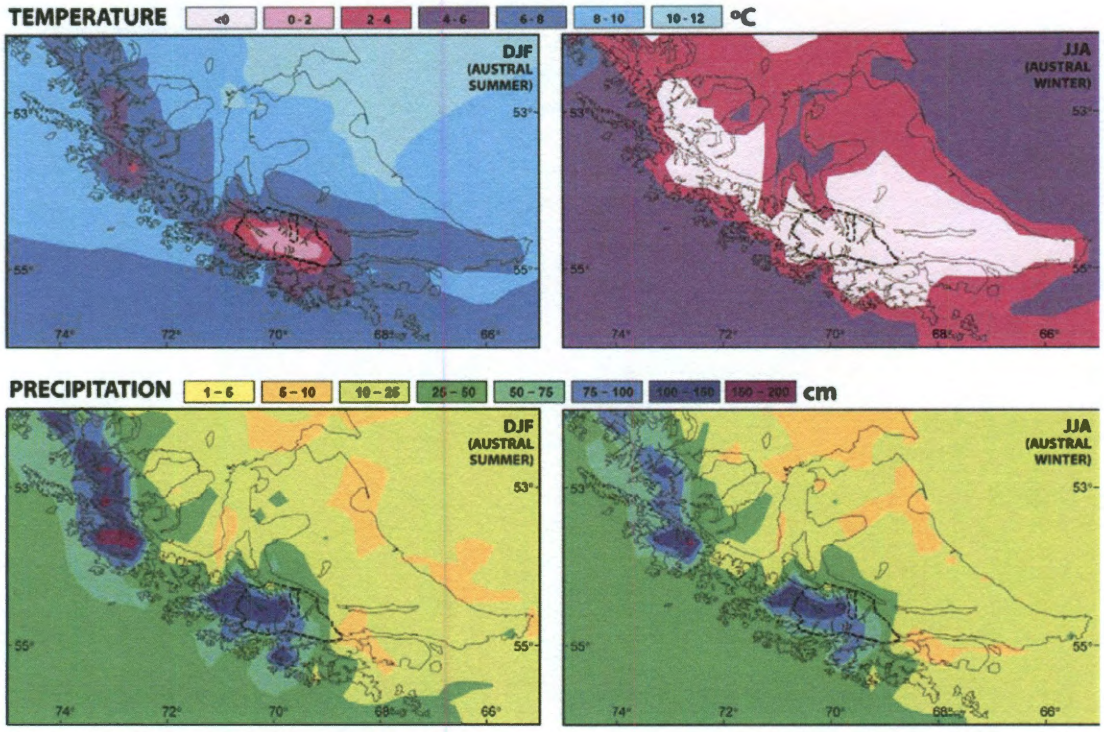

Figure 2.3 Climate images generated using PRECIS model showing temperature and precipitation for the Magallanes region (modified from DGF, 2006). Three-month averages for the austral summer and winter are shown. Temperature for the rest of the months stays below zero at the central Cordillera Darwin (not shown). Precipitation shows no important variation through the rest of the year.

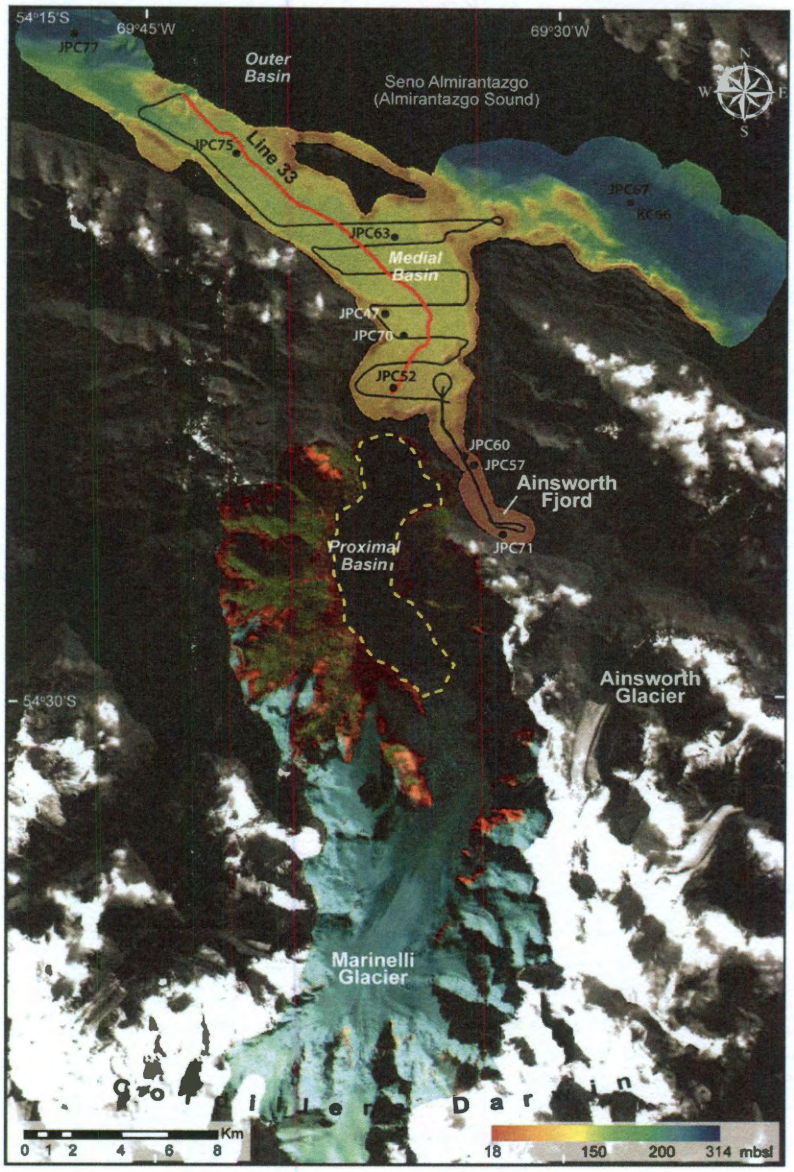

Figure 2.4 Marinelli Glacier area. The drainage basin area, considered for the centennial and millennial scale erosion rates calculations (266.52 km2; see text for details), is shown in RGB colors (Landsat TM (8,5,3). Areas covered by vegetation appear in green, bare rock in reddish colors, snow in light blue and ice in dark blue. Swath bathymetry is shown for the areas covered by the survey (Medial and part of the Outer Basin). The figure shows the area recently exposed by ice retreat (~1960; Marinelli Fjord) and termed "Proximal Basin" for the purpose of this study (dashed yellow line); this area was study by Koppes (2009). The figure also shows the location of the cores used to estimate accumulation rates (black dots) and the air-gun seismic lines (continuous lines) used to estimate sediment volumes. Line 33 (see Figure 2.6) is shown in red. Map is projected on UTM 19S (WGS1984).

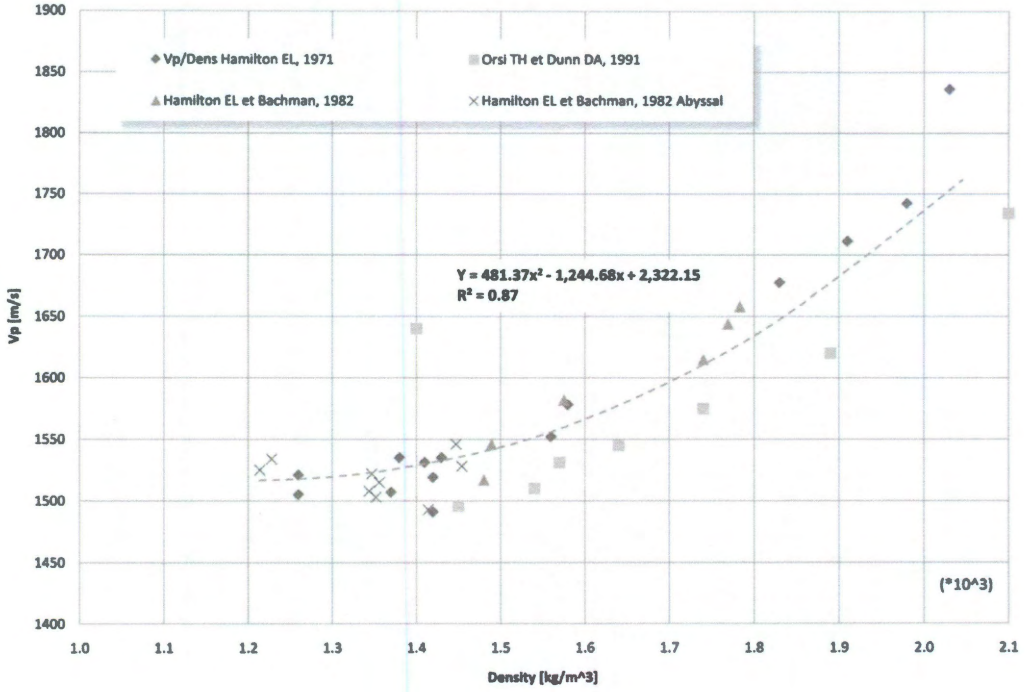

Figure 2.5 P-wave velocity relative to densities for silty marine sediments based on data from several authors.

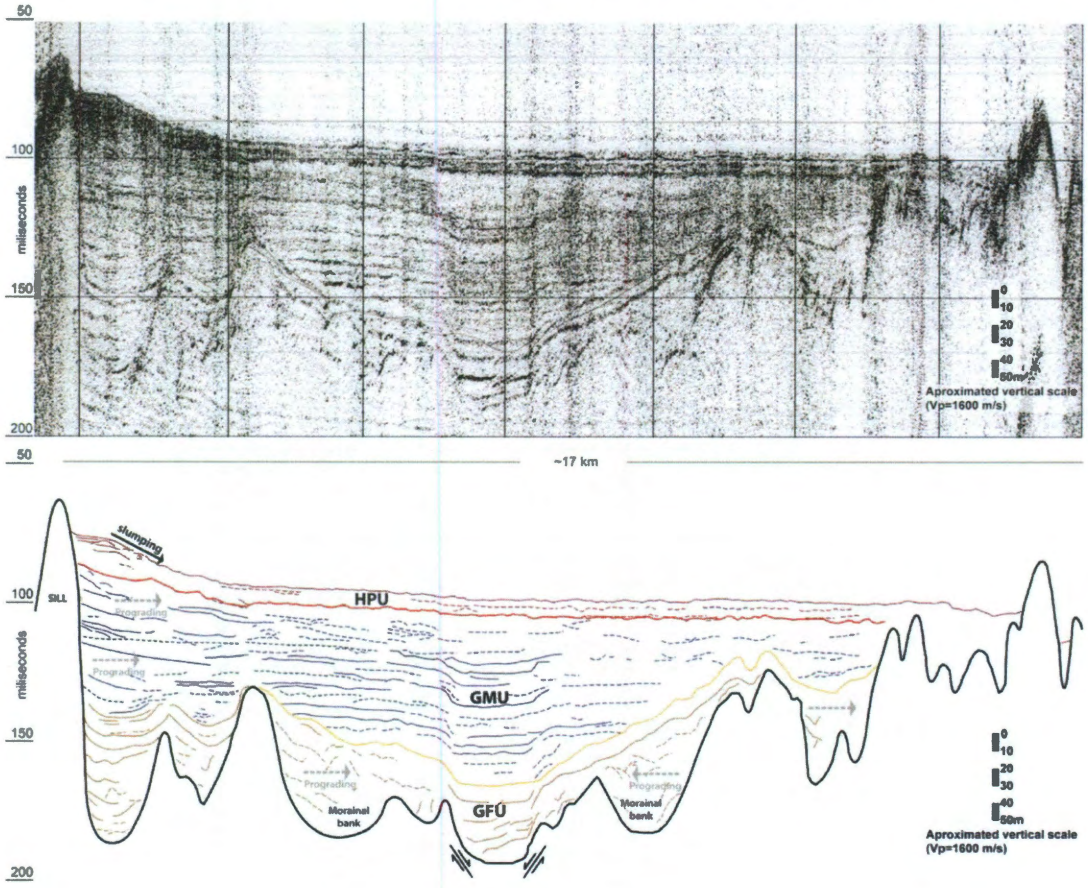

Figure 2.6 Interpretation of seismic Line 33 (Figure 2.4, red line), which goes along the axis of the Medial Basin. GFU (Gravity Flow Unit): gravity flow deposits (Morainal bank?), GMU (Glacimarine Unit) composed of proximal to distal glacimarine sediments, and HPU (Hemipelagic Unit), composed of recent hemipelagic sediments.

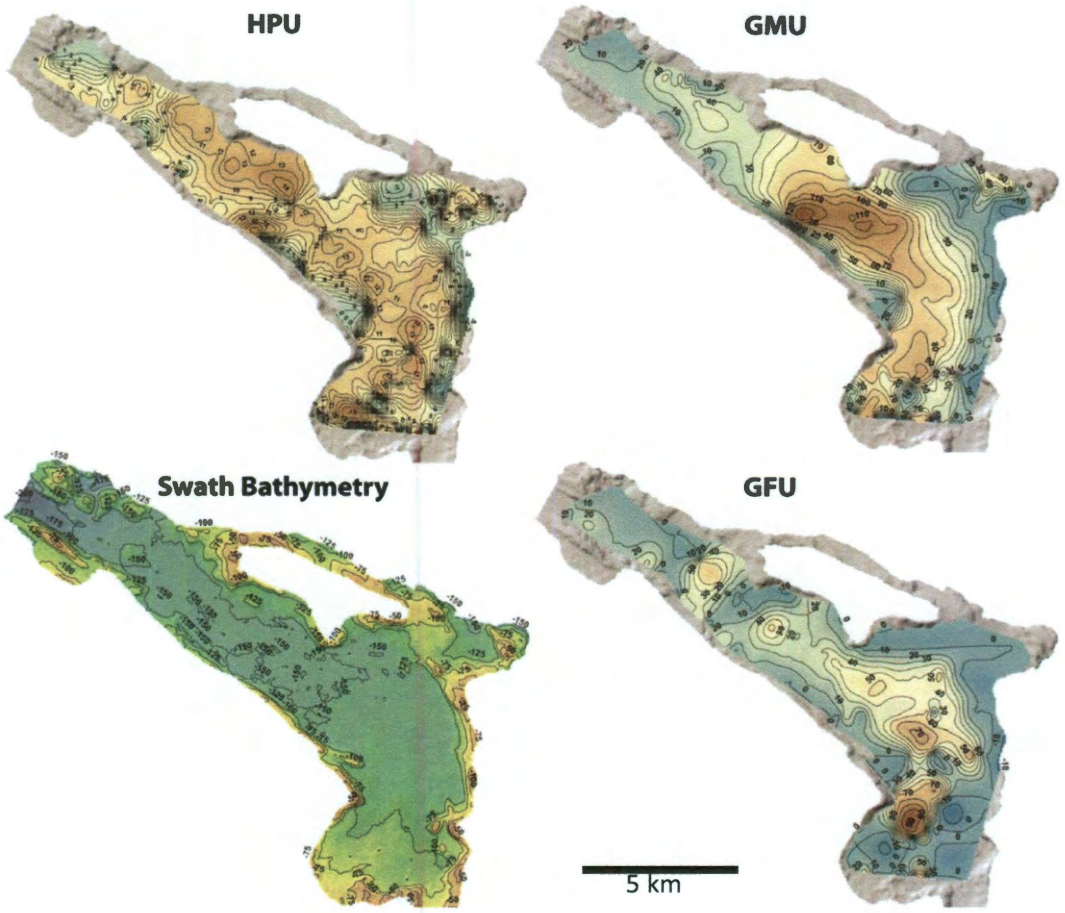

Figure 2.7 Isopach maps of the seismic units described in the text (contour lines: 10 m) and swath bathymetry of the medial basin (contour lines: 25 m).

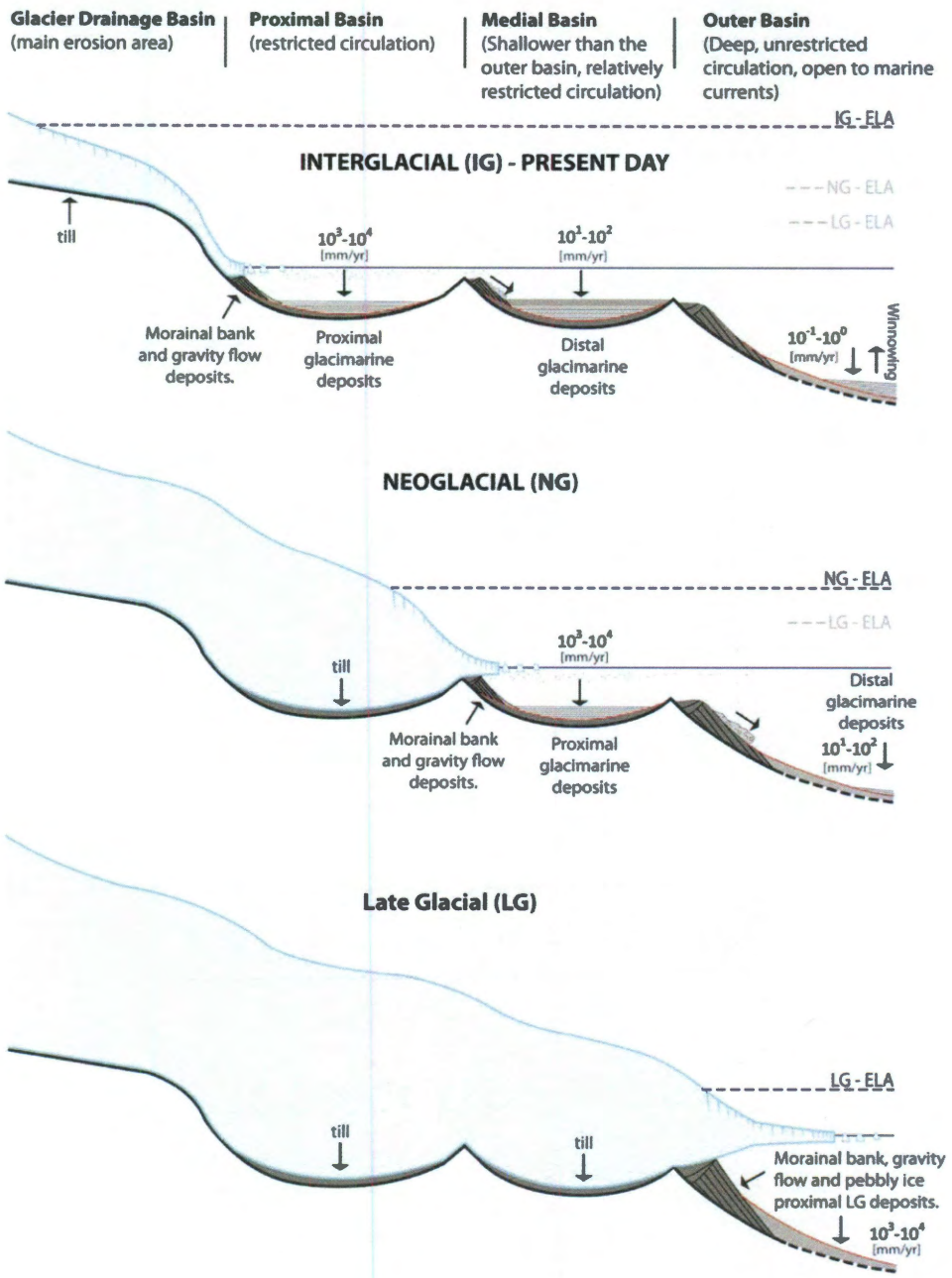

Figure 2.8 Conceptual depositional model for a tidewater glacier that calves in several consecutive basins for LGM, neo-glacial and present day inter-glacial situation. Orders of magnitude of the accumulation rate for each basin is based on the results of Marinelli Glacier studies (this work and Koppes, 2009) and cited literature (Introduction and Table 3). Maximum ELA positions are indicated. ELA: Equilibrium Line Altitude. IG-ELA: Inter Glacial-ELA. NG-ELA: Neoglacial ELA. LG-ELA: Late Glacial ELA. Sea level is kept constant for simplicity.

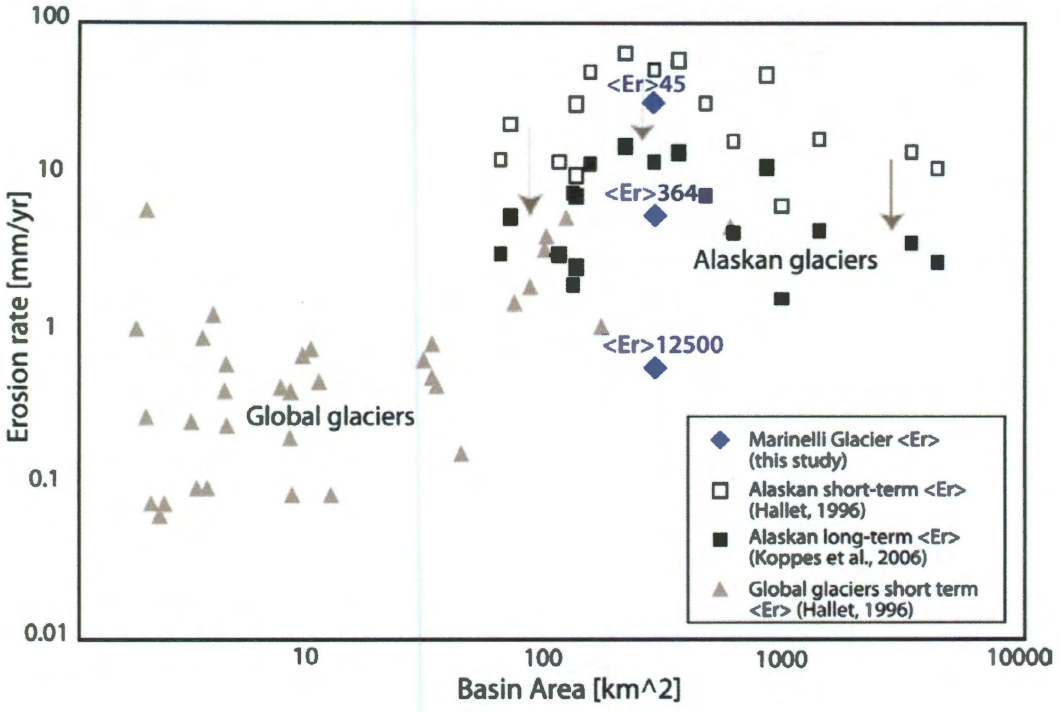

Figure 2.9 Erosion rates versus drainage basin area. Data from Marinelli Glacier are plotted over Hallet (1996) dataset. Numbers indicate the time span that is covered by the respective average erosion rate (<Er>). "Long term" correction of erosion rates for Alaskan glaciers by Koppes et al (2006).

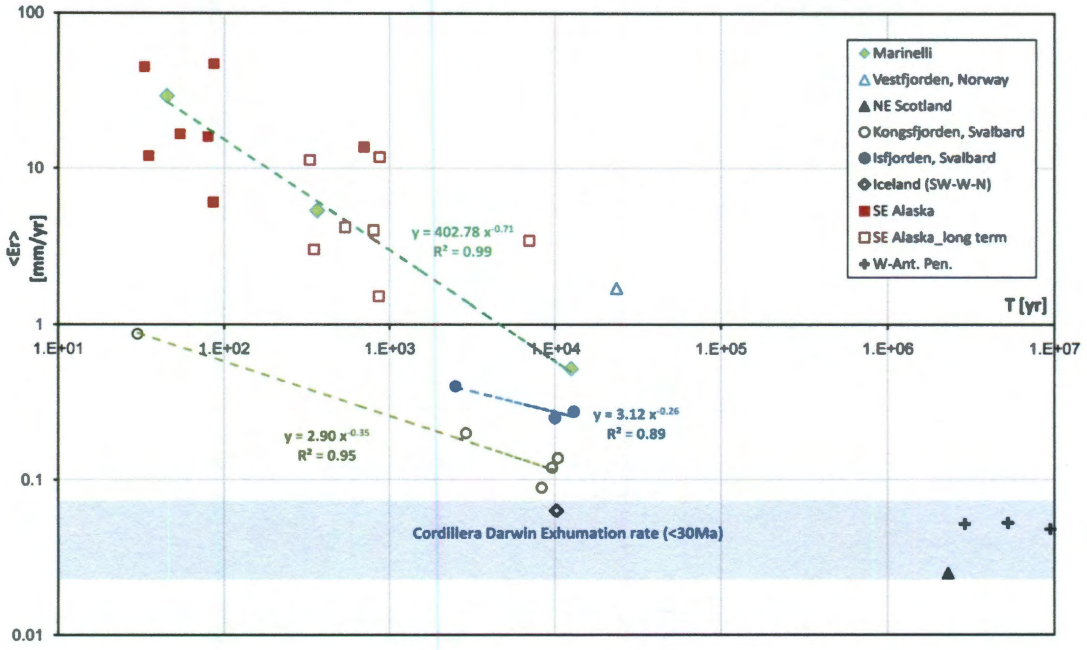

Figure 2.10 Average erosion rates (<Er>) over the last "T" years for glaciated environments. Only studies with data covering >30 yrs and with average erosion rates estimated over an entire drainage basin were considered. The estimated best fit curve for the Alaskan glaciers (not shown in the plot) is <Er>Ak = 94.41*T-0.42. The Cordillera Darwin exhumation rate is based on thermochronoly data from Nelson et al. (1982) and Gombosi et al. (2009).

Chapter 3

Gualas Glacier sedimentary record of climate and environmental change, Golfo Elefantes, Western Patagonia (46.5°S)

Rodrigo A. Fernandez[1], John B. Anderson[1], Sebastien Bertrand[2] and Julia S. Wellner[3]

[1] Rice University, Earth Science Department, 6100 Main St, MS126, Houston,

Texas 77005, USA

[2] Department Renard Centre of Marine Geology, University of Ghent.

Krijgslaan, 281 s.8, 9000 Ghent, Belgium

[3] University of Houston, Department of Earth and Atmospheric Sciences, Houston,

Texas 77204, USA

In press (November 2011):

The Holocene

Abstract

Gualas Glacier is an outlet glacier of the Northern Patagonian Icefield, one of the largest temperate ice bodies on Earth. Golfo Elefantes, the depositional basin of Gualas Glacier, has a sedimentary record that spans, with some hiatuses, at least the last ~11.3±3.0 ka. During this period the gulf remained free of ice, as suggested by the absence of proximal glacimarine sediment and till in the sedimentary section. This implies that the arcuate terminal moraines that occur along the edges of Golfo Elefantes, were formed during the waning stages of the local glacial maxima (Late Pleistocene) or the early Holocene. Between ~11.3±3.0 ka and ~4.2±0.3 - 1.4 ka, the basin received low sediment input consisting of fine-grained sediments in the form of low concentration density currents that filled bathymetric lows. Sediment discharge increased several times in the late Holocene (~<1.4 ka) and started with the accumulation of ~ 0.5 km^3 of sandy sediments in a relatively short time span (~670 yr). This high discharge of sandy sediments is interpreted as being the result of glacial reworking of sediments stored in Gualas Glacier proglacial lake and thus implies that the glacier advanced at ~1.4-0.8 ka. The overall increase in sediment discharge in the late Holocene indicates a sharp increase in centennial timescale precipitation, which in turn suggests an increase in the intensity of the westerly winds in the area. Two recent periods of inter-annual sedimentation variability were identified at ~AD 1160-1460 and ~AD1680-1890 and correlate with documented regional glacier advances.

3.1 Introduction

Gualas Glacier is an outlet glacier of the Northern Patagonian Icefield (NPI), one of the largest temperate ice bodies on earth. NPI has a total glaciated area of 3953 km^2 (Rivera et al., 2007), capping the Andes cordillera at altitudes between 700 and 2500 meters above sea level (masl) and extending 125 km along its NS axis (Glasser et al., 2005). Outlet glaciers on its western side reach almost to sea level, including San Rafael Glacier, the lowest latitude tide water glacier in the world. The mass balance of the NPI has been negative during the last few decades, contributing 0.013±0.006 mm/a to global sea-level rise (Rignot et al., 2003; Rivera et al., 2007). NPI is nourished by moisture transported from the Pacific Ocean by the southern westerly winds, which results in high precipitation throughout the year and a strong west-east precipitation gradient due to the rain shadow effect of the Andes (Warren and Sudgen, 1993). The few weather stations in the region show that the NPI, and thus Gualas Glacier, is located in an intermediate zone with respect to seasonal precipitation: seasonal maxima occur during winter north of the NPI and are reached during summer south of the NPI (Harrison and Winchester, 1998). The climate of the area is highly influenced by the latitudinal position and strength of the Westerly Wind Belt (WWB), which depends on the interplay between the Pacific Anticyclone and the Polar Front. It is hypothesized, based on pollen records, that the WWB shifted northward during the local Last Glacial Maximum (LGM) and then shifted southward during the last deglaciation (Ashworth et al., 1991; Markgraf, 1993; McCulloch et al., 2000; Moreno et al., 2001; Villa-Martínez and Moreno, 2007; Moreno et al., 2010). However, other records suggest that instead of latitudinal wandering the

WWB expanded and weakened during regional cold climate phases (e.g. Late Holocene; Lamy et al., 2010), as occurs today during the austral winter, and that it contracted and strengthened during the early Holocene, as occurs during the austral summer (Lamy et al., 2010).

Most of the NPI glaciers are currently receding from their historical maximum position, which was reached coincidently with the northern hemisphere Little Ice Age (LIA) (17^{th} to 19^{th} centuries AD; Harrison et al., 2007; Araneda et al., 2007; Lopez et al., 2010). Virtually nothing is known about the Holocene behavior of the NPI outlet glaciers prior to the LIA, but it is generally accepted that the entire Patagonian region experienced a pattern of Neoglacial advances similar to that described for the Southern Patagonian Icefield (SPI) by Mercer (1965, 1968, 1976) and others (see next sections).

In this study we focus on the Holocene sedimentary record of Golfo Elefantes in central western Patagonia (46.5°S). Most of the sediment supplied to this gulf is generated by Gualas Glacier and delivered to the gulf by Gualas River. Minor amounts of sediment is supplied to Golfo Elefantes by Reicher Glacier through Gualas River, and by San Rafael Glacier through Rio Tempanos (Fig 1). Hence we interpret the sedimentary record of Golfo Elefantes as an archive of past variability of the coupled Gualas Glacier/River system. We present data that indicates an order of magnitude increase of sediment discharge to the basin in the late Holocene (~<1.4-4.3 ka) compared to early Holocene-late Pleistocene (~4.3-11.3 ka). This increased sediment flux is interpreted to represent increased precipitation related to intensification of the westerly winds in the area. The deposition of sandy sediments at the beginning of the late Holocene (~0.8-1.1 ka) is interpreted as the result of advance of Gualas Glacier over its proglacial lake and

reworking of the sediments stored there. Our results shed light on the history of other glaciers of western Patagonia and contribute to the understanding of the Holocene behavior of the southern WWB.

3.2 Glacial evolution of Patagonia

3.2.1 LGM and deglaciation

Maximum ice extent during the LGM was reached diachronously along the Patagonian Andes, with recent age estimations falling within the interval 22-26 ka (Kaplan et al., 2004, 2008; McCulloch et al., 2005; and references therein). At the latitude of Gualas Glacier (46.5° S), the ice persisted close to LGM limits until ~15-16 ka, when the extensive piedmont ice lobes that characterized the LGM ice sheet in the eastern flanks of the Patagonian Andes shrank to give way to present day outlet glaciers that drain into fjord lakes and glacial valleys east of the North Patagonian Icefield (Turner et al., 2005).

Following the initial glacial retreat along the eastern side of the Patagonian Andes, glaciers stabilized until ~13.6-12.8 ka (Turner et al., 2005). At this time a second stage of retreat resulted in the separation of the Pleistocene Patagonian Ice Cap into the Northern and Southern Patagonian Icefields (Turner et al., 2005). Whether this two stage retreat was mimicked on the western side of the Andes remains unknown.

Relatively few studies have been conducted on the western side of the Patagonian Andes and much uncertainty exists concerning the timing and geographic pattern of the Pleistocene deglaciation. In the Taitao Peninsula, west of Gualas Glacier, several studies obtained minimum ages of deglaciation around 16-18 ka (~14,000 ^{14}C yr BP; Heusser, 2002; Lumley and Switsur, 1993; Bennett et al., 2000). This indicates that the deglaciation of Taitao Peninsula occurred at least a couple of millennia earlier than on the eastern side of the Andes, at a time when some reconstructions and models suggest that the area was still covered by ice (Hubbard et al., 2005; Turner et al., 2005).

3.2.2 Neoglaciation

The majority of studies suggest that no regional glacial advance occurred during the early-middle Holocene and that between three to six late Holocene glacial advances took place at different latitudes within the Patagonian Andes since ~5000 ^{14}C yr BP. Widely accepted is Mercer's (1965, 1968, 1970, 1976) chronology of three major Holocene advances culminating at 4600-4200 ^{14}C yr BP, 2700-2000 ^{14}C yr BP, and 17th to 19th centuries AD, the last one being equivalent to the northern hemisphere Little Ice Age (LIA). However, recent works suggest additional Neoglacial advances at around 3600 ^{14}C yr BP (Aniya, 1995; Wenzens, 1999, Strelin et al., 2008), at ~ 1600-1288 ^{14}C yr BP (Röthlisberger, 1986; Aniya, 1995; Strelin et al., 2008) and at ~900-500 ^{14}C yr BP (Röthlisberger, 1986; Aniya, 1995; Koch and Kilian, 2005; Strelin et al., 2008) in Darwin Cordillera and at some eastern outlet glaciers of SPI. Additionally, there is some evidence indicating early-Holocene (~ 6-9 ka) advances in at least three areas along the eastern

flanks of the Patagonian Andes, but their regional significance and climate ties are still a matter of debate (Röthlisberger, 1986; Wenzens, 1999; Douglass et al., 2005).

The chronology of centennial to millennial scale Holocene glacier fluctuations remains obscure in the area of Gualas Glacier. The most studied glaciers in this area are San Quintin and San Rafael glaciers, the two largest outlet glaciers of the NPI. Along with Gualas Glacier, all three glaciers have prominent terminal moraines located along a fault-controlled elongated basin west of the cordilleran front (Figure 3.3.1). The similar relative location of terminal and frontal moraines (Heusser, 2002) further suggests that they were constructed in response to the same climatic forcing and not by internal ice dynamics. Unfortunately, due to the lack of suitable material for age determination and the complexity of the facies architecture of these moraines, the only ages that have been obtained to date are from the dual moraine system of San Rafael Glacier known as Témpanos I and II (Muller, 1959) (Figure 3.3.1). Heusser (1960, 2002) obtained a date of 3740 ^{14}C yr BP for near basal sediments in a small lagoon between Témpanos I and II moraines and another of 3600 ^{14}C yr BP that postdates Témpanos I-II outwash deposits along Rio de Los Témpanos (Figure 3.3.1). A third age of 6850 ^{14}C yr BP from a peat bed located inside the perimeter defined by a younger moraine system (Témpanos III; Figure 3.3.1; Muller 1959) was interpreted by Heusser (1960, 2002) as implying that Témpanos I-II were formed after an early Holocene recession. This is supported by the occurrence of deformed laminites at the bottom of the morainal sequence (Glasser et al., 2006). The age of the analogous morainal arcs associated with Gualas Glacier at Golfo Elefantes, which we informally call Gualas I, II and III (Figures 1b and 2), is unknown.

By comparison, the recent behavior of Gualas Glacier has received much attention (Harrison et al., 2007; Winchester and Harrison, 1996; Harrison and Winchester, 1998). Harrison and Winchester (1998) estimated that Gualas Glacier retreated from its LIA position (moraine system Gualas IV; Figure 3.3.1) by ~1870 AD based on a dendrochronological study of trees on the highest trimline near the present day ice front. According to the same author, marked retreat also occurred during the 1920s-1930s and 1960s-1970s. A similar pattern of retreat is documented for the nearby Reicher, San Rafael and San Quintin glaciers, and appears to correlate with periods of reduced precipitation in the area. This suggests that climate might effectively control the behavior of these glaciers, at least at decadal timescales (Warren, 1993; Winchester and Harrison, 1996; Harrison and Winchester, 1998; Araneda et al., 2007).

The middle to late Holocene in Patagonia might therefore have been characterized by up to six Neoglacial advances: I, ~4600-4200 ^{14}C yr BP; II: ~3600 ^{14}C yr BP; III: ~2700-2000 ^{14}C yr BP; IV: ~1600-1288 ^{14}C yr BP; V: ~900-500 ^{14}C yr BP; and VI (LIA): 17th-19th centuries AD.

3.3 Methods

A marine geological survey was conducted onboard the research vessel RV/IB *Nathaniel B. Palmer* during the austral winter of 2005 (Appendix B1). During this cruise we obtained a dense grid of 3.5 kHz sub-bottom profiler (SBP) data and single-channel air gun seismic data in "Golfo Elefantes" (Figure 3.3.2). Swath bathymetry mapping was

conducted using a hull-mounted Simrad EM120 multibeam sonar system consisting of 120 beams using a 12 kHz source. Sediment discharge from Gualas River was derived from the volume of the seismic units imaged in the 3.5 kHz and air-gun seismic profiles (Figures 3.2, 3.3, 3.4a, 3.4b and Appendix B2) using the sea floor bathymetry as a bounding surface following Fernandez et al. (2011).

Sedimentation rates and the ages of seismic units were estimated using two radiocarbon-dated sediment cores. The cores were opened, described and sampled onboard. Further analyses were made to characterize the sediments and to correlate the sedimentological facies with seismic units. Analyses included particle size distributions, physical properties, total organic carbon measurements and x-radiography (Appendix B1). Radiocarbon ages were obtained on 13 samples of carbonate shell material and terrestrial plant material (JPC12: 3 samples, JPC14: 10 samples; Table I).

3.4 Results

3.4.1 Seismic facies and architecture

We identified 6 seismic units in the Golfo Elefantes based on internal seismic characteristics (amplitude, spacing and continuity of reflections) and geometric relationships between units. The stratigraphic relationship between these units and their internal architecture was better imaged in north-south lines 3 and 10 (Figures 3.2, 3.3 and

4a), and in east-west line 5 (Figure 3.4b). Hence, the following description will be based mainly on these three lines (details in Appendix B3).

Seismic unit G1 was imaged only in the western part of Line 5, near the two arcuate moraines that surround Golfo Elefantes (Figures 2 and 4b), and is the oldest distal glacimarine deposit in the gulf. Unit G1 is overlaid by Unit G2, which is characterized by relatively strong reflections roughly parallel to the (acoustic) basement (Figures 3.2, 3.3, 3.4). Unit G2 rests directly on bedrock or morainal deposits (acoustic basement), is laterally continuous and shows uniform thickness over large areas. Neither G1 nor G2 were sampled.

The oldest seismic unit that was sampled by cores is G3. It is composed of parallel, near horizontal reflections that onlap the irregular and relatively well defined contact with underlying unit G2 and fills depressions in the sea floor (Figures 3.3, 3.4). Unit G3 is overlaid by G4, which is characterized by discontinuous and relatively strong reflections. Unit G4 has variable thickness (<10m), with a low-relief upper boundary (Figure 3.4). As seen near the center of Lines 3, 5, and 10, unit G4 onlaps underlying unit G3 (Figure 3.4), although the contact is difficult to follow due to its irregular and discontinuous character. The same seismic profiles show that only the top of unit G4 occurs at coring site JPC14 (Figure 3.4). This indicates the existence of a hiatus at the contact with the underlying unit (G3) at that location. Overlying G4 there are two units of similar seismic architecture, units G5 and G6. Unit G5 is characterized by medium-low amplitude reflections alternating with transparent intervals indicating thin bedding of approximately 40 cm thickness (the approximate vertical resolution of our seismic acquisition system). This unit downlaps at low angles onto underlying unit G4 and thins

to the north in lines 3 and 10. Unit G6, the youngest seismic unit, is bounded by two strong, continuous and roughly parallel reflections separated by up to ~2.5 m (from peak to peak) in the central part of the basin. Unit G6 looses continuity and pinches out toward the north (lines 3 and 10; Figure 3.4a) and, to a lesser extent, to the west (line 5; Figure 3.4b).

3.4.2 Sedimentology of seismic units

The description of the sedimentary facies associated with seismic units G3 through G6 is based mainly on core JPC14, located approximately at the intersection of seismic lines 3, 10 and 5 (Figure 3.3.2). Six lithofacies units were defined based mainly on changes in grain size distribution and occurrence of laminations (Figure 3.5). Five of these units consist primarily of silty mud (SM1, 2, 3, 5, and 6; Figure 3.5) and one is composed of silty sand (SS4; Figure 3.5).

Seismic unit G6 corresponds to the top 196-240 cm of core JPC14 (top of unit SM1; Figure 3.5). The lower boundary of G6 correlates with a silty mud interval (196-240 cm) with sandy layers (<2cm thick) and associated organic matter (leaves and pieces of wood) that marks the deepest visible layering in SM1 (Figure 3.5). This same interval shows the highest TOC values of the core (~1-1.7%). Seismic unit G5 composes the lower part of lithofacies unit SM1 and complete units SM2 and SM3. The overall lithology is silty mud with increasing percentages of clay (from <20% to ~30%) and sand (from <10% to <20%) towards the bottom (Figure 3.5). The appearance of laminations

<1 cm thick between 689 – 797 cm (bottom of SM2 and all SM3) and an increase in sand correlate with relatively high TOC values (~0.9-1.4%).

Seismic unit G4 correlates with a 328 cm thick interval of silty, fine sand that composes sedimentary unit SS4 (796.5-1125 cm). There are three main peaks in sand content (sub units SS4a,b,c; Figure 3.5) that seem to correlate with the two internal reflections in unit G4 at the location of core JPC14 and the strong reflection that marks the top boundary of this unit. Visual inspection of the bottom contact of the silty sands of SS4 in core JPC14, as well as the grain size data (Figure 3.5), shows a gradational contact associated with the hiatus inferred from the seismic records. The absence of visible organic matter in this unit is consistent with relatively low TOC content in this unit (~0.4-0.6%).

The oldest seismic unit sampled by JPC14, G3, comprises two sedimentary units: SM5 and SM6 (Figure 3.5). Both consist of silty mud with variable percentages of sand (SM5: 20% sand; SM6: 5-10% sand) that decreases down core (Figure 3.5). Some silty/sandy laminations were visually identified in unit SM5, but several intervals with layering and laminations were observed in the x-rays of unit SM6.

3.4.3 Age constraints for seismic units

Accumulation rates and bounding ages for seismic units G3 through G6 were determined from 13 radiocarbon ages obtained from shells and vegetation samples in cores JPC14 and JPC12 (Table I).Three dates from the top of unit SM1 in core JPC14

(~200-220 cm; Figure 3.5 and Table I) imply that unit G6 accumulated at a rate of ~10 mm/yr (Figure 3.6) since the beginning of the 18th century. Four radiocarbon ages with calibrated ages ranging from 328 to 729 cal yr BP (2σ minimum and maximum interval) were obtained from core JPC14 for seismic unit G5 (Table I; Figure 3.6). These ages, plus the three from unit G6, show a clear linear trend in the age model (R^2=0.75; Figure 3.6), implying an average accumulation rate of ~10 mm/yr for these two units (Figure 3.6). Using this rate to estimate the age of the top and bottom of unit G5 at the location of core JPC14, we determined that unit G5 accumulated between ~AD 1160 and 1710 (~240-790 cal yr BP). Three other ages obtained in core JPC12 (calibrated ages that fall between 454-909 cal yr BP, 2σ minimum and maximum interval, further support this chronology (Table I; Figure 8). These ages imply a linear accumulation rate of 12.7 mm/yr (R^2=0.76; Figure 3.6), which indicates that at the location of JPC12 unit G5 was deposited between ~AD 1170 and 1580 (~780 - 370 cal yr BP) (Figure 3.6).

No radiocarbon ages were obtained in Unit G4 due to the lack of datable material. The down-core extrapolation of the accumulation rate of G5 in JPC14 (10.1 mm/yr) implies that the portion of G4 sampled at this site was deposited in 325 years (Figure 3.6). However, just ~1 km from JPC14, G4 is about 6 m thick and consist of six instead of three seismic layers seen at the location of JPC14 (Figures 4). This implies that at that location G4 represents ~600 years of sediment accumulation. A similar down core extrapolation of G5 accumulation rates at the location of JPC12, where G4 is ~8.5 m thick (Appendix B2), implies that G4 accumulated during a time span of ~670 years. The extreme values for the time span of accumulation of G4 (325 and 670 yr) are used to estimate a maximum and minimum sediment discharge for this unit. However, the

estimated time span from core JPC14 must be taken with caution since the section at this location includes a hiatus (see previous sections; Figure 3.6).

Table 3.1. Radiocarbon and calibrated ages for cores JPC12 and JPC14

	Core depth (cm)	Laboratory code	Material	$\delta^{13}C$ (‰)	^{14}C yr BP ± 1σ	Reservoir correction (yrs)	2 σ range calibrated ages (cal yr BP)	Weighted average
JPC12	410	OS- 50966	Shell fragments	0.6	960 ± 30	480	454-534 (95%)	496
	517	OS- 51078	Wood	-27.43	775 ± 25	--	577-725 (95%)	675
	760	OS- 51706	Wood	-28.34	835 ± 85	--	565-909 (95%)	732
JPC14	200	OS-51044	Shell fragments	0.24	730 ± 40	480	140-328 (89%)	224
	210.75	OS-79111	Leaf	-28.37	120 ± 25	--	0-254 (95%)	102
	217	OS-51079	Leaf fragments	-29.52	230 ± 25	--	146-304 (95%)	208
	464	OS-70902	Shell fragments	2.44	910 ± 30	480	328-508 (95%)	440
	559	OS-51080	Leaf fragments	-27.43	600 ± 35	--	513-635 (95%)	568
	690.5	OS-51040	Shell	-0.02	1240 ± 45	480	563-729 (95%)	653
	720.75	OS-79113	Twigs	-28.01	880 ± 25	--	685-791 (95%)	743
	1234	OS-71182	Shell fragments	0.10	4590 ± 25	480	4423-4789 (95%)	4543
	1412.5	OS-71183	Shell fragments	-1.56	5000 ± 20	480	4972-5287 (96%)	5137
	1414	OS-70903	Shell fragments	-1.41	4980 ± 35	480	4877-5285 (95%)	5089

Notes: Samples were analyzed at the National Ocean Sciences Accelerator Mass Spectrometry Facility (NOSAMS). Calibration was made using OXCAL 4.1 and calibration curve SHCal04 (southern hemisphere atmospheric curve; McCormac et al., 2004). Probability percentages associated with 2 σ ranges are approximated.

Three calibrated ages ranging from 4423- 5287 cal yr BP (2σ minimum and maximum interval) were obtained in core JPC14 for Unit G3 (Table I). Using these ages we calculated an accumulation rate of ~3.1 mm/yr for the interval 1234-1414 cm (Figure 3.6). Using this rate results in an age for the upper limit of Unit G3 of ~4230 cal yr BP,

with an uncertainty (~95% confidence interval) between ~4450 cal yr BP and ~3925 cal yr BP (Figure 3.6; for simplicity this age will be presented as ~4.2±0.3 ka in the discussion section). To estimate the age of the base of unit G3, we extrapolated the accumulation rate of G3 down section at its thickest part near core JPC14 (~22 m, about 3 km north of JPC14; Figure 3.5a) and obtained an age of ~11,300 cal yr BP. Given the few radiocarbon ages for G3, the uncertainty of the limiting ages for this unit is higher than for units G5 and G6. Figure 3.6 shows the uncertainty of the age model for unit G3 estimated from accumulation rates obtained from all possible combinations of calibrated ages within the 95% interval of confidence. This model implies that the actual age of initial accumulation of G3 might fall within the interval ~8500-14500 cal yr BP (Figure 3.6; for simplicity this age will be presented as ~11.5±3.0 ka in the discussion section). However this is considered a conservative estimate of the uncertainty since the monotonous parallel horizontal reflections that characterized G3 (Figures 3.3 and 3.4a) suggests little variation of the accumulation rate.

3.4.4 Sediment discharge

To estimate the sediment discharge corresponding to each seismic unit, we used estimates of the rock-equivalent volume of each unit (i. e., the total volume of sediments multiplied by the ratio between the density of the sediments over the source rock's density) divided by the time span over which these units accumulated. The total volume

of sediments accumulated in Golfo Elefantes was obtained by mapping the onlap of glacimarine sediments onto steeply dipping reflections of unit G2 (Figures 3.3, 3.4), and then calculating the volume of sediment between this surface and the sea floor. Similarly, we mapped a reflection that lies about 9 meters below sea floor (mbsf) and corresponds to the boundary between units G4 and G5 using the 3.5 kHz subbottom profiler records (SBP). The volumes of units G5 and G6 were estimated from their relative proportions in the SBP sections along lines 3 and 10. Then, by mapping unit G4 in the same sections, we estimated its volume as a proportion of the combined volumes of G5 and G6. Finally, the volume of G3 was calculated as the difference between the total sediment volume and the volumes of the other units (i. e., G4+G5+G6). Errors were estimated for the total interval of uncertainty from each parameter involved in the calculations. Table II and Figure 3.7 summarize our results.

For units G4, G5 and G6 the uncertainty presented in Table II is produced mainly from the calculation of volumes. The sediment discharge represented by unit G4 is considered a maximum since the time span of accumulation could be longer than the estimated value if the hiatus separating G4 from G3 (Figure 3.6) is in fact shorter in some other non-studied locations. Figure 3.7 shows that, using accumulation rates and unit thickness found in JPC14, the equivalent discharge of G4 doubles. For unit G3, the associated uncertainty comes mainly from the age determination of the onset of its accumulation, and to a lesser extent, from the age of its top (Figure 3.6 and 3.7). Even considering extreme scenarios for the time span of accumulation of G3, including the oldest possible estimate of the onset of its accumulation (~14.5 ka) and no hiatus between G3 and G4 (i. e., the age of G3's top being equal to the estimated age of G4's bottom,

~1.1 ka), the time averaged sediment discharge (Qs) represented by unit G3 is several times less than any of the younger units (Figure 3.7).

Table 3.2 Summary of sediment discharge associated with seismic units G3 through G6

Unit	Volume (m^3)	Density ratio	JPC14 clay (%)	JPC14 silt (%)	JPC14 sand (%)	Time span (yr)	Sed. discharge (kg/s)	Uncertainty (kg/s)
G6	$1.24\ 10^{08}$	0.81	14.8	77.6	7.7	238	36.22	9
G5	$3.75\ 10^{08}$	0.80	22.4	67.0	10.7	551	46.37	12
G4	$3.53\ 10^{08}$	0.89	9.5	36.4	54.0	670	40.07	10
G3	$7.41\ 10^{08}$	0.80	22.6	65.3	12.1	7097	7.12	4

Density ratio uses a rock density of 2700 kg/m^3 and sediment densities between 2150 and 2400 kg/m^3; Qs: sediment discharge. For G4, the time span is the value associated with the longer timespan according to the extrapolation of sedimentation rates from overlying units in cores JPC12 and JPC14.

3.5 Discussion

3.5.1 Implications for the Late Pleistocene glacial history of the fjords west of the NPI

According to our best estimates, the marine sedimentary record of Golfo Elefantes spans, with some hiatuses, the last ~11.3±3.0 ka. Between ~11.3±3.0 ka and ~4.2±0.3 ka (Early-Middle Holocene) mostly fine-grained sediments accumulated in the basin. These sediments were derived from turbidity currents (underflows), forming subhorizontal layers that filled bathymetric lows within the basin (seismic unit G3; Figures 3.4). The lack of strong seismic reflections or evidence of channelized deposits or prograding wedges indicates relatively steady sediment accumulation, likely associated with climate and glacier stability. Additionally, no evidence was found of till or ice proximal deposits. Rather, sediments from this time interval that were sampled in core JPC14 are characterized by an absence of material coarser than fine sand and by high clay content. The grain size distribution and high clay content imply that syn- or post- depositional winnowing did not occur during the deposition of this unit (seismic unit G3; Figure 3.5 and Appendix B4). Thus, the low sediment discharge (Qs) calculated for G3 (~7.1 kg/s; Figure 3.7) can be considered a good approximation of the early Holocene sediment discharge of Gualas River.

The absence of ice contact sediments raises the question of the age of the arcuate (terminal) moraines that occur along the edge of Golfo Elefantes (MS Gualas I; Figure 3.3.2). Our data suggest that the moraines were formed before the deposition of unit G3

(>~11.3±3.0 ka), probably in the late/waning stages of the local LGM. This is supported by basinward dipping reflections in E-W seismic lines (unit G2, Figure 3.4b) near the moraines, over which subhorizontal reflections of unit G3 onlap. Similar geometries and seismic character are found in other Patagonian fjords and have been interpreted as the contact between glacimarine/marine sediments and ice-proximal or post-retreat gravity flow deposits (e.g. DaSilva et al., 1997; Boyd et al., 2008; Fernandez et al., 2011). Thus, the age of the formation of these terminal moraines is bracketed by the age of the beginning of marine sedimentation in Golfo Elefantes (~11.3±3.0 ka) and the age of the retreat of the eastern NPI glaciers into mountain valleys, assuming that glaciers in the western (wet) side of the NPI retreated into the present day fjords at least as early as their eastern (dry side) counterparts (~12.8 ka; Turner et al., 2005). If the terminal moraine systems of San Rafael and San Quintin glaciers were formed synchronously with those of Gualas Glacier, as suggested by their similar geometries and relative positions (Heusser, 1960, 2002), the age of Tempanos I and II moraines (Figure 3.2) has been largely underestimated, and/or the few published radiocarbon ages have been misinterpreted. In either case, the possibility that the terminal moraines of these glaciers were originally formed in the late Pleistocene – early Holocene and subsequently reoccupied during late Holocene advances (e.g. some indication exists that San Quintin Glacier might have extended to its terminal moraine by the end of the nineteenth century; Winchester and Harrison, 1996) cannot be ruled out.

3.5.2 Implications for sediment discharge variations in the Holocene

Our data show that the millennial average sediment discharge of Gualas River during the interval ~11.3±3.0 to 4.2±0.3 ka was close to estimated modern values (Figure 3.7). Sediment discharge increased several times during the late Holocene (~<1.4-4.2; Figure 3.7). The simplest explanation for increased sediment discharge during the Late Holocene is the reworking of sediments from isolated sediment sinks (pro-glacial and subglacial) and/or increased glacier erosion by Gualas Glacier and, to minor degree, Reicher Glacier.

The silty sands of seismic unit G4 record an important Holocene event in Golfo Elefantes. In the southern part of the basin, this unit conformably overlies early Holocene sediments of unit G3. However, at the location of JPC14, seismic reflections of G4 onlap unit G3, implying a depositional hiatus (~<3100 years; Figures 3.4a, 3.4b and 3.6). Variations in the sand content of G4 probably reflect variations in the relative proportion of sands supplied from the source. Our estimates show that the sediment discharge for G4 (~40 kg/s) is several times higher than for underlying unit G3 (~7 kg/s; Figure 3.7). Assuming that G4 was derived from a similar low sediment discharge (Qs) and low sand concentration as for unit G3, the volume of sand in Unit G4 (~$1.7*10^8$ kg) would require an unrealistic time span for deposition (~16.8 ka). Likewise, if we assume that the hiatus that separates G3 and G4 is negligible (i. e., G4 accumulated at ~ 1 mm/yr at the location of JPC14; Figure 3.6), and that there was no variation in the relative percentage of sand delivered to the gulf, sediment discharge would have to have increased several times (>38 kg/s) along with a significant increase in winnowing to produce the sandy sediments of G4. Although an increase in sediment discharge of this magnitude is possible, the grain

size data do not indicate depletion, and therefore winnowing, of the fine fraction. Rather, the size distribution consists of two distinctive modes, one consisting of fine to very fine sand and the other consisting of a very fine silt and clay (Appendix B4).

At the location of JPC14, Unit G4 was deposited at an estimated water depth of around 120-130 m, based on the accumulation rate and a conservative estimate of compaction of 10-30 %. The core site is only 3 km from the steep slope of the innermost morainal arch of Gualas Glacier (~ 50 m water depth) (MS Gualas III; Figure 3.3.2). Hence, either turbidity currents flowing off the arc or hyperpycnal flows emanating from the Gualas River could have delivered sandy sediments to this location. But unit G4 lacks the sedimentary structures and grain size grading indicative of turbidite deposition. Instead, unit G4 comprises three poorly sorted coarsening upward subunits (Figure 3.5: SS4 a,b,c). Thus, sediment delivery by hyperpycnal flows is the most likely mechanism for the deposition of Unit G4.

According to Mulder and Syvitski (1995) and Mulder et al. (2003) hyperpycnal flows normally occur at sediment concentration higher than 36-43 kg/m^3, but can occur at concentrations as low as 5 kg/m^3 if convective instability is considered. Using the BQART global model (Syvitski and Milliman, 2007) and an annual rainfall in the area of ~2000-3000 mm/y (Aniya and Enomoto, 1986), we estimate that modern annual average sediment discharge (Qs) of Gualas River falls in the range Qs=4.4-6.8 kg/s (Figure 3.7), with an average particle concentration (Cs) in the range 0.2-0.4 kg/m^3. Higher values of Qs and Cs (~11 kg/s and ~1 kg/m^3 respectively) are obtained if a 30% higher ice cover is introduced into the model (today ice cover is ~55%), so that the pro-glacial lakes that trap some of the sediments from Gualas and Reicher glaciers are covered by ice. Although the

Cs values obtained from the QBART model for Gualas River are relatively low compared to other rivers that produce frequent hyperpycnal flows (10-40 Kg/m^3; Mulder and Syvitski, 1995; Mulder et al., 2003), hyperpycnal flows commonly form during periods of high discharge or flooding events when Qs and particle concentration increase.

A weather station at Puerto Aysen, ~140 km to the north of Golfo Elefantes, recorded maximum daily precipitation values of ~180 mm/day (Stappung, 2000). Based on these data, we estimate that maximum discharge of Gualas River during flooding events could reach up to 200-300 m^3/s. As particle concentrations increase with water discharge, these estimates suggest that the threshold concentration for producing hyperpycnal flows could be reached during high precipitation events or during the peak of the melting season.

3.5.3 Implications for the Holocene climate of the west NPI area

Several authors have related modern fluctuations in glaciers on the west side of the Northern Patagonian Icefield (NPI) with precipitation trends (Warren, 1993; Winchester and Harrison, 1996; Harrison and Winchester, 1998). Based on these studies, last century glacial advances and still stands are related to high annual (primarily winter) precipitation whereas retreat periods are related to periods of low precipitation. If this relationship is valid for the Holocene, it implies that unit G3, which is associated with low sediment discharge, was deposited during a relatively dry early-middle Holocene (~>1.4-4.2 ka) when Gualas Glacier was confined to relatively high altitudes. In this

scenario, the coarser fractions delivered by glacial discharge would be trapped in Gualas's (paleo) proglacial lakes. In contrast, our data suggests that units G4, G5 and G6 would have been deposited under relatively wet conditions that resulted in increased water discharge of Gualas River during the late Holocene (<1.4-4.2 ka). The advance of Gualas Glacier during the initial period of increased precipitation would cause reworking of sediments from Gualas's proglacial lakes producing an increase in the sand content of Gualas River sediments and the deposition of unit G4 between ~1.4ka and 0.8 ka. Subsequently, an increase in glacier erosion and/or the release of sediments stored in the pro-glacial and subglacial environments produced an increase in the sediment discharge of Gualas River and the deposition of units G5 and G6.

The increase in long-term (millennial scale) precipitation is interpreted as the result of the intensification of the westerly winds in the area during the late Holocene (<1.4-4.2 ka). This interpretation is consistent with humid conditions during the late Holocene (<4-5 ka) in contrast to the relatively drier conditions that existed during the middle and early Holocene, documented further to the north west of the Andes at ~41°S and ~34°S (Lamy et al., 2001; Jenny et al., 2002; Villa-Martinez et al., 2003). South of our study area, along the west side of the Patagonian Andes (~53°S), the opposite pattern has been documented; humid conditions during the early Holocene were followed by relatively drier conditions in the middle to late Holocene (Lamy et al., 2010). This emerging pattern of opposing trends in precipitation north (~41°S) and south (~53°S) of the study area, and the severe arid conditions at ~34°S during the early-middle Holocene (Villa-Martinez et al., 2003), suggest that the westerlies wind belt widened and/or its core shifted northward during the late Holocene.

In core JPC14, relatively high TOC content (~0.8-1.6%) and concentrations of plant and dark organic debris characterize the intervals 2-3 mbsf (top of unit G5 and bottom of unit G6) and 7-8 mbsf (bottom of unit G5) (Figure 3.5). These intervals record episodes of organic-rich sedimentation that were likely generated by reworking of deltaic sediments. Based on our age model (Figure 3.6), the average recurrence time of deposition of laminations is ~5-7 years for the top ~2 m of Unit G6 and within the interval 5-7 mbsf of unit G5 in core JPC14 (Figure 3.5). An average recurrence time greater than 20 years is estimated for the rest of units G5 and G6. Thus, for units G5 and G6, a period of relatively frequent (inter-annual) deposition of laminations, which might indicate inter-annual discharge variability, followed an initial period of organic-rich deltaic sedimentation. For unit G5, the overall interval of inter-annual sedimentation (discharge) variability occurred during the interval ~790-490 cal yr BP (AD 1160-1460). This interval correlates with a cold and moist period indicated by tree ring studies in northern Patagonia around AD 1270-1660 (Villalba, 1994), and with several glacier advances in the region that are believed to represent Neoglacial V (~900-500 ^{14}C yr BP or ~1200-1460 AD; Röthlisberger, 1986; Aniya, 1995; Koch and Kilian, 2005; Strelin et al., 2008).

Similar sedimentation patterns in the top 2-3 m of JPC14 (Figure 3.5) indicate that the period AD 1680-1750 was characterized by strong deltaic influence. This was followed by deposition of inter-annual laminations (inter-annual discharge variability), that lasted until AD 1890. This overall period (AD1680-1890 or ~270-60 cal yr BP) coincides with the advance of a number of Patagonian glaciers (e.g. Araneda et al., 2007),

and with the last Neoglacial (VI: 17^{th}-19^{th} AD) proposed by Mercer (1965, 1968, 1976) and widely correlated with the northern hemisphere Little Ice Age.

The discharge variability deduced from core JPC14 for the last ~790 yrs suggest that a phenomena with a multiannual period, such as the El Nino Southern Oscillation (ENSO), affected the precipitation pattern of the area. As discharge variability occurred when some glaciers in Patagonia advanced or were at still stand positions, we hypothesize that increased ENSO frequency might have a positive impact on the mass balance of Patagonian glaciers. Further studies are necessary to test this hypothesis.

3.6 Conclusions

The sedimentary record of Golfo Elefantes, the marine depositional basin of Gualas Glacier, spans, with some hiatuses, at least the last ~11.3±3.0 ka. During this period the gulf remained free of ice, as indicated by the absence of proximal glacimarine sediment and till in the Holocene sedimentary sequence. This implies that the age of arcuate moraines that occur along the edges of Golfo Elefantes is bracketed between the age of the waning stage of the local LGM ~<12.6 ka (Turner et al., 2005) and the beginning of glacimarine sedimentation in Golfo Elefantes at ~11.3±3 ka. Between ~11.3±3 ka and ~4.2±0.3 – 1.4 ka, fine-grained sediments deposited from low concentration density currents filled bathymetric lows. Millennial average sediment discharge of Gualas River at this time was low (7.1±4.0 kg/s), but similar to modern expected values (4.4-6.8 kg/s). Sediment discharge averaged over centennial time scales

increased several times during the late Holocene (~<1.4-4.2 ka). The simplest explanation for increased sediment discharge (36-40 kg/s) is reworking of sediments from isolated sediment sinks (pro-glacial and subglacial) and/or increased glacier erosion by Gualas Glacier and, to a lesser degree, Reicher Glacier. The high sediment discharge began with the accumulation of ~ 0.5 km^3 of sandy sediments in a relatively short time span (~670 yr; 1.4-0.8 ka) as result of the advance of Gualas Glacier over its proglacial lake and reworking of sediments stored there. The increase in Gualas river discharge during the Late Holocene is interpreted as having been caused by an increase in long-term (centennial - millennial scale) precipitation. This increase in precipitation most likely results from the intensification of the westerly winds in the area during the late Holocene (<1.4-4.2 ka), suggesting a widening of the westerlies wind belt and/or a northward shift of its core at this time.

Two recent periods of inter-annual sedimentation variability are characterized by abundant laminations with average recurrence time ~5-7 years. The first occurred during the interval ~790-490 cal yr BP (AD 1160-1460) and the second occurred during the interval ~270-60 cal yr BP (AD1680-1890). The associated inter-annual discharge variability suggests that a phenomena with a multiannual period, such as the El Nino Southern Oscillation (ENSO), affected the precipitation pattern of the area. Furthermore, these periods coincide with the two last Neoglacial periods in southern Patagonia (Neoglacial V and the Little Ice Age). We hypothesize that increased ENSO frequency might have a positive impact on the mass balance of Patagonian glaciers.

3.7 Acknowledgments

This research was funded by the National Science Foundation, Office of Polar Programs grant number NSF/OPP 03-38137 to J.A. and J.W. We thank the officers, crew, and scientists who sailed on the RV/IB Nathaniel B. Palmer during NBP05-05 in the Chilean Fjords. This research was also partly supported by an EU FP6 Marie Curie Outgoing Fellowship to S. B. In addition, we would like to thank the Instituto Antártico Chileno (INACH) for their support in obtaining permission to work in Chilean fjords. S.B. acknowledges Jan-Berend Stuut and Inka Meyer (MARUM, Bremen, Germany) for providing access to the Coulter grain-size analyzer. S. B. is currently a postdoctoral fellow of the Flemish Research Foundation of Belgium (FWO).

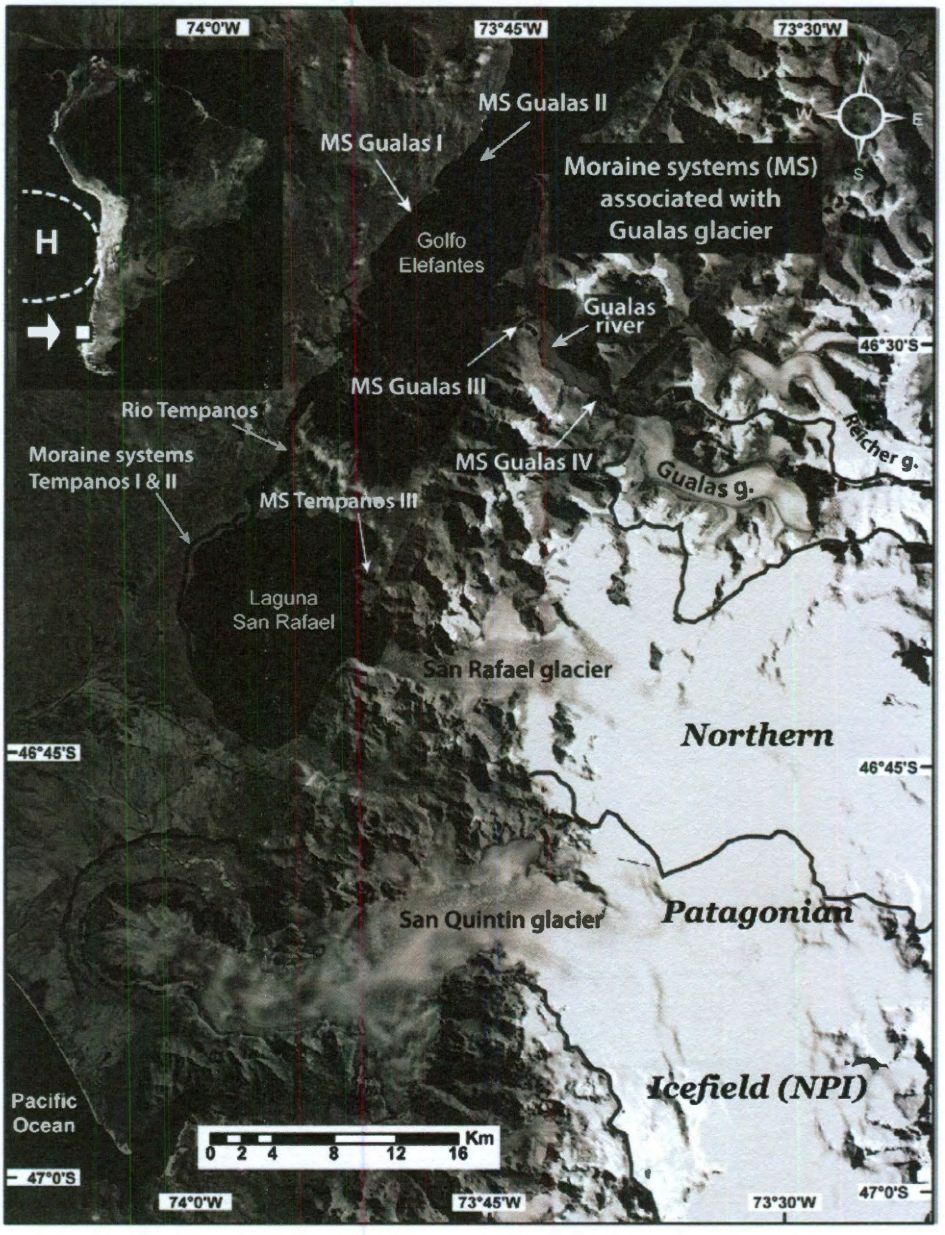

Figure 3.1. Location of the study area and main geomorphological features. The terminal moraines of Gualas, San Rafael, and San Quintin glaciers are shown by a black line (inferred Late Pleistocene to early Holocene age; see discussion section). The dashed lines inside the perimeter of the terminal moraines show the younger (presumably Holocene) moraine systems. Terminal moraine traces and glacier drainage basins were mapped using Landsat TM+ and Radar SRTM images of the area (http://edcsns17.cr.usgs.gov/EarthExplorer/). The inset shows the annual approximate locations of the SE Pacific high pressure system (H) and the position of the center of the westerly wind belt (white arrow).

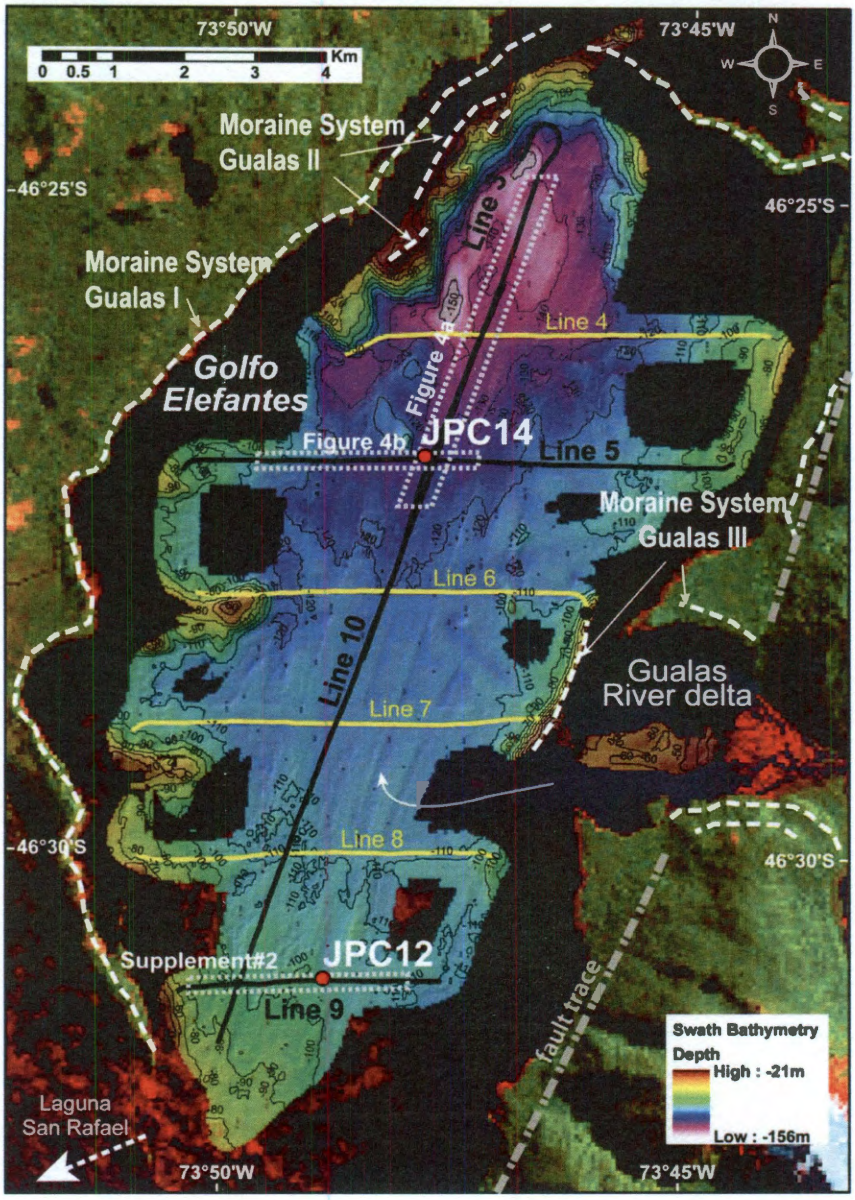

Figure 3.2. Swath bathymetry of Golfo Elefantes ("Elefantes" Gulf) (countour interval 10 m) and location of the air gun seismic lines used in this study. Black lines represent the seismic lines mentioned in the text and shown in figures 3, 4a,4b and Appendix B2. Yellow lines are those seismic lines that were used to estimate the volume of the seismic units used for the calculation of sediment discharge values (not mentioned in the text). The main moraine systems are shown in a dashed white line. The white arrow shows the direction of a modern sediment plume imaged by the background Landsat TM+ image.

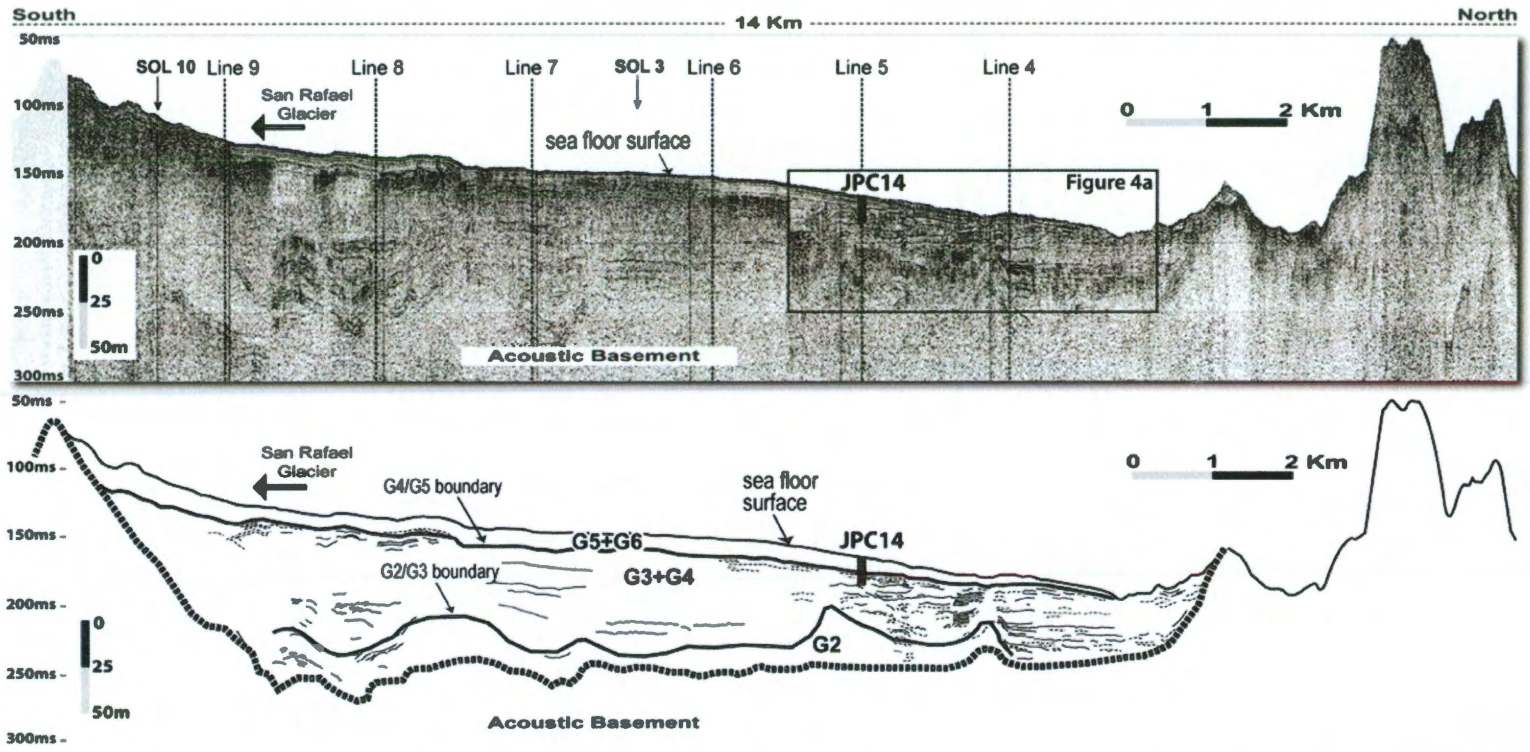

Figure 3.3. Combined air gun seismic records of lines 3 and 10, raw data and interpretation. The boundaries between units G3+G4 and G5+G6 and between G2 and G3 are shown by thick black lines. All relevant seismic boundaries were cross checked at the intersection of seismic lines. Also shown are the locations of cross lines and core JPC14. Vertical scale is estimated with Vp=1500 m/s. SOL3,10: start of line 3,10.

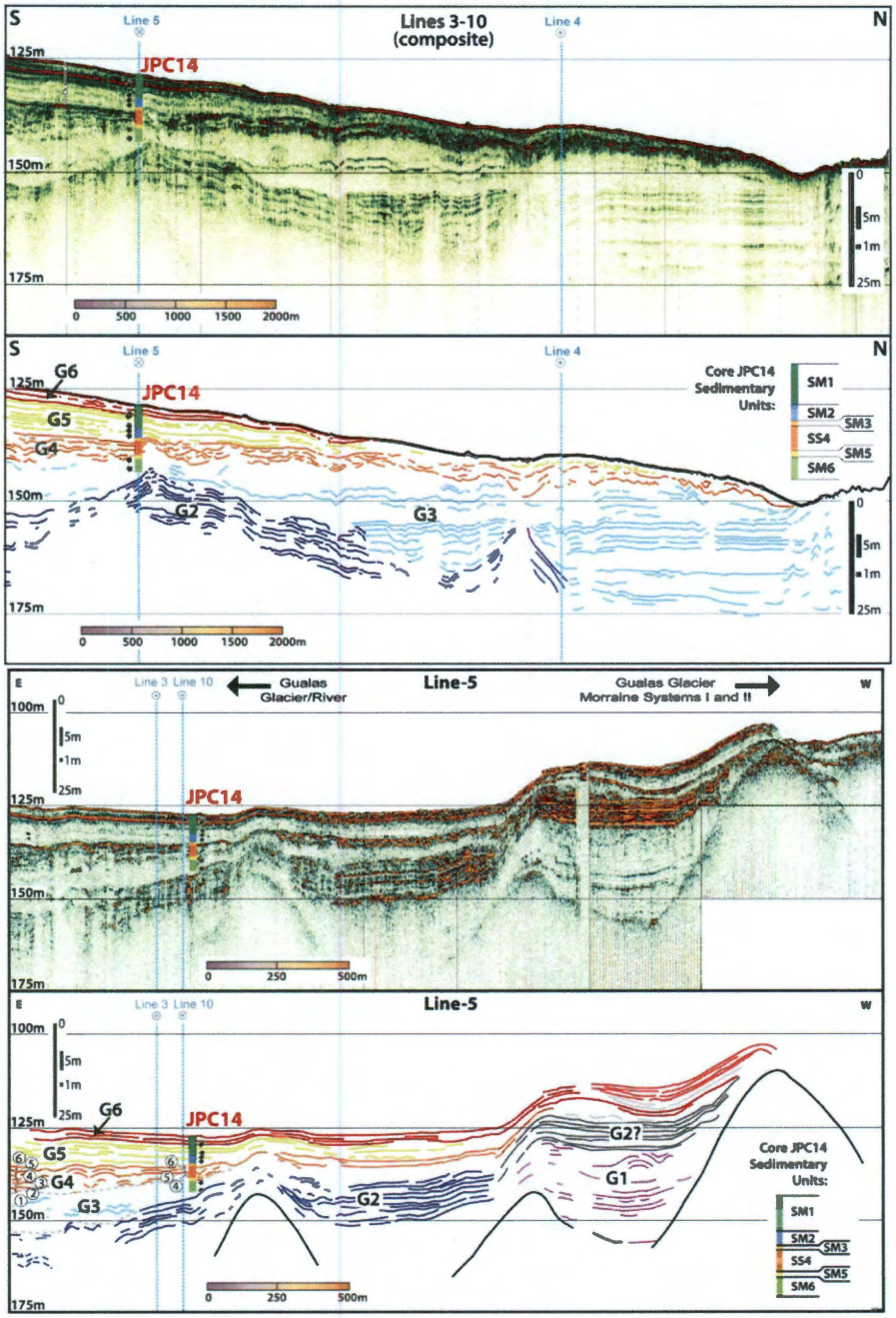

Figure 3.4. Sub-bottom profiler (chirp) records illustrating the stratigraphic architecture of Golfo Elefantes. The sedimentary units of core JPC14 (Figure 3.5) and the approximate depths of the samples used for radiocarbon analyses are also shown. Vertical scale is estimated using Vp=1500 m/s. (a) part of the composite section along lines 3 and 10, as shown in Figure 3.3.2; (b) part of the section imaged by Line 5; encircled numbers in unit G4 indicate the counting of "seismic" layers identified in this record.

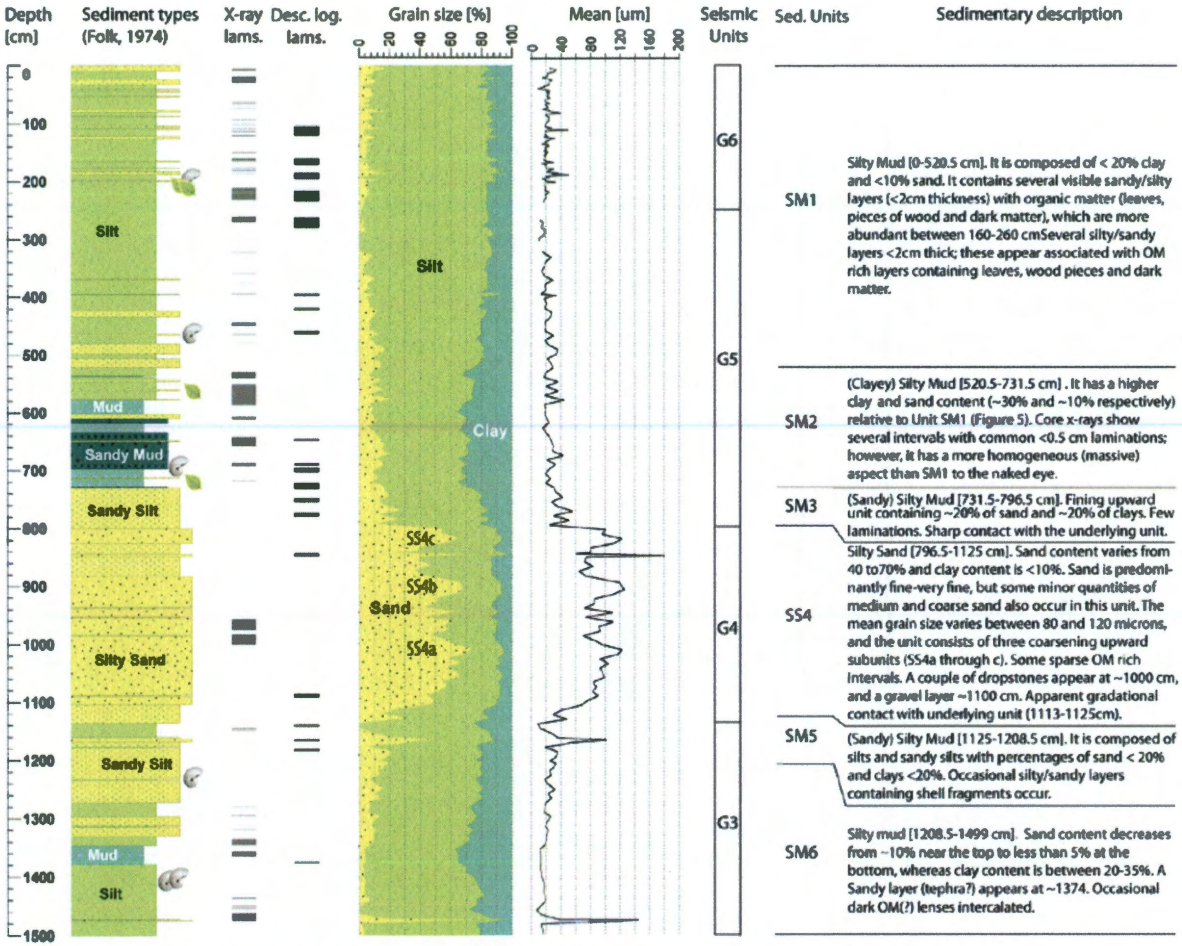

Figure 3.5. Sedimentology of core JPC14. Location of samples selected for radiocarbon analysis (leaves: plant material; shell: carbonate shells), laminations (lams.) and correlation with seismic units are shown. SS4a,b,c represent the three subunits identified within sedimentary unit SS4. Desc. log. lams.: laminations identified visually once the core was split for sedimentological description.

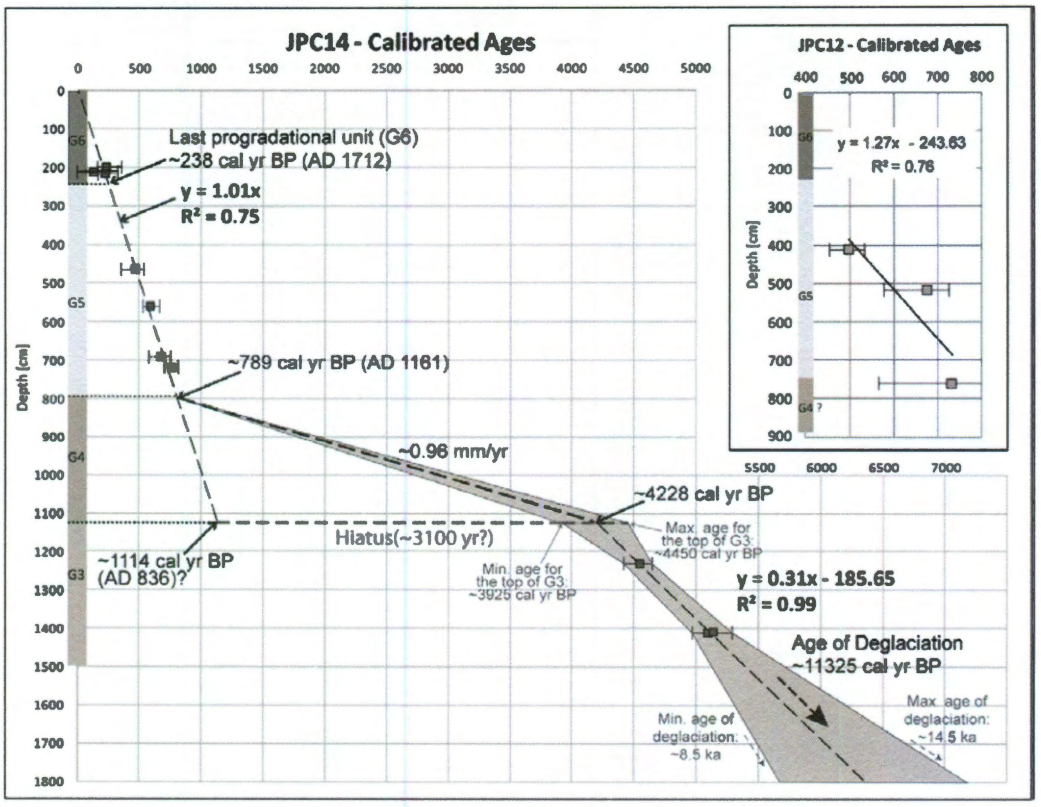

Figure 3.6. Age model for sediment cores JPC14 and JPC12. The ages of boundaries of seismic units G3, G4, G5 and G6 are shown for JPC14. For G4, two possible scenarios are given. One scenario assumes the same average accumulation rate as for the younger units and implies the existence of a 3100 yr hiatus between G4 and G3. The other scenario assumes no hiatus and result in an accumulation rate of ~0.96 mm/yr for unit G4. See text for discussion of the validity of these assumptions. For unit G3 minimum and maximum ages for the top and bottom are estimated based on the uncertainty of calibrated ages. For JPC12 the best linear fit curve for the three existing radiocarbon ages is shown.

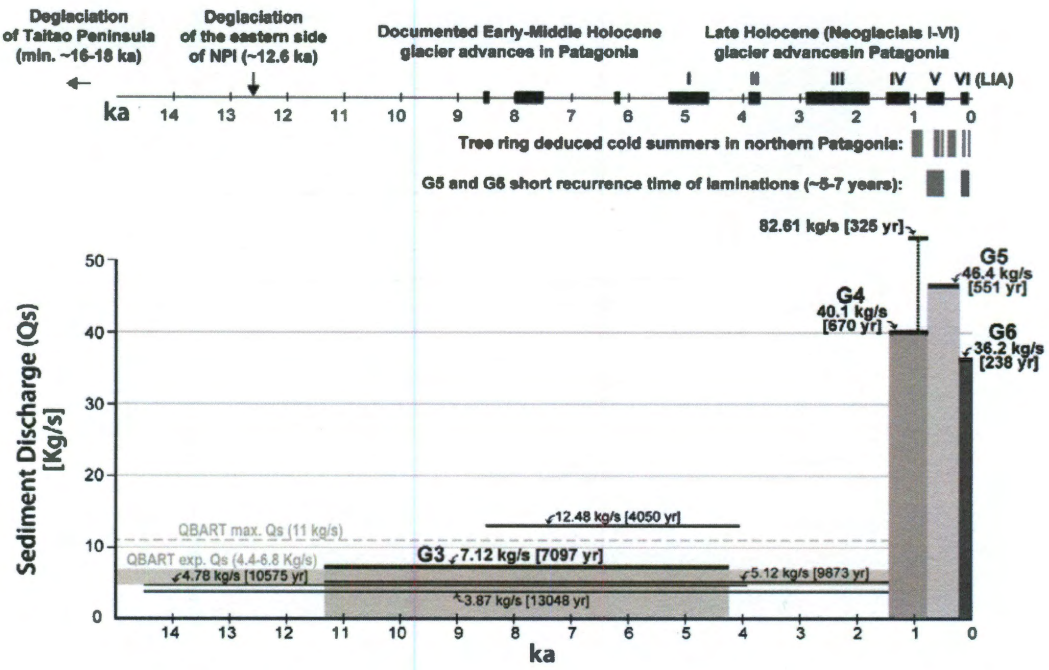

Figure 3.7. Volume equivalent sediment discharge for each seismic unit derived from the seismic analysis (centennial to millennial averages). For G4 (sandy unit) sediment discharge scenarios are based on the assumed extreme values of accumulation rates (10 mm/yr and 0.8 mm/yr as calculated from cores JPC14 and JPC12 respectively). The modern expected and maximum Qs intervals were estimated using the QBART model from Syvitski and Milliman (2007). As an example, different values of sediment discharge are shown for G3 based on different estimates of lower and upper age limits according to their estimated uncertainties (see Figure 3.6). Time intervals of the early Holocene glacier advances and Neoglacial periods in Patagonia as well as intervals of recent cold summers (from tree ring studies) and high frequency of laminations in core JPC14 are also shown (see text for details).

Chapter 4

Latitudinal variation of sedimentation and erosion rates from Patagonia and Antarctic Peninsula tidewater glaciers (46°-65° S)

Rodrigo A. Fernandez[1], John B. Anderson[1], Julia S. Wellner[2] and Rebecca L. Minzoni[1]

[1] Rice University, Earth Science Department, 6100 Main St, MS126, Houston, Texas 77005, USA

[2] University of Houston, Department of Earth and Atmospheric Sciences, Houston, Texas 77204, USA

Submitted November 2011:

Geology

Abstract

We estimate, based on sediment volumes accumulated in fjords, sediment erosion rates (Er) for millennial time scales across a broad latitudinal transect, from central Patagonia (46°S) to the Antarctic Peninsula (65°S). In the Antarctic peninsula, accumulation rates are ~10^0 mm/yr regardless of the time span of deposition (i.e. no "Saddler effect"). In Patagonia, proximal basins are in general well isolated and have short timescale (decadal-centennial) sedimentary records and high accumulation rates, whereas medial (more distal) basins have millennial scale sedimentary records and low accumulation rates. Erosion rates values span two orders of magnitude from 0.03 mm/yr for Lapeyrere Bay at Anver Island, Antarctica (~64.5°S), to 1.09 mm/yr for San Rafael glacier at northern Patagonia (~46.5°S). Rates for Antarctic Peninsula glaciers are in general lower than those of temperate Patagonian glaciers. A good correlation of erosion rates and modern sea level annual temperature was found. Latitudinal decrease in millennial erosion rates is interpreted as a result of decreasing annual temperature although decreasing annual precipitation is suggested. The pattern of published thermochronology ages, and the values of 10^3 and 10^6 year timescales erosion rates from our study, indicates that long-term glacial erosion decreases significantly in efficiency with latitude, implying that long-term glacial cover acts as a protective blanket, hindering erosion and allowing mountain growth, as previously suggested by other researchers.

4.1 Introduction

The indication that global sedimentation rates increased several times during the last 5 Ma (Hay et al., 1988; Peizhen et al., 2001; Molnar, 2004) and the evidence of multiple Quaternary glaciations from ice and marine sediments core isotope records (e.g. EPICA Community Members, 2004) have resulted in the common assumption that glaciers are more effective at eroding landscapes than rivers. This has further led to the argument that isostatic response of continental lithosphere to glacial erosion has resulted in accelerated Quaternary mountain uplift (Molnar et al., 1990). However, much debate still exists on this topic, a counter argument being that inferred higher rates of Quaternary uplift is perhaps more a product of higher rates of sediment production related to Quaternary climate variability (Molnar et al., 1990; Molnar, 2004; Whipple, 2009; Willenbring et al., 2010). Even more, the argument that sediment production has increased in recent geological time has been called into question due to the difficulty of accounting for hiatuses in the sedimentary record and the one-dimensionality of sediment-core based studies (e.g. Sadler et al., 1999; Schumer et al., 2009).

Recent studies have shown that estimated modern erosion rates are not representative of long-term (centennial, millennial or million-year time scales) trends and that erosion rates at longer than centennial time scales can be several orders of magnitude lower than estimates based on modern sediment yields (Delmas et al., 2009; Koppes et al., 2009; Fernandez et al., 2011a). Evidence exist that contemporary high sediment yields from tidewater glaciers might be the result of high ice fluxes associated with the retreat of modern glaciers from their last Neoglacial positions (Koppes and Hallet, 2002, 2006).

Regardless of the poorly constrained temporal association between glacier erosion and mountain uplift, glacier erosion is proposed to be a first-order control on mountain range exhumation and isostatic processes through the evacuation and removal of crustal material from orogens (e.g. Molnar et al., 1990; Montgomery et al., 2001; Blisniuk et al., 2006). A major challenge in understanding the effects of glacier erosion on mountainous regions is the paucity of unbiased measurements of denudation at time scales within the order of magnitude of tectonic processes and of quantification of first-order geological or climatic controls.

A primary control on glacier erosion rates is proposed to be the size of the drainage basin (Hallet et al., 1996; Koppes et al., 2009). These authors argued that modern glacier erosion rates are higher than fluvial erosion rates for small basins ($<10^2$ km^2) and lower than fluvial rates for medium size basins ($10^2 - 10^4$ km^2). However, Fernandez et al., (2011a) argued that the same datasets show a weak correlation between erosion rates and drainage basin area for glaciers from the same geographical region. This implies that other factors, such as geological/geographical setting, climate, and relief are be more important than drainage basin size in controlling erosion (Burbank, 2002; Fernandez et al., 2011a).

Efforts to construct a global dataset of glacier erosion rates (or equivalent sediment yields), as exists for fluvial sediment discharge (e.g. Milliman and Syvitski, 1992; Syvitski and Milliman, 2007), are hindered by a wide range of methodologies used

to determine glacial erosion (Delmas et al., 2009). Thus, existing datasets do not allow empirical first-order approximations of spatial variability of glacier erosion rates.

Our objective is to identify first-order control mechanism(s) and magnitude trends in glacial erosion by comparing glacier-fjord systems of regions with similar geological characteristics (lithologic assemblages and structural deformation) but different climatic settings. We estimated, based on sediment volumes accumulated in fjords, sediment erosion rates (Er) for millennial time scales across a broad latitudinal transect, from central Patagonia (46°S) to the Antarctic Peninsula (65°S). We present data from three glacier-fjord areas in Patagonia, San Rafael and Gualas area (~46.5° S), Europa Glacier area (~50.5° S) and Marinelli Glacier area (~55° S), and four glacier-fjord areas in the northern Antarctic Peninsula (<65° S), Maxwell Bay area (~62.2° S), Herbert Sound area (~64° S) and Lapeyrere and Andvord bay areas (~64.5° S) (Figure 4.1). We show that erosion rates are between 10^{0}-10^{2} mm/yr for temperate glaciers of Patagonia (similar to Alaskan glaciers; Hallet et al., 1996; Fernandez et al., 2011a), are in the order of 10^{-1}-10^{0} mm/yr for subpolar glaciers of northern Antarctic Peninsula (similar to published results from Svalbard; Elverhøi, 1995, 1998), and in the order of 10^{-2}-10^{-1} mm/yr for the polar to subpolar glaciers of the northern Antarctic Peninsula (Danco Coast). We also discuss million-year scale erosion rates calculated from sediment volume estimates from the continental shelf and slope of the central-northern Antarctic Peninsula. A comparison of the sediment volume derived erosion rates and thermochronology estimates of exhumation rates for Patagonia an Antarctica is also given.

4.2 Climate setting for the Patagonian Andes and the Antarctic Peninsula (~46-65° South)

The Patagonian Andes and the Antarctic Peninsula cordillera together form the most latitudinally extensive mountain range connecting middle and high latitudes. The westerly wind belt intersects both regions and, along with the cyclonic winds associated with the Antarctic Circumpolar Trough (ACT) in the Antarctic Peninsula, supplies moisture from the west to both regions (e.g. Anderson, 1999; Domack, 2003; Simmonds, 2003; Lamy 2010). The abrupt topography of these mountain ranges results in high (~>2000 mm/yr) but latitudinally variable precipitation that nourishes numerous westward flowing glaciers while the eastern side of the cordillera is characterized by drier and more continental climates (Schneider et al, 2003; Hulton et al., 2001; Reynolds 1981; Turner et al., 2002; Domack et al., 2003).

In western Patagonia, precipitation varies in relation to the distance from the core of the westerly winds and with altitude as the topography of the Andes exerts a strong orographic effect (Hulton et al., 2001; Schneider et al, 2003; Lamy 2010). Annual precipitation is >8000 mm/yr, likely reaching values over 10000 mm/yr at high elevations on the Patagonian icefields (46-52° S); to the south, at Cordillera Darwin in Tierra del Fuego Island (~54.5° S), maximum precipitation is 4000-6000 mm/yr (DGF-CONAMA Professional Report, 2006). Areas east of the Patagonian Andes are drier with annual precipitation <500 mm/yr (Hulton et al., 2001; DGF-CONAMA Professional Report, 2006). Mean annual temperatures near sea level decrease by ~0.5 °C per degree of latitude (a.k.a. latitudinal lapse rate), from ~10 °C at ~46° S to ~6 °C at ~55° S. However,

at higher altitudes large areas stay below ~4 °C and high peaks stay below freezing year round (DGF-CONAMA Professional Report, 2006).

In the western Antarctic Peninsula, precipitation at high plateaus and ice domes diminishes from more than 2000 mm/yr at the latitude of Anvers Island (~65° S) to ~500 mm/yr at the northern tip of the peninsula (~63.5° S) (Turner et al., 2002). At King George Island in the South Shetland Islands (Figure 4.1), precipitation reaches ~1200 mm/yr on the main dome summit. The eastern side of the Peninsula is under the rain shadow effect of peninsular mountains that block most of the moisture brought by westerly cyclones and receives dry air advected from higher latitudes (Smith et al., 1996; Turner et al., 2002; Domack et al., 2003). Precipitation comes mostly from the western Weddell Sea, but is only one third of the amount of precipitation on the western side of the peninsula at comparable latitudes and altitudes (Turner et al., 2002).

In the northern part of the Antarctic Peninsula (latitudes <~65° S), temperature measurements exist only from weather stations located in coastal areas. These stations show that temperature has increased at a rate of ~0.33 °C/°latitude between the beginning of the 1970's and the last 15 years, from an increase of ~1.8 °C at ~65° S to an increase of ~1 °C at ~63° S (Appendix C1). A slightly smaller increase of ~0.8 °C has occurred over the same time period at Bellingshausen Station in the South Shetland Islands (Appendix C1). A maximum temperature increase of ~1.5 °C has been measured at Marambio Station on Seymour Island (Figure 4.1) eastern of the peninsula, and at Faraday Station, located on the western side of the peninsula at ~65°S on the Danco Coast. On the western side of the peninsula the latitudinal lapse rate for coastal areas is ~-0.5 °C/°latitude north of ~65° S (Appendix C1), much less than on the eastern side where

this lapse rate is ~-1.4 °C/°latitude (Morris and Vaughn, 2003). Altitudinal lapse rate for the western side of the Peninsula is 0.72-0.74 °C/ 100 m (Reynolds, 1981; Morris and Vaughn, 2003).

4.3. Methods

Glacier erosion rates were calculated by estimating the volume of sediments deposited in fjords and bays following the method outlined by Fernandez et al. (2011a). The method uses swath bathymetry to map the sea floor, and seismic records for mapping sub-sea floor surfaces that are recognizable over an entire fjord or bay. The volumes of sedimentary units bounded by these surfaces are estimated and converted to source rock-equivalent volumes. Finally, the rock-equivalent volumes are distributed (divided) over the effective drainage basin and the total time span of accumulation of the sediments that comprises each unit.

The swath bathymetry data was collected by the RV/IB Nathaniel B. Palmer (NBP) in several cruises, including NBP0505 for the Patagonian fjords, and from cruises NBP0201, NBP0703 and NBP0502 for the Antarctic fjords and bays. Seismic records comprising high frequency (3.5 kHz) chirp data from two different sub-bottom profiler systems available on the NBP (Knudsen and Bathy200), along with sparker, water gun and air gun single channel (lower frequency) seismic data collected by the NBP and by earlier (1980's and 1990's) cruises on the USCGC Glacier (Deep Freeze 1986) and the RV Polar Duke (PD91). Basin-wide seismic units were mapped, digitazed and cross

checked at intersection points of navigation track lines as well as between different source records. In this way, a "latitude/longitude/depth" dataset was generated for each seismic boundary, then interpolated and rasterized following Fernandez et al. (2011a). A p-wave velocity (Vp) ranging between 1500 and 1700 m/s was used to convert time to depth on the seismic records.

To obtain source rock-equivalent volumes we used the following equation:

$$Vol_{Rx} = (\rho_{sed} / \rho_{source}) Vol_{Sed}$$

where,

ρ_{sed} = average density of the sediments, [kg/m^3].

Vol_{Sed} = volume of sediments of each seismic unit, [m^3].

Vol_{Rx} = source rock-equivalent volume of sediments, [m^3].

ρ_{source} = estimation of the average density of the source rocks, [kg/m^3].

The density used for the parental rock (ρ_{source}) was 2700 kg/m^3, which is a common value used for metasedimentary and igneous rocks. The density of the sediment was not directly measured, but the interval 1600-1800 kg/m^3 that contains the most probable values was derived from previous studies (Michalchuk et al., 2010; Hamilton, 1982) following Fernandez et. al (2011a).

To constrain the timespan of accumulation of each seismic unit "t", a number of radiocarbon ages were used to estimate linear accumulation rates and thus inter- or extrapolate the most likely age of seismic reflections bounding seismic units. For two of

the Patagonian glacier/basin systems (Marinelli Glacier and San Rafael-Gualas Glacier areas; Figure 4.1) and one South Shetland Island basin (Maxwell Bay; Figure 4.1), the ages were previously published (Boyd et al., 2008 and Fernandez et al., 2011b) and (Milliken et al., 2009), respecively.

Hence, the basin and time average erosion rate is given by $\langle Er \rangle = (1/t)\ (1/A_{dr})\ Vol_{Rx}$, where A_{dr} is the effective drainage basin area including all areas that potentially supplied sediment to the fjord or bay.

4.4 Results

The most remarkable difference between the sedimentary sections of Patagonian and Antarctic Peninsula fjords and bays as seen in the seismic records is the geometry and nature of the early infilling of these basins (Figure 4.2). In the Antarctic Peninsula depositional systems, subhorizontal parallel reflections onlap the acoustic basement (Figure 4.2a) with no evidence of progradation of the bottom units. In Herbert Sound, the bottom unit, interpreted as subglacial till, has almost a constant thickness across the sound. In contrast, Patagonian sedimentary sections show bottom units with progradational geometries that thin over relatively short distances (<5km) (Figure 4.2b).

These bottom units prograde away from acoustic basement (bedrock?) highs and are interpreted as morainal bank deposits formed during glacier retreat while the glacier was pinned on these highs (Figure 4.2). This implies that subglacial sediment flux was higher in the temperate Patagonian glaciers and/or retreat rate of the grounding line was

slower than in the Antarctic glaciers, which allowed for building of morainal bank depostis at pinning points in the Patagonian systems. Nevertheless, these bottom units were not sampled or dated, and the sediment flux or accumulation rates associated with them were not calculated. Thus, these units were not included in the volume calculations since they constitute a minor fraction of the total volume accumulated in the depositional basins where they are present (Patagonia), and because time spans of accumulation were estimated only for the glacimarine units. The results and following discussion focus only on the glacimarine sedimentary units deposited above these progradational units.

The first approximation of the amount of sediments that have been delivered to fjords and bays since their deglaciation is linear accumulation rates. Table 4.1 shows the estimated linear accumulation rates for all the fjords and bays included in this work. In general, accumulation rates do not show any simple pattern with latitude, although they vary by as much as four orders of magnitude for the temperate Patagonian glaciers (10^{-1} – 10^{4} mm/yr) but vary within one order of magnitude for the subpolar/polar glaciers of the Antarctic Peninsula (~10^{0} mm/yr;). The only exception is Maxwell Bay where a rate of 26 mm/yr was determined for the early Holocene (Milliken et al., 2009). However, for Antarctic Peninsula fjords, there is a pattern of decreasing accumulation rates with latitude (Figure 4.3a).

We investigated the possible relationship between accumulation rates and the timespan of accumulation and the distance from the present day ice front. Figure 4.3b shows that, with respect to timespan, accumulation rates might vary within one or more orders of magnitude but maximum values are constrained by a power-law curve indicating that long timespans (10^{3} – 10^{4} years) would record low accumulation rates

whereas at shorter timespans (<10^3 years) higher accumulation rates of (up to four order of magnitude higher) could be measured. A similar relationship was found between accumulation rates and distance from the present day ice front (Figure 4.3c). Values of accumulation rate spread over four orders of magnitude at less than 10 km from the ice front, reaching 10^4 mm/yr, but decrease rapidly with distance away from the ice front, implying that at distances larger than ~40 km accumulation rates would only reach up to 1 mm/yr (Figure 4.3c).

Table 4.1. Sedimentation rates and information on the dataset data used for their calculation.

Area	Sed rate [mm/yr]	time interval [min.age	max.age]	core/cruise of seismic survey	Lat	Long	core type	Number of 14C dates	dist from ice front [km]
Gualas g.	10.10	220	740	NBP0505 JPC14	-46.449	-73.798	piston cores	7	18
Gualas g.	2.70	0	11300	NBP0505 seismic survey	-46.449	-73.798	---	---	18
San Rafael g. (1)	410.79	1871	1959	NBP0505 seismic survey	-46.667	-73.941	---	---	7.6
Europa g.	1.20	370	10700	NBP0505 JPC37	-50.057	-74.343	piston cores	8	50
Europa g.	2.00	1480	4800	NBP0505 JPC32	-50.185	-74.211	piston cores	4	31
Marinelli g. (2)	3500.00	1960	2005	NBP0505 seismic survey	-54.456	-69.619	---	---	5
Marinelli g.	28.00	160	230	NBP0505 JPC52, JTC70, JPC63	-54.362	-69.582	piston cores	3	5
Marinelli g.	0.56	100	15500	NBP0505 JPC67, JPC77	-54.260	-69.626	piston cores	16	22
Herbert sound	1.20	700	2000	NBP0502 2C	-63.971	-57.759	kasten core	4	12.8
Herbert sound	1.80	5000	7000	NBP0502-2B	-63.971	-57.759	drill core	4	12.8
Herbert sound	4.20	6500	9000	PD91-08	-63.979	-57.775	piston core	5	11.8
Herbert sound	1.14	0	9300	NBP0502-2B	-63.971	-57.759	drill core	4	12.8
Firth of Tay	9.60	0	3500	NBP0602-X8 and NBP0703-JPC02	-63.343	-55.887	kasten, piston and drill core	14	5.3
Firth of Tay	7.30	3500	9400	NBP0602-X8 and NBP0703-JPC03	-63.343	-55.887	kasten, piston and drill core	19	5.3
Maxwell Bay	5.30	1000	7000	NBP0502-1B	-62.282	-58.754	drill core	15	12.3
Maxwell Bay	12.70	7000	9400	NBP0502-1B	-62.282	-58.754	drill core	14	12.3
Maxwell Bay	7.42	0	14500	NBP0502-1B	-62.282	-58.754	drill core	29	12.3
Lapeyrere Bay	2.70	0	1600	NBP0703-JPC35	-64.335	-63.098	piston core	1	17.2
Lapeyrere Bay	2.80	500	1500	NBP0502-6D	-64.392	-63.250	kasten core	4	7.6
Lapeyrere Bay	1.30	1500	8000	NBP0502-6E	-64.392	-63.250	drill core	4	7.6
Andvord Bay	2.80	80	400	NBP0703-KC57	-64.872	-62.425	kasten core	5	1.8
Andvord Bay	4.90	400	800	NBP0703-KC55	-64.781	-62.870	kasten core	4	18
Andvord Bay	3.10	500	4500	NBP0703-JPC56	-64.781	-62.870	piston core	5	18
Beascochea	1.31	0	4000	NBP0703-KC42	-65.591	-63.817	kasten core	2	1

Note: Gualas g. rates and time span are from Fernandez et al., 2011b; (1) Idem from Koppes et al. (2009b); (2) Idem from Koppes et al. (2010).

The volume of sediments accumulated in fjords and bays across the study region does not show any clear trend with latitude (Figure 4.4; Table 4.2). Most of the fjords and bays have accumulated 1-10 km^3 of sediments with only two exceptions: San Rafael

Glacier depositional basins (Patagonia), where approximately 16.1 km^3 accumulated in its proglacial lagoon (Laguna San Rafael) and in a more distal basin we informally call "San Rafael Glacier intermediate basin" (Appendix C2); and Lapeyrere Bay in the Antarctic Peninusla, where only ~0.1 km^3 of sediments were deposited in the main fjord and in a small embayment we informally call "the thumb" (Appendix C2). However, polar glaciers, such as those feeding Andvord Bay, Lapeyrere Bay and Herbert Sound, have accumulated in their proglacial basins significantly less sediments than any other subpolar or temperate systems (Figure 4.4).

The sediments of the Antarctic Peninsula fjords and bays can have a significant proportion of biogenic material, and thus the actual volume of siliciclastic material is a fraction of the total volume of post glacier retreat accumulation. The only areas where biogenic percentages have been estimated are Maxwell and Andvord bays. Average total biogenic material in Maxwell Bay is ~6.3 wt% based on TOC (0.3 wt%) and biogenic silica (~6.0 wt%) percentages obtained in a 108 m long drill core that sampled the entire post retreat sedimentary section (Milliken et al., 2009). In Andvord Bay, biogenic flux can be up to 30 wt% of the total sediment flux (Mammone, 1992), but analysis of the sediments accumulated at the sea floor show that only a fraction of this flux is preserved since only about 15-20 wt% of the sediments consist of biogenic material (Mashiotta, 1992). Discounting the biogenic content results in a total volume of siliciclastic sediments accumulated in Andvord Bay of about 1.1 km^3. Ongoing studies of Lapeyrere Bay and Herbert Sound indicate that percentages of biogenic material is relatively low at Lapeyrere Bay (<5%), but can be as high as ~20% in Herbert Sound. As shown in Figure 4.4, the percentages of biogenic material accumulated in those bays and fjords have little

influence on sediment volumes. For the Patagonian study areas, visual inspection of cores indicates that the percentage of biogenic material is lower than any of the studied Antarctic areas.

Table 4.2 Time and basin wide average erosion rates (<Er>) and the climatic parameters used.

Glacier	Latitude (S)	volume [m^3]	density ratio	Dranaige basin [m^2]	Time Interval [yr]	<Er> [mm/yr]	Mean annual t° 1995-recent [C]	Mean annual t° ~1970 [C]	Mean annual ppt [mm]
Gualas	46.5	1.592366E+09	0.63	1.704263E+08	11300	0.52	10.0	10.0	4000
San Rafael	46.5	1.605229E+10	0.63	7.243473E+08	12800	1.09	10.0	10.0	8000
Europa	50.5	1.670269E+09	0.63	4.576689E+08	12500	0.18	8.0	8.0	8000
Marinelli	55.0	2.760094E+09	0.63	2.665200E+08	12500	0.52	6.0	6.0	4000
Maxwell Bay	62.2	3.963912E+09	0.63	2.949211E+08	13000	0.61	-2.0	-3.0	1249
Herbert Sound	64.0	1.159913E+09	0.63	3.841884E+08	8511	0.18	-7.8	-9.0	700
Lapeyrere Bay	64.5	1.151572E+08	0.63	2.501956E+08	10500	0.03	-2.5	-4.0	2000
Andvord Bay	64.5	1.387765E+09	0.63	5.539218E+08	10500	0.12	-2.5	-4.0	2900

Erosion rate values span two orders of magnitude from 0.03 mm/yr for Lapeyrere Bay (~64.5°S) to 1.09 mm/yr for the San Rafael area (~46.5°S; Figure 4.5; Table 4. 2). Although quite variable, there is a clear trend of decreasing values of erosion rates with latitude (Figure 4.5). The best fit curve shows increasing R^2 values from 0.40 to 0.60 if Maxwell Bay is excluded from the interpolation (Figure 4.5). This is a power law with exponent -6.3, meaning that erosion rates decreases steadily with latitude, reaching values lower than 0.1 mm/yr at latitudes higher than ~64°S. If further refinement is made so that only areas with well isolated basins are considered (San Rafael Glacier area, Marinelli Glacier area, Herbert Sound and Andvord Bay), so that the effects of sediment loss are minimized, a linear pattern of decreasing <Er> with latitude and high fit (R^2=0.98) is obtained (Figure 4.5). The negative slope of the linear interpolation implies that <Er> decreases about 5% per latitude degree (Figure 4.5).

4.5 Discussion

4.5.1 Accumulation rates

Our results show that accumulation rates in bays and fjords along the studied latitudinal transect vary over several orders of magnitude (Figure 4.3A). Despite of their different climate, millennial-scale accumulation rates for Patagonian and Antarctic Peninsula glaciers are within the same order of magnitude (~10^0 mm/yr; Figure 4.3A). We interpret this as being due to: a) a modulated expression of the so called "Sadler effect" (Sadler, 1999), in other words, that the relative proportion of hiatuses vs accumulation periods in the sedimentary section results in similar low accumulation rates (~10^0 mm/yr) for Patagonian and Antarctic Peninsula glaciers; and/or b) a bias produced by the selection of coring sites and/or the maximum length of cores. The latter is based on the fact that millennial-scale accumulation rates are obtained from sedimentary sections that occur at some distance from the ice front where accumulation rates are low enough to record millennial scale sedimentary processes. This effect is of greater importance for the Patagonian fjords as indicated by the stronger dependence of timespan on distance from the ice front (Figure 4.3D). The "Saddler effect" is evident when plotting accumulation rates vs timespan of deposition. For the Antarctic systems, accumulation rates are ~10^0 mm/yr regardless of the time span of deposition (i.e. no "Saddler effect"; Figure 4.3B). This indicates that the same accumulation dynamics (sedimentation versus non-deposition or erosion) have dominated the Antarctic fjords and bays at millennial timescales during most of the Holocene (the best represented period on our cores; Appendix C3). Hence, the Holocene climate variability in the northern

Antarctic Peninsula (e.g. Middle Holocene Blimate Optimum and Neoglacial) suggested by recent studies (Domack et al. 2001, 2006; Milliken et al., 2009; Michalchuk et al., 2009), had little impact on the accumulation dynamics on fjords and bays.

Accumulation rates do not relate to distance from the present day ice front in a simple fashion. Particularly, at distances less than 10 km, accumulation rates vary over four orders of magnitude (10^0-10^3 mm/yr), the largest values corresponding to the temperate Patagonian glaciers whose rates reach values of 10^2-10^3 mm/yr in the proximal basins of San Rafael and Marinelli glaciers (Table 1; Figure 2c). These proximal basins have restricted circulation and are connected to the sea by shallow (few meters deep) passages that restrict the amount of sediments that can escape the fjord (e.g. Fernandez et al., 2011a). Since these proximal basins were occupied by ice during the Little Ice Age (LIA) (Boyd et. al, 2008; Koppes et al., 2009b; Koppes et al., 2010), the estimated accumulation rates represent relatively short timescales (10^1-10^2 years). For this reason all the cores where centennial and millennial accumulation rates were estimated are located in basins that are at some distance from the present day ice front (>5-12 km approx.). These basins (from now on referred as "medial basins") have semi-restricted circulation and are not directly connected to the open sea (not influenced by oceanic currents). Summarizing, Patagonian proximal basins have short timescale (decadal-centennial) sedimentary records and high accumulation rates, whereas medial basins have millennial scale sedimentary records and low accumulation rates.

Unlike Patagonia, none of the Antarctic Peninsula depositional basins have well isolated proximal basins. Rather sills separating individual basins in Antarctic fjords and bays are typically hundreds of meters deep. Our bathymetry, cores and sub-bottom

profiler data show that sediment accumulation has indeed occurred in proximal basins within fjords (e.g. Andvord Bay's NE fjord and Marion Cove in Maxwell Bay) although the timespan of accumulation and overall linear accumulation rates were not estimated because of the absence of datable material and uncertainty as to the thickness of the sedimentary section. However, the small size of these proximal basins (<25% of the area of proximal Patagonian basins) and the fact that only a portion of the total basin area has experienced sedimentation, suggests that accumulation rates are significantly less than for the Patagonian proximal basins. Thus, most of the sediment is accumulated in the medial basins (main bays and fjords), where basin-wide, sub-horizontal seismic reflections occur. This indicates efficient sediment dispersion and settling from suspension as the main sedimentation mechanism. Hence, we find fairly constant sedimentation rates throughout large areas (Figure 4.3C).

4.5.2 Erosion rates

Erosion rate values span two orders of magnitude from 0.03 mm/yr for Lapeyrere Bay area to 1.09 mm/yr for San Rafael area in northern Patagonia (~46.5°S). The lesser spread on erosion rates (<Er>) with respect to accumulation rates (Ar) values is attributed to two main factors. First, unlike Ar, <Er> are calculated from the estimation of a 3D parameter, volume of sediments accumulated in a certain basin, which diminishes the effect of local sediment bypass, heterogeneous dispersion of sediments within the basin and local sediment dynamics (reworking, concentration or erosion) that commonly affect one dimensional Ar. Second, the volumes used to calculate <Er> are averaged over long

time spans and large drainage areas, which diminishes the impact of volume variability. Volume derived <Er> can however be affected by basin-scale sediment bypass or erosion, large scale storage of sediments within the sub- and en-glacial environment or in proximal or proglacial basins.

4.5.3 Patagonian Glaciers

Patagonian Glaciers are characterized by relatively high erosion rates. A general pattern of decreasing millennial timescale <Er> with latitude is evident, although some spread exists in the data. Because San Rafael and Marinelli glaciers have the most efficient sediment sinks, i.e. well isolated depositional basins, erosion rates for Gualas and Europa glaciers, whose depositional basins have less trapping efficiency, might be underestimated due to sediment bypass and storage.

The Gualas Glacier proglacial fluvial system stores at least ~0.14 km^3 of sediments while an unknown amount has been stored in its proglacial lake since the glacier retreated from its Little Ice Age maximum position. Additionally, some sediment might have bypassed the Gualas Glacier main accumulation basin, Golfo Elefantes (Appendix C2). However, as much as 1.4 km^3 of sediments need to be accounted for and added to the volume already included in our calculations to obtain an <Er> value similar to that estimated for the nearby San Rafael Glacier. Such a volume of sediment would be about ten times the estimated volume of sediment stored in the Gualas Glacier proglacial fluvial system. We consider this an unlikely scenario, so other factors such as glacier

dynamics, slope, fracturing etc.) should be more influential in producing the remarkably lower <Er> for Gualas Glacier compared to San Rafael Glacier.

Europa Glacier yielded a relatively low <Er> value compared to the rest of the Patagonian glaciers. This glacier calves into a long (~60 km) and narrow (2-3 km) fjord (Europa Fjord) that has no shallow sills or moraines (depth >100 m for most of the fjord). Chirp seismic data shows prominent depressions on the sea floor surface. These depressions are usually 2-10 meters deep, being up to 22 m deep in some areas, and are interpreted as erosional features produced by strong tidal currents. Since there are no obvious sediment sinks within the drainage basin of Europa Fjord, erosion and advection of sediments out of the fjord is a possible cause of underestimation of the volume of sediments and <Er> produced by Europa Glacier.

Figure 4.6 shows the hypsometry of San Rafael, Europa and Marinelli glaciers as well as estimated modern and LGM equilibrium line altitudes (ELA). Europa Glacier hypsometry, unlike San Rafael and Marinelli glaciers, implies that the accumulation area ratio (AAR; the fraction of the total glacier area where there is net accumulation) is relatively more insensitive to vertical displacements of the ELA (Figure 4.5). Thus, elevation of the ELA during interglacial periods would have a smaller impact on the mass balance and the dynamics of Europa Glacier. As shown for other Patagonian and Alaskan glaciers, erosion rates correlate with retreat rates (i.e. negative mass balance; Koppes et al., 2002, 2006, 2009, 2010) and might also increase with glacier fluctuations (Fernandez et al., 2011a). We hypothesize that Europa Glacier has had a lower sediment production (i.e. low erosive power) due to its relative stability (mass balance and ice dynamics) throughout the Holocene.

The bottom units prograde away from acoustic basement (bedrock?) highs and are interpreted as morainal bank deposits formed during glacier retreat while the glacier was pinned on these highs.

4.5.4 Antarctic Peninsula glaciers

Erosion rates obtained for the Antarctic Peninsula glaciers are in general lower than those of temperate Patagonian glaciers (Figure 4.5). The most dramatic exception are the glaciers that feed Maxwell Bay, which yielded <Er> ~0.61 mm/yr. This value is only surpassed by the <Er> estimated for San Rafael Glacier in northern Patagonia. Additionally, on the <Er> vs Latitude plot (Figure 4.5), the best fit curve improves its R^2 from 0.4 to 0.6 if Maxwell Bay is removed from the calculation. Thus, the Maxwell Bay <Er> value is interpreted as anomalously high for its latitude. The question that arises is why do Maxwell Bay glaciers erode as fast as the temperate Patagonian glaciers?

The ice that flows into Maxwell Bay drains part of King George Island Ice Cap (KGIIC). This ice cap is regarded as sensitive to climate change due to its small size and low elevation (<700 m; Ruckamp et al., 2010). According to ground-penetrating radar (GPR) studies by Blindow et al. (2010), the ice cap is temperate up to at least the surface isohypse 400 mamsl (meters above mean sea level) and cold above this elevation, meaning that KGIIC is a polythermal ice body. The ice flowing into Maxwell Bay is below ~645 mamsl, with only ~15% of its surface area above the isohypse 400 mamsl,

indicating that, for the most part, the ice flowing into Maxwell Bay is a temperate ice body. According to Knap et al. (1996), the present day ELA at KGIIC is ~100 mamsl, meaning that ~82% of the ice surface draining into Maxwell Bay corresponds to accumulation area (AAR~ 0.82). However as temperature rises on the island (it has increased 0.8+-0.2 C since 1970; Appendix C1) the ELA will presumably rise as well, affecting the mass balance of KGIIC. Hence, temperate ice physical conditions and high glacier sensitivity to climate changes, which translate into active glacier dynamics, might explain why the erosion rates obtained for Maxwell Bay are similar to values obtained for the temperate glaciers of Patagonia.

The lowest <Er> value was obtained for Lapeyrere Bay (0.03 mm/yr). Neighboring Andvord Bay yielded four times this value (0.12 mm/yr). Differences in basin and glacier configuration might explain this difference. Lapeyrere Bay is an elongated fjord with no shallow sills. It has efficient down-fjord transport of sediments and the thickness of the sedimentary section diminishes away from the ice front (Griffith et al., 1989; Domack et al., 1993). These characteristics indicate that some sediment may be advected out of the fjord, and thus was not accounted for in our volume calculations. On the otherhand, Andvord Bay is a large embayment with a complex morphology, including prominent lows and highs, with an eddy like circulation that distributes sediments within the embayment (Domack et al., 1993). This makes Andvord Bay a better sediment trap than Lapeyrere Bay. This means that the volume of sediments produced in these areas might be more underestimated at Lapeyrere Bay than at Andvord Bay.

The glaciers draining into Lapeyrere and Andvord bays also show significant differences. The hypsometry curves for these bays are remarkably asymmetrical, with the peak of area distribution at low elevations for Lapeyrere Bay (300-700 masml) and at high elevation for Andvord Bay (1500-1700 masml) (Figure 4.7). This implies that an elevation in the regional ELA would have a greater effect on the mass balance of Lapeyrere Bay glaciers. However, the main difference is the configuration of glaciers. Whereas Lapeyrere Bay is fed with sediments mainly by a single large valley-type glacier (Illiad Glacier) and to a lesser extent by a few cirque and headland glaciers (Griffith et al., 1989), Andvord Bay is fed by a greater number and variety of glaciers. Four large outlet glaciers are located at its eastern end (Domack et al., 1993), and a number of small cirque, headland glaciers and ice aprons occur all along its coast. The lower 50% of the glaciated areas of Lapeyrere Bay have lower average slope (~9° for areas <900 masml) relative to Andvord Bay (~19° for areas <1200 masml; Figure 4.7). Glaciers calving fronts occupy about 20 km in Andvord Bay but not more than 12 km in Lapeyrere Bay. Thus, the greater erosion rates and sediment production at Andvord Bay are explained by the greater number of glaciers, higher low-elevation slopes and greater overall calving front length.

The estimated erosion rate for the Herbert Sound area (0.18 mm/yr) is higher than that of Lapeyrere and Andvord bays. Like Andvord Bay, the configuration of the areas draining into Herbert Sound is complex with several calving ice fronts. The hypsometry maximum is reached at low elevation (<300 masml) and 50% of the drainage area is below 600 masml but slopes are on average ~8-9 degrees similar to Lapeyrere Bay. One of the most important differences between the Herbert Sound area and the rest of the

studied Antarctic Peninsula areas is the large area with no ice cover where large amounts of sediments are stored. Sediment is also stored in submarine fans that protrude from some bays as indicated by satellite imagery. All of the above imply that sediment volumes have been underestimated and that erosion rates can be much higher than our estimates, implying that the difference of <Er> between Herbert Sound and Lapeyrere and Andvord bays is even greater. However, the lithology of James Ross Island (JRI), the drainage basin for the glaciers feeding Herbert Sound, is different from the rest of the studied areas. James Ross Island is dominated by a large polygenetic strato volcano whose volcanic sequences rest unconformably on tilted Creataceous marine sediments (Bibby, 1966; Nelson, 1975; Smellie 1990, 2006). In addition, there is evidence that the past JRI ice cap was wet-based, being either temperate or polythermal during deposition of volcanoclastic deltas (Hambrey and Smellie, 2006; Hambrey et al., 2008; Smellie, 2008). Whether the thermal state of JRI ice cap during the Holocene was at some point polythermal or temperate is not known. Hence, lower bedrock resistance to erosion and perhaps temperate ice conditions explain the relatively high erosion rates obtained in the Herbert Sound area.

4.5.5 Origin of Latitudinal decrease in millennial scale erosion rates

Roughly similar Mesozoic and early Cenozoic geological history of south western Patagonia and northern Antarctic Peninsula has result in similar assemblages of rock outcrops and magnitude of deformation for the two areas (Anderson, 1999). This allows direct comparison of erosion rates between these two regions in terms of processes that

influence glacier dynamics and sediment production. Since our study areas span a broad latitudinal range, the main climatic parameter influencing ice dynamics is temperature. Because temperature decreases almost monotonically with latitude, a good correlation of <Er> and modern (estimated sea level annual 1970 temperature; Appendix C1) sea level annual temperature was found. However, the high erosion rate of Herbert Sound despite the modern low temperatures of this area results in an unreasonable increase of <Er> for temperatures below ~ -3° C (Figure 4.8A). The indication that JRI ice cap and possibly the KGI ice cap were wet-based temperate ice bodies in the past, suggest that the use of long-term temperatures could improve the <Er> vs temperature correlation. Unfortunately, data on Holocene temperatures is not currently available.

A low degree of correlation was found between <Er> and mean annual precipitation (R^2<0.35; Figure 4.8B), although a trend of increasing <Er> with precipitation is apparent. However, this has to be viewed with caution given the poor constraints on the amounts of precipitation within the accumulation areas of glaciers. Particularly in Patagonia, direct measurements are sparse or nonexistent for most of the study areas, and data used here for discussion relies only on re-analysis modeling (DGF-CONAMA Professional Report, 2006; section 2). Key to understanding if precipitation has a correlation with <Er> is the relative amount of precipitation between San Rafael and Europa glaciers, because they are end members and have a high impact on the correlation coefficient of Figure 4.8B.

No correlation between <Er> and drainage basin area was found (Figure 4.8C). This is in good agreement with other researchers (e.g. Burbank, 2002) who suggested that other factors such as the geological/geographical setting, climate, and relief should be

more important, and with the suggestion that evidence relating erosion rates and drainage basin area is poor (Fernandez et al., 2011a).

4.5.6 Implications for the million-year scale erosion of the Patagonian - Antarctic Peninsula Cordillera

In order to understand the effects of glacial erosion on the evolution of mountain ranges, erosion rates at different geological time scales need to be determined. In most studies, estimation of million year-timescale erosion rates rely on the interpretation of exhumation rates derived from thermochronology analysis (e.g. Spotila et al., 2004; Koppes et al., 2009). However, when comparing erosion rates at different timescales, it is desirable to use the same methodology to avoid artificial differences generated by the set of assumptions, tools and geological proxies used by the different methods (Delmas, 2009). Additionally, it is not evident whether timescale itself does or does not influence a specific method, since geological processes themselves could produce a timescale dependence of estimated erosion rates (Fernandez et al., 2011a). The calculation of million year timescale erosion rates through the estimation of the volume of sediments produced over time, requires the quantification of sediment accumulated beyond the cordilleran front. This is because during maximum glacial conditions sediments are purged from fjords and none of the bays and fjords we have studied contain sifnificant accumulations of pre-Holocene sediments (Powell, 1984; Anderson et al., 2002). The only region within our study area where such quantification has been attempted is on the central Antarctic Peninsula (64°-68° S), just south of our southernmost studied area.

There, Bart and Anderson (1995) mapped the main stratigraphic units and regional unconformities on the shelf. On the continental rise, Rebesco et al. (1997, 2002) mapped a series of sediment mounds located at the toe of the slope and interpreted them as drifts originated from gravity flows. Smith (2009) correlated the sediments from the continental shelf and rise, and estimated the volume and age of the uppermost units. Based on these studies we estimate that basin-time average erosion rates for the last 9.5 Ma are between 0.07 and 0.12 mm/yr (Figure 4.8) and that they did not vary within the interval 2.9-9.5 Ma. These values are similar to those obtained using Holocene accumulation rates for Andvord and Lapeyrere Bay, suggesting that erosion rates have not varied significantly in this region through time. This also suggests that sediment production in these fjords during the Holocene might be a good analog for longer timescales despite different amplitude and wave length of climate variations.

Thermochronology studies in Patagonia show that youngest Apatite (U-Th)/He and fission track ages increase southward south of ~45° S (Thompson et al., 2010). South of ~45.5 to 46.0 ° S, mean and maximum elevation of the Andes is well above the estimated LGM and modern regional snow line altitude respectively (Broecker, 1990). This is not the case for the northern and central Andes. This is interpreted as a southward reduction in long-term glacial erosion efficiency, implying that north of ~45° S glacial erosion has effectively limited mountain height ("glacial buzz saw"; e.g. Egholm, 2009), whereas south of ~45° S, long-term ice cover has acted as a protective blanket, hindering erosion and allowing mountain growth (e.g. Thompson et al., 2010). However, although there is a general trend of decreasing <Er> with latitude, Late Pleistocene-Holocene millennial scale erosion rates are relatively high in this region (Figures 4.5 and 4.9). This

suggest that rates of bedrock erosion and sediment production have varied significantly through time, with larger variations occurring at ~48 to 52 °S where the Patagonian icefields are located and maximum elevation rises well over the modern snow line altitude (Thompson et al., 2010). This further indicates that glacial erosion has been relatively ineffective at geological timescale despite the relatively high Holocene erosion rates. Hence, modern high values of erosion rates in central-south Patagonia are not representative, nor should they be used directly to understand long-term mountain denudation (Koppes et al., 2009, 2010).

The number of thermochronology studies on the Antarctic Peninsula are much fewer than in Patagonia. Recently, Guenthner et al. (2010) obtained a set of ages that present two distinctive patterns north and south of Anvers Island (~65°S). To the north of Anvers Island, apatite He ranges between 65 and 24 Ma (with one exception at 11 Ma) and decrease in age southward. To the south, ages range from 16 to 8 Ma and decrease northward (Guenthner et al., 2010). This complex pattern of thermochronology ages is interpreted to be the result of different thermal histories north and south of Anver Island. The older Antarctic Peninsula ages indicate that million-year scale exhumation rates are lower than in Patagonia. This suggests that long-term glacial erosion is even more inefficient on the Antarctic Peninsula than in southern Patagonia, meaning that glacial cover has protected the Antarctic mountains allowing them to grow more than if the they were located in a more temperate region.

4.6 Conclusions

Accumulation rates in bays and fjords along an extended latitudinal transect (46-65°S) vary over several orders of magnitude. Millennial scale accumulation rates for Patagonian and Antarctic Peninsula fjords are within the same order of magnitude (~10^0 mm/yr), regardless of their different climate setting and the thermal state of the glaciers supplying them with sediments. We interpret this as being due to a modulated expression of the so called "Sadler effect" (i.e. accumulation rates are timespan dependent; Sadler, 1999), that is to say that at millennial timescales the relative proportion of hiatuses vs accumulation periods in the sedimentary section results in similar (low) accumulation rates. Particularly, in the Antarctic systems, accumulation rates are ~10^0 mm/yr regardless of the time span of deposition (i.e. no "Saddler effect"). This indicates that the same accumulation dynamics (sedimentation versus non deposition or erosion) have dominated the Antarctic fjords and bays at millennial timescales during most of the Holocene. However, in Patagonia proximal basins are in general well isolated and have short timescale (decadal-centennial) sedimentary records and high accumulation rates, whereas medial (more distal) basins have millennial scale sedimentary records and low accumulation rates. This produces a noticeable "Saddler effect". We hypothesize that the "Saddler effect" in the accumulation rates from the Patagonian systems exists because Neoglacial advance and recent post Little Ice Age retreat has left well isolated proximal basins that effectively trap sediments. This, along with high sediment yields, produces high decadal accumulation rates. There is no such organization of basins in the Antarctic Peninsula fjords and bays and no such clear manifestation of Neoglacial advances or morphologies.

Erosion rate values span two orders of magnitude from 0.03 mm/yr for Lapeyrere Bay on Anver Island, Antarctica (~64.5°S), to 1.09 mm/yr for San Rafael Glacier in northern Patagonia (~46.5°S). Rates from the Antarctic Peninsula glaciers are in general lower than the temperate Patagonian glaciers.

The latitudinal decrease of millenial <Er> along the studied Patagonian and Antarctic transect (about 5% per latitude degree) is interpreted as result of decreasing annual temperature, although a reduction in annual precipitation is also suggested. However, local variability within each region might be influenced by differences in bedrock geology (e.g. Herbert Sound versus Lapeyrere and Andvord bays <Er>) and drainage basin morphology (hypsometry, number of glaciers and length of overall calving front, topography slope). Particularly, the interplay between the variations through time of the equilibrium line altitude and glaciers hypsometry, which influences mass balance and glacier dynamics, seems to have a strong effect on the erosion capability of glaciers (e.g. Europa versus San Rafael and Marinelli glaciers). No correlation between millennial <Er> and drainage basin area was found.

Erosion rates on the Antarctic Peninsula for the last 9.5 Myr are between 0.07 and 0.12 mm/yr and did not vary within the interval 2.9-9.5 Ma. These values are similar to those obtained for millennial scale (Holocene) erosion rates at Andvord and Lapeyrere bays, suggesting that long-term erosion rates have not varied significantly in this region through time. This also suggests that sediment production in these fjords during the Holocene might be a good analog for longer timescales, despite different amplitude and wave length of climate variations over different timescales.

The pattern of thermochronology ages, and 10^3 and 10^6 years timescale erosion rates indicates that long-term glacial erosion decreases significantly with latitude, implying that long-term glacial cover acts as a protective blanket, hindering erosion and allowing mountain growth as previously suggested by other researchers (Thompson et al., 2010).

4.7 Acknowledgments

This research was funded by the National Science Foundation, Office of Polar Programs grant number NSF/OPP 03-38137 to John Anderson and Julia Wellner. We thank the officers, crew, and scientist who sailed on the RV/IB Nathaniel B. Palmer during NBP05-05 in the Chilean Fjords, and NBP07-03 among other cruises in the Antarctic Peninsula. We also thank the staff of the Antarctic Marine Geology Facility for their support on describing and sampling Antarctic cores in several visits to the facility.

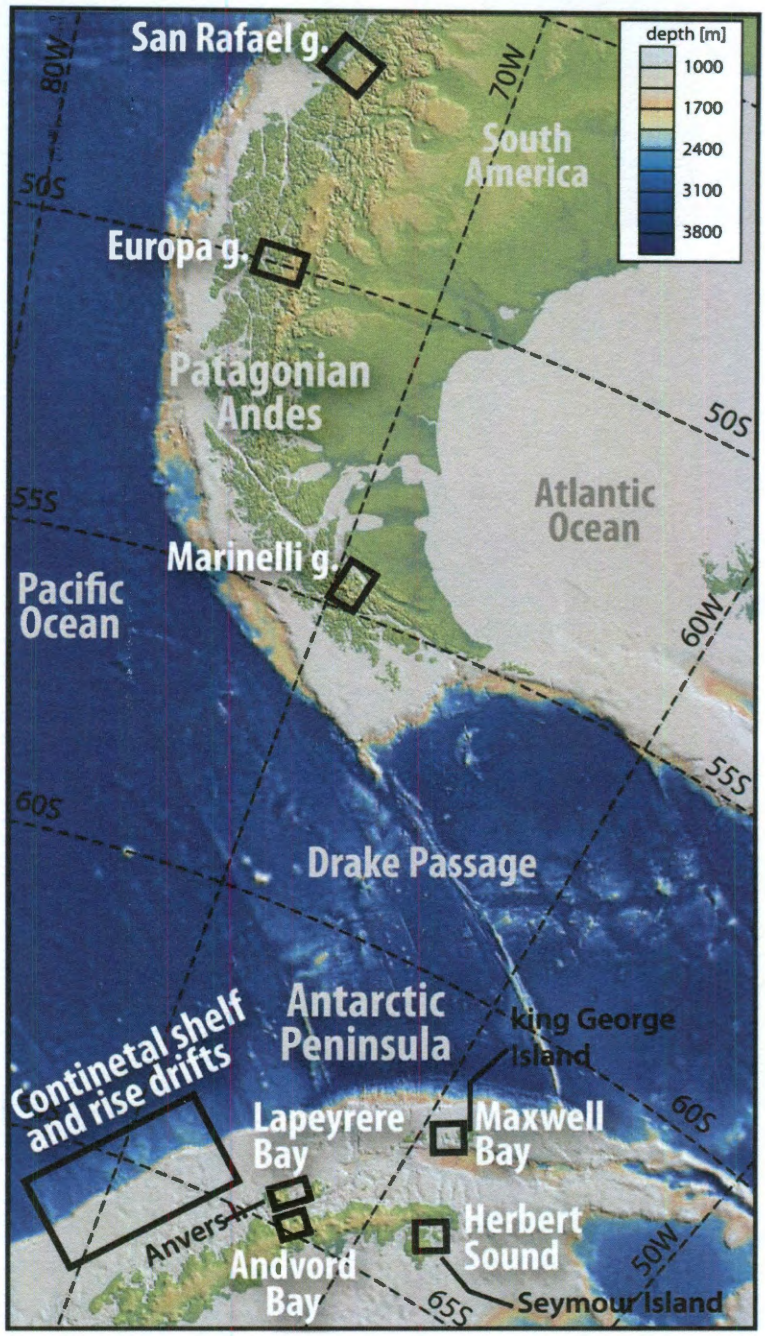

Figure 4.1 Map of southern South America and the Northern Antarctic Peninsula showing the areas of study. The data from the Antarctic Peninsula continental shelf and rise used in this study was modified from Smith (2009)

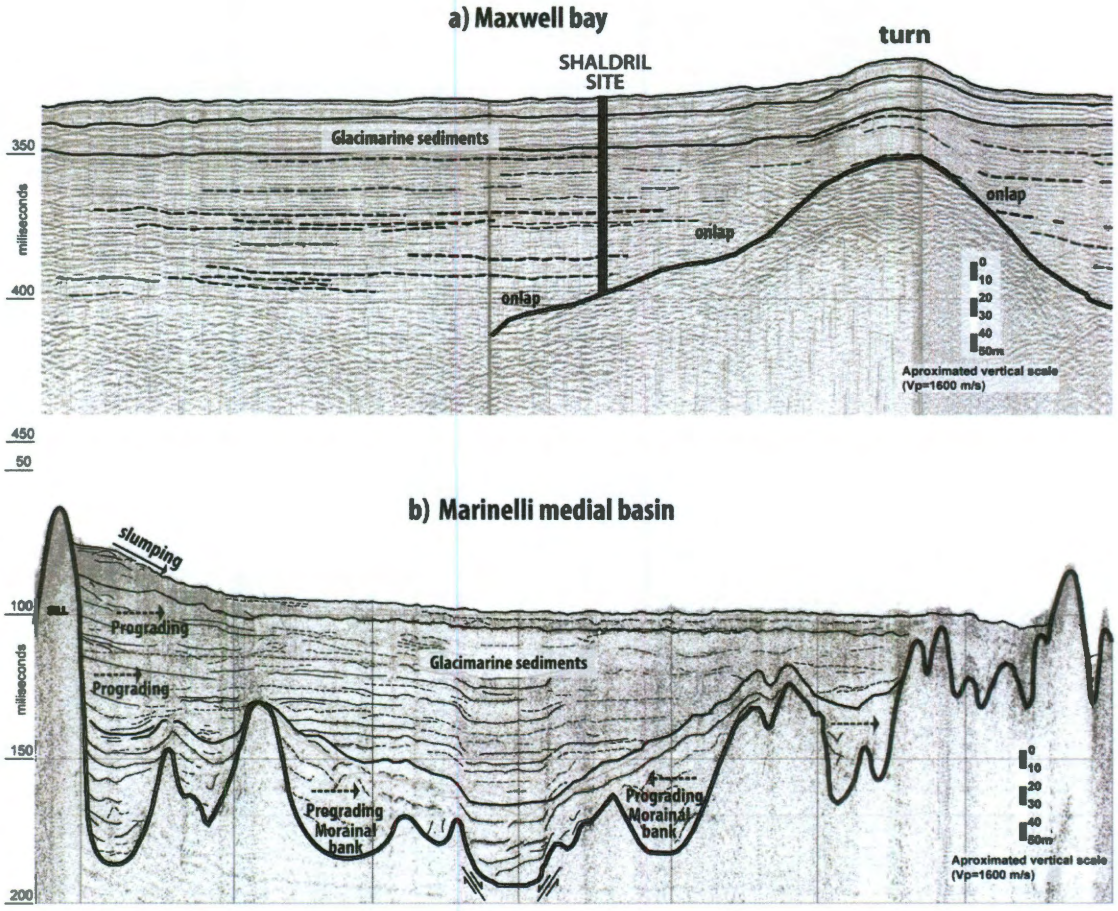

Figure 4.2 Seismic records for Maxwell bay (a) and Marinelli Glacier area (b) illustrating the main difference between sedimentary sections of Patagonian and Antarctic fjords/bays respectively. Both records were acquired using a single channel air gun system. In Maxwell Bay, the drill core obtained during cruise NBP0502 (SHALDRIL) is shown (Milliken et al., 2009)

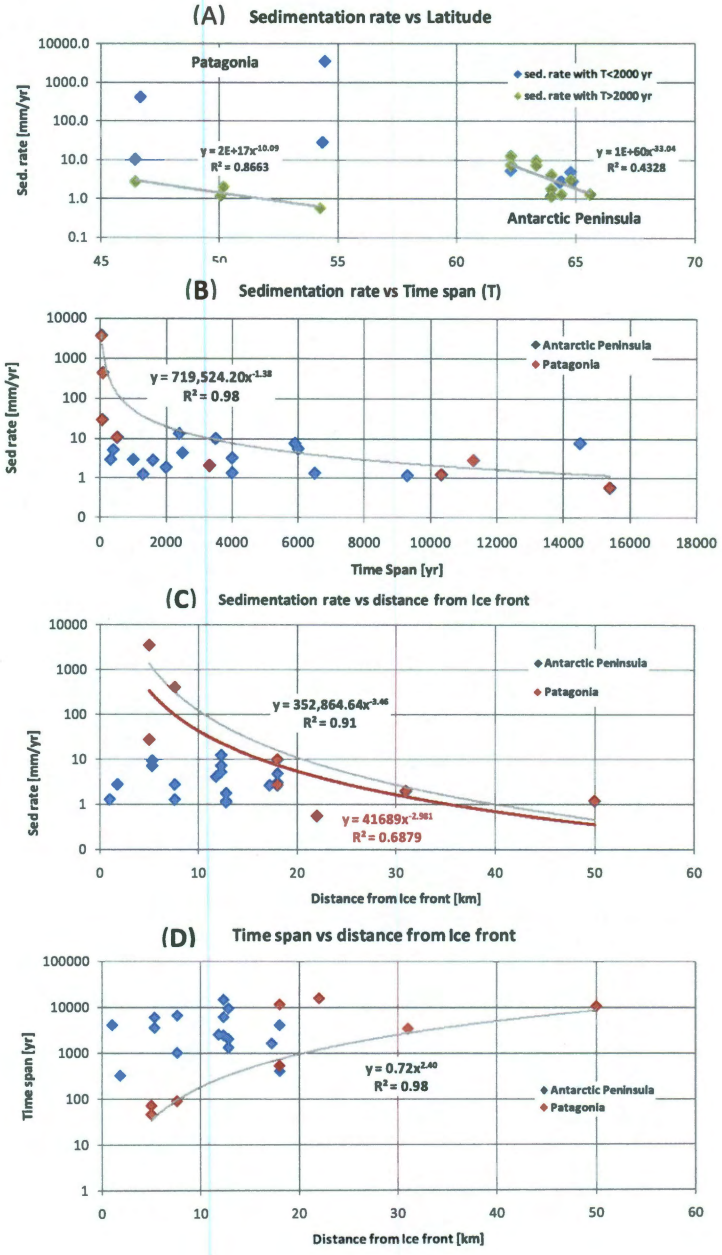

Figure 4.3 Sedimentation rates as function of (A) latitude, (B) time span, and (C) distance from present day ice front. (D) shows time span versus distance from present day ice front. Interpolations shown in dashed grey lines in B, C and D, correspond to the maximum (B, C) and minimum (D) values.

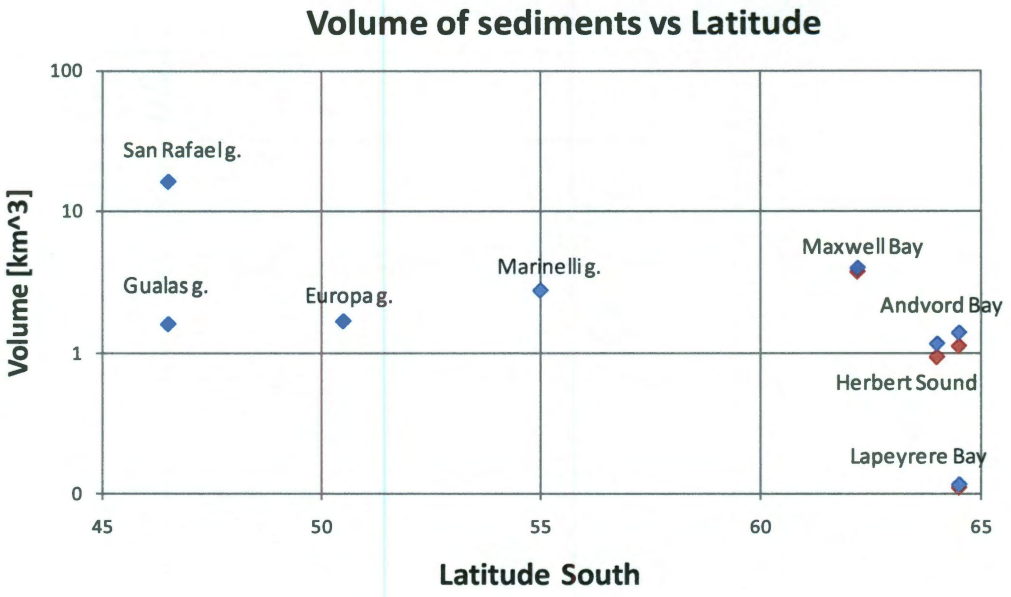

Figure 4.4 Volume of sediments accumulated in fjords and bays as a function of latitude.

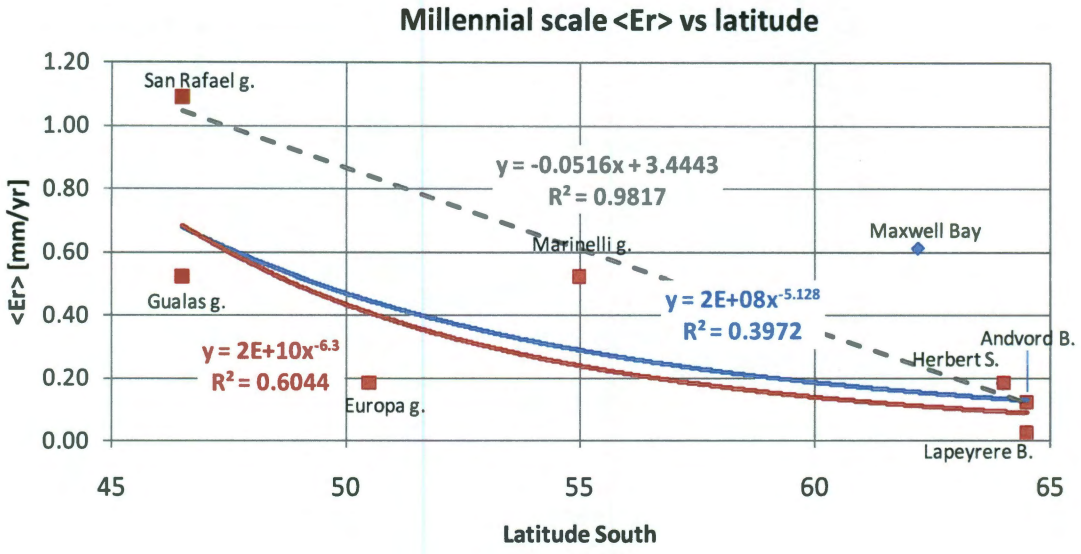

Figure 4.5 Time and basin wide average erosion rates (<Er>) versus latitude. The dashed blue line shows the best fit curve including all data points. The dashed red line shows the best fit curve including all data points but Maxwell Bay. The dashed gray line shows the best fit curve including only datapoints from well isolated bays, excluding Maxwell Bay. Also not included are Europa Glacier, Gualas Glacier and Lapeyrere Bay areas.

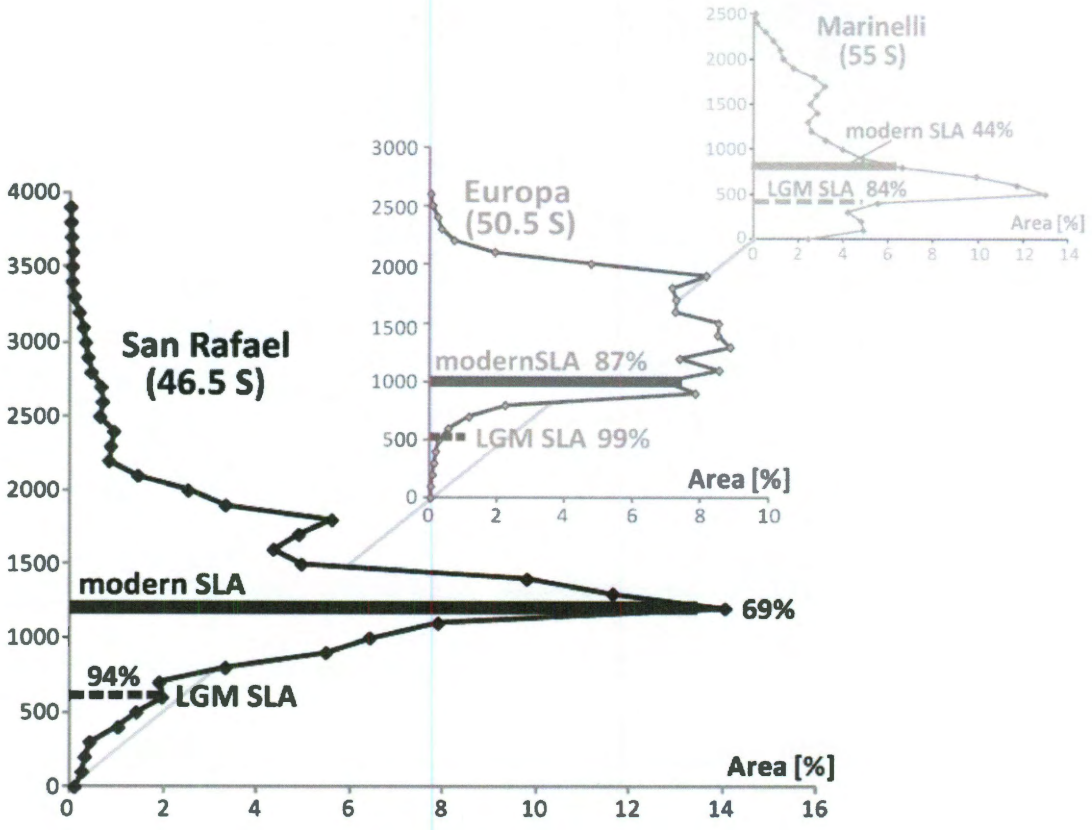

Figure 4.6 Hypsometry of the drainage basins of the Patagonian glaciers. Regional modern and last glacial maximum (LGM) snow line altitudes (SLA) from Broecker et al. (1990) and Thomson et al. (2010). Percentages refer to the accumulation area and thus can be directly related to the accumulation area ratio (AAR) of each glacier.

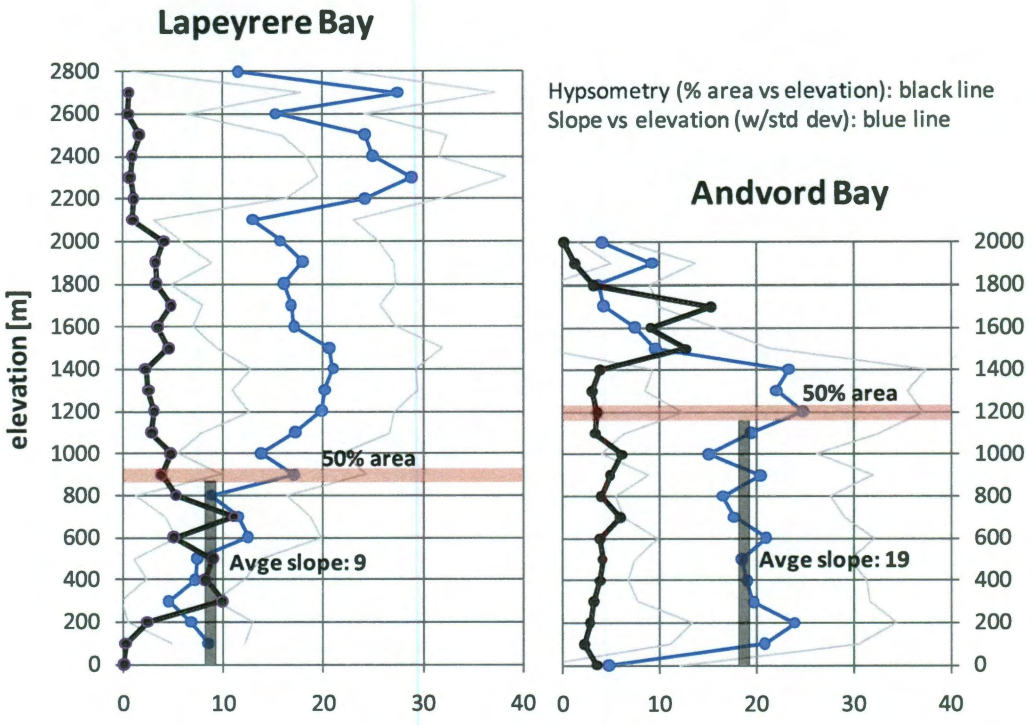

Figure 4.7 Hypsometry and slope vs elevation for the drainage area of Lapeyrere and Andvord bays.

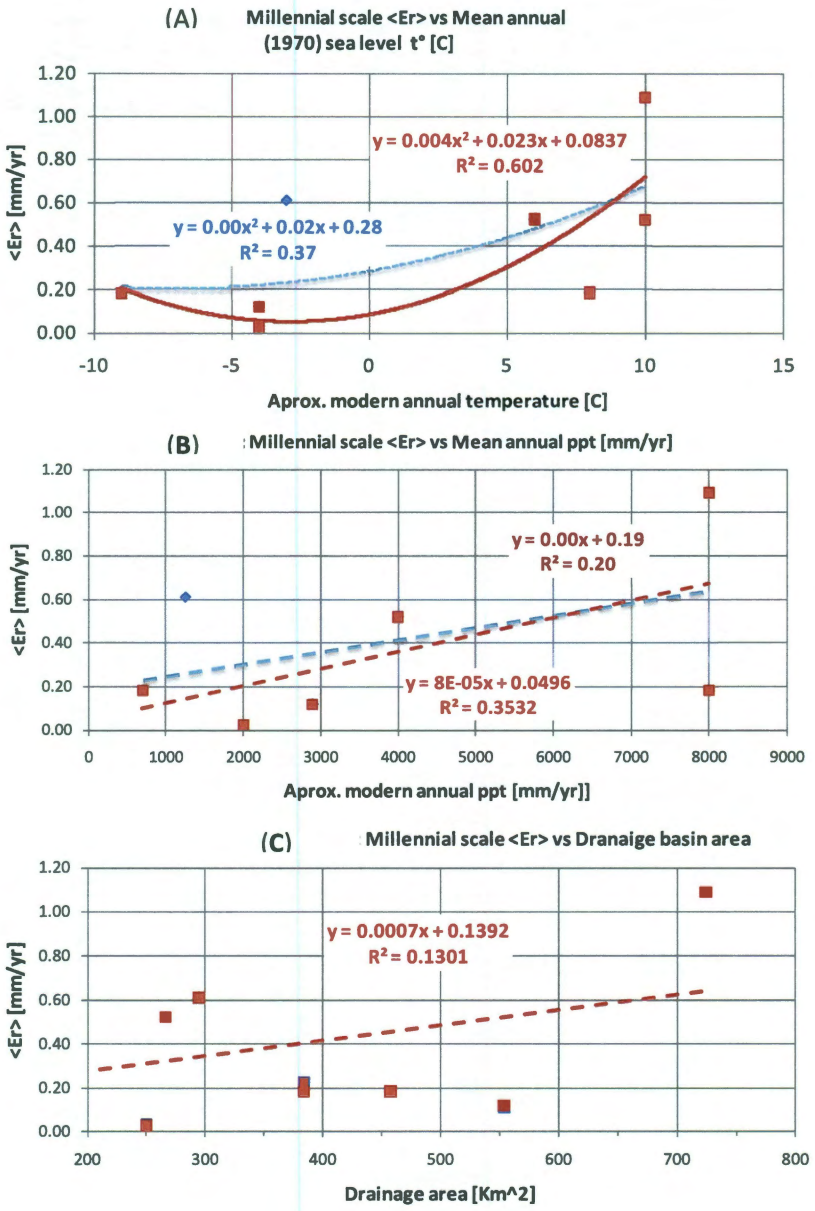

Figure 4.8 Millennial <Er> versus (A) mean annual temperature (1970); (B) mean annual precipitation; and (C) drainage basin area.

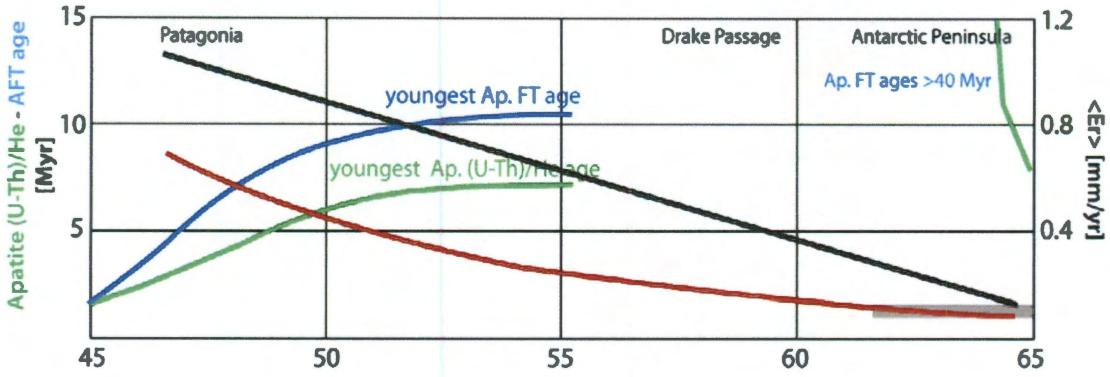

Figure 4.9 Comparison of trends of different datasets. In blue, the bounding line of the youngest apatite fission track (AFT) ages obtained by Thompson et al. (2010) in Patagonia. In green, the bounding line of the youngest apatite (U-Th)/He ages obtained by Thompson et al. (2010) in Patagonia. The same colors are used to represent the data obtained by Guenthner et al. (2010) in the Antarctic Peninsula. The red line represent the best fit of the <Er> data (without Maxwell Bay; dashed red line in Figure 4.4.) and the black line represent the best fit of the well isolated bays (dashed grey line in Figure 4.4). The thick grey line represents the million years timescale erosion rates obtained using data from Smith (2009).

References

Anderson, J. B., 1999. Antarctic Marine Geology. Cambridge University Press, pp 289.

Anderson, J.B., S.S. Shipp, A.L. Lowe, J.S. Wellner, and A.B. Mosola, 2002. The Antarctic ice sheet during the last glacial maximum and its subsequent retreat history: a review, Quaternary Science Reviews. 21, 49-70.

Andrews, J.T., J.D. Milliman, A. E. Jennings, N. Rynes and J. Dwyer, 1994. Sediments Thicknesses and Holocene Glacial Marine Sedimentation Rates in Three East Greenland Fjords, The Journal of Geology 102, 669-683.

Aniya, M.,1995. Holocene glacial chronology in Patagonia: Tyndall and Upsala Glaciers. Arctic and Alpine Research, 27, 4, 311-322.

Aniya, M. and Enomoto, H, 1986. Glacier variations and their causes in the Northern Patagonia Icefield, Chile, since 1944. Arctic and Alpine Research, 18, 3, 307-316.

Araneda, A., Torrejón, F., Aguayo, M., Torres, L., Cruces, F., Cisternas, M. and Urrutia, R., 2007. Historical records of San Rafael Glacier advances (North Patagonian Icefield): another clue to 'Little Ice Age' timing in southern Chile?. The Holocene, 17, 7, 987-998.

Ashley, G. M. and N. D. Smith, 2000. Marine sedimentation at a calving glacier margin, Geological Society of America Bulletin 112, 657-667.

Ashworth, A. C., Markgraf, V. and Villagran, C., 1991. Late Quaternary climatic history of the Chilean channels based on fossil pollen and beetle analyses, with an analysis of the modern vegetation and pollen rain. Journal of Quaternary Science, 6, 279-291, lSSN 0267-81 79.

Bart, P.J., Anderson, J.B., 1996. Seismic expression of depositional sequences associated with expansion and contraction of ice sheets on the Northwestern Antarctic Peninsula Continental Shelf. Geological Society Special Publication, 117, 171–186.

Bennett, K. D., Haberle, S. G. and Lumley, S. H., 2000. The Last Glacial-Holocene transition in southern Chile. Science, 290, 325-328, DOI: 10.1126/science.290.5490.325.

Bibby, J.S., 1966. The stratigraphy of part of north-eastGrahamLand and the James Ross Island group. British Antarctic Survey Scientific Reports 53, 37 p..

Blindow, N., Suckro, S. K., Ruckamp, M., Braun, M., Schindler, M., Breuer, B., Saurer, H., Simones, J. C., Lange, M. A., 2010. Geometry and thermal regime of the King

George Island ice cap, Antarctica, from GPR and GPS. Annals of Glaciology 51, 55, 103-109.

Blisniuk, P. M., L. A. Stern, C. P. Chamberlain, P. K. Zeitler, V. A. Ramos, E. R. Sobel, M. Haschke, R. Manfred, M. R. Strecker and F. Warkus, 2006. Links between Mountain Uplift, Climate, and Surface Processes in the Southern Patagonian Andes, In The Andes. Springer Berlin Heidelberg, doi 10.1007/978-3-540-48684-8, 429-440.

Boyd, B.L., J.B. Anderson, J.S. Wellner and R.A. Fernandez, 2008. The sedimentary record of glacial retreat, Marinelli Fjord, Patagonia: Regional correlations and climate ties. Marine Geology 255, 165-178.

Broecker, W. S. & Denton, G. H. The role of ocean-atmosphere reorganizations in glacial cycles. Quat. Sci. Rev. 9, 305–341, 1990.

Burbank, D. W., 2002. Rates of erosion and their implications for exhumation, Mineralogical Magazine 66, 1, 25-52.

Cai, J., 1994. Sediment yields, lithofacies architecture and mudrock characteristics in glacimarine environments, PhD dissertation, 442 pp., Northern Illinois University.

Caldenius, C., 1932. Las Glaciaciones Cuaternarias en la Patagonia y Tierra del Fuego, Geografiska Annaler 14, 1-164.

Carlson, P.R., 1989. Seismic reflection characteristics of glacial and glacimarine sediment in the Gulf of Alaska and adjacent fjords, in Modern Glacimarine Environments: Glacial and Marine Controls on Modern Lithofacies and Biofacies, Marine Geology 85, 391-416.

Clapperton, C. M., and Sugden D. E., 1988. Holocene Glacier Fluctuations in South America and Antarctica, Quaternary Science Reviews 7, 185-198.

Clapperton, C., 2000. Interhemispheric synchroneity of Marine Oxygen Isotope Stage 2 glacier fluctuations along the American cordilleras transect, Journal of Quaternary Science 15, 4, 435-468.

Clapperton, C.M., 1995. The Last Glaciation in Central Magellan Strait, Southernmost Chile, Quaternary Research 44, 133-148.

Cunningham, W. D.,1995. Orogenesis at the southern tip of the Americas: the structural evolution of the Cordillera Darwin metamorphic complex, southernmost Chile, Tectonophysics 244, 197-229.

DaSilva, J. L., Anderson, J. B. and Stravers, J., 1997. Seismic facies changes along a nearly continuous 24° latitudinal transect: the fjords of Chile and the northern Antarctic Peninsula. Marine Geology, 143, 103-123.

Delmas M., M. Calvet, and Y. Gunnell, 2009. Variability of Quaternary glacial erosion rates – A global perspective with special reference to the Eastern Pyrenees, Quaternary Science Reviews 28, 484-498.

DGF, Departamento de Geofísica, Facultad de Ciencias Físicas y Matemáticas, Universidad de Chile-CONAMA, Comisión Nacional del Medio Ambiente, Chile, 2006. Estudio de la variabilidad climática en Chile para el siglo XXI. http://www.conama.cl/portal/1301/articles-39442_pdf_Estudio_texto.pdf

Domack, E. W., D.J.P. Foss, J.P.M. Syvitski, and C.E. McClennen, 1994. Transport of suspended particulate matter in an Antarctic fjord, Marine Geology 121, 161-170.

Domack, E.W., Amblàs, D., Gilbert, R., Brachfeld, S., Camerlenghi, A., Rebesco, M., Canals, M. and Urgeles, R., 2006. Subglacial morphology and glacial evolution of the Palmer deep outlet system, Antarctic Peninsula. Geomorphology, 75, 1-2, 125-142, ISSN 0169-555X, doi: 10.1016/j.geomorph.2004.06.013.

Domack, E.W., and Ishman, S.,1993. Oceanographic and physiographic controls on modern sedimentation within Antarctic fjords, GSA Bulletin, v. 105, p. 1175-1189.

Domack, E.W., Burnett, A, Leventer, A., 2003. Environmental Setting of the Antarctic Peninsula. In E. W. Domack, A. Leventer, A. Burnett, R. Bindschadler, P. Convey and M. Kirby, Eds., Antarctic Peninsula climate variability; historical and paleoenvironmental perspectives. Antarct. Res. Ser. 79. American Geophysical Union, Washington D.C., 1-13.

Domack, E.W., Leventer, A., Dunbar, R., Taylor, F., Brachfeld, S., Sjunneskog, C., and ODP Leg 178 Scientific Party, 2001. Chronology of the Palmer Deep site, Antarctic Peninsula: a Holocene paleoenvironmental reference for the circum-Antarctic. The Holocene 11, 1-9.

Douglass, D. C., Singer, B.S., Kaplan, M.R., Ackert, R.P, Mickelson, D.M. and Caffee, M.W., 2005. Evidence of early Holocene glacial advances in southern South America from cosmogenic surface-exposure dating. Geology, 33, 237-240, doi: 10.1130/G21144.1.

Egholm, D. L., Nielsen, S. B., Pedersen, V. K. and Leseman, J. E, 2009. Glacial effects limiting mountain height. Nature, 460, 884–888.

Elverhøi, A., Hooke, R. L. and Solheim, A., 1998. Late Cenozoic erosion and sediment yield from the Svalbard-Barents sea region: Implications for understanding erosion of glacierized basins. Quaternary Science Reviews, 17, 209-241.

Elverhøi, A., J. I. Svendsen, A. Solheim, E. S. Andersen, J. Milliman, J. Mangerud, and R. L. Hooke, 1995. Late Quaternary Sediment Yield from the High Arctic Svalbard Area, The Journal of Geology 103, 1, 1-17.

EPICA Community Members, 2004. Eight glacial cycles from an Antarctic ice core. Nature 429, 623–628.

Fernandez, R.A., Anderson, J.B., Bertrand, S., and Wellner, J.S., 2011b. The Holocene sedimentary record of climate change from Gualas Glacier, Golfo Elefantes, Northern Patagonia (46.5°S), The Holocene, in press.

Fernandez, R.A., Anderson, J.B., Wellner, J.S., and Hallet, B., 2011a. Timescale dependence of erosion rates, a case study: Marinelli Glacier, Cordillera Darwin, southern Patagonia. Journal of Geophysical Research-Earth Surface, 116, doi:10.1029/2010JF001685.

GEBCO, General Bathymetric Chart of the Oceans, 2003. One arc-minute grid data. https://www.bodc.ac.uk/data/online_delivery/gebco/

Geirsdóttir, A., G. H. Miller, and J. T. Andrews, 2007. Glaciation, erosion and landscape evolution of Iceland, Journal of Geodynamics 43, 170-186.

Gilbert, R., A.E. Aitken, and D.S. Lemmen, 1993. The glacimarine sedimentary environment of Expedition Fiord, Canadian High Arctic, Marine Geology 110, 257-273.

Glasser, N. F., and A. M. Hall, 1997. Calculating Quaternary glacial erosion rates in northeast Scotland, Geomorphology 20, 29-48.

Glasser, N. F., Jansson, K. N., Harrison, S. and Rivera, A., 2005. Geomorphological evidence for variations of the North Patagonian Icefield during the Holocene. Geomorphology, 71, 263-277.

Glasser, N. F., K. N. Jansson, S. Harrison, and J. Kleman, 2008. The glacial geomorphology and Pleistocene history of South America between 38°S and 56°S, Quaternary Science Reviews 27, 365-390.

Glasser, N. F., Krister, J., Wishart, A. M. and Harrison, S., 2006. The geomorphology and sedimentology of the 'Témpanos' moraine at Laguna San Rafael, Chile. Journal of Quaternary Science, 21, 6, 629-643. ISSN 0267–8179.

Gombosi, D. J., D. L. Barbeau Jr., and J. I. Garver, 2009. New thermochronometric constraints on the rapid Palaeogene exhumation of the Cordillera Darwin complex and related thrust sheets in the Fuegian Andes, Terra Nova 21, 507-515.

Griffith, T. W., and Anderson, J.B., 1989. Climatic Control of sedimentation in bays and fjords of the northern Antarctic Peninsula. Marine Geology, 85, 181-204.

Guenthner, W. R., Barbeau Jr., D. L., Reiners, P. W. and Thomson, S. N., 2010. Slab window migration and terrane accretion preserved by low temperature thermochronology of a magmatic arc, northern Antarctic Peninsula. Geochemistry, Geophysics and Geosystems, 11, 3, Q03001, doi:10.1029/2009GC002765.

Hallet, B., L. Hunter, and J. Bogen, 1996. Rates of erosion and sediment evacuation by glaciers; a review of field data and their implications. Global and Planetary Change, 12, 1-4, 213-235.

Hambrey, M.J., Smellie, J.L., 2006. Distribution, lithofacies and environmental context of Neogene glacial sequences on James Ross and Vega islands, Antarctic Peninsula. In: Francis, J.E., Pirrie, D., Crame, J.A., Eds., Cretaceous–Tertiary High-latitude Palaeoenvironments, James Ross Basin, Antarctica. Geological Society, London, Special Publication, 258, 187–200.

Hambrey,M.J., Smellie, J.L., Nelson, A.E. and Johnson, J.S., 2008. Late Cenozoic glacier–volcano interaction on James Ross Island and adjacent areas, James Ross Island. Geological Society of America Bulletin, 120, 709–731.

Hamilton, E. L., and Bachman R.T., 1982. Sound velocity and related properties of marine sediments. Journal of the Acoustical Society of America, 72, 6, 1891-1904.

Hamilton, E.L.,1971. Elastic Properties of Marine Sediments, Journal of Geophysical Research 76, 2, 579-604.

Harbor, J., and J. Warburton, 1993. Relative Rates of Glacial and Nonglacial Erosion in Alpine Environments, Arctic and Alpine Research 25, 1, 1-7.

Harbor, J.M., 1992. Numerical modelling of the development of U-shaped valleys by glacial erosion, GSA Bulletin 104, 1364-1375.

Harbor, J.M., 1993. Glacial geomorphology: modeling processes and landforms, Geomorphology 7, 129-140.

Harrison, S. and Winchester, V.,1998. Historical fluctuations of the Gualas and Reicher glaciers, North Patagonian Icefield, Chile. The Holocene, 8, 4, 481-485, doi: 10.1191/095968398672334459.

Harrison, S., Winchester, V. and Glasser, N., 2007. The timing and nature of recession of outlet glaciers of Hielo Patagónico Norte, Chile, from their Neoglacial IV (Little Ice Age) maximum positions. Global and Planetary Change, 59, 67-78.

Hay, W. W., Sloan, J. L. I. and Wold, C. N., 1988. The mass/age distribution of sediments on the ocean floor and the global rate of loss of sediment. Journal of Geophysical Research, 93, 14933–14940.

Herve, F., A. Demant, V.A. Ramos, R.J. Pankhurst, and M. Suarez, 2000. The Southern Andes, Tectonic Evolution of South America, 605-634.

Herve, F., C.M. Fanning, and R.J. Pankhurst, 2003. Detrital zircon age patterns and provenance of the metamorphic complexes of southern Chile, Journal of South American Earth Sciences 16, 107-123.

Herve, F., E. Nelson, K. Kawashita, and M. Suarez, 1981. New isotopic ages and the timing of orogenic events in the Cordillera Darwin, southernmost Chilean Andes, Earth and Planetary Science Letters 55, 257-265.

Herve, F., R.J. Pankhurst, C.M. Fanning, M. Calderon, and G.M. Yaxley, 2007. The South Patagonian batholith: 150 my of granite magmatism on a plate margin, Lithos 97, 373-394.

Heusser, C. J., 1960. Late-Pleistocene environments of the Laguna de San Rafael area, Chile. Geographical Review, 50, 4, 555-577.

Heusser, C. J., 2002. On glaciation of the Southern Andes with special reference to the Península de Taitao and adjacent Andean cordillera (~46°30'S). Journal of South American Earth Sciences, 15, 577–589.

Holmlund, P., and H. Fuenzalida, 1995. Anomalous glacier responses to 20th century climatic changes in the Darwin Cordillera, southern Chile, Journal of Glaciology 41, 209–220.

Hubbard, A., Hein, A. S., Kaplan, M. R., Hulton, N. R. J. and Glasser, N., 2005. A modeling reconstruction of the last glacial maximum ice sheet and its deglaciation in the vicinity of the northern Patagonian Icefield, South America. Geografiska Annaler, 87A, 2, 375-391.

Hulton, N.R.J., Purves, R.S., McCulloch, R.D., Sugden, D.E. and Bentley, M.J., 2002. The Last Glacial Maximum and deglaciation in southern South America. Quaternary Science Reviews, 21, 233-341.

Jordan, G.F., 1962. Redistribution of sediments in Alaskan bays and inlets, Geographical Review 52, 548-558.

Kaplan, M. R., Ackert Jr., R. P., Singer, B. S., Douglass, D. C. and Kurz, M. D.,2004. Cosmogenic nuclide chronology of millennial-scale glacial advances during O-Isotope Stage 2 in Patagonia. GSA Bulletin, 116, 3, 308–321, doi: 10.1130/B25178.1.

Kaplan, M. R., Fogwill, C. J., Sudgen, D. E., Hulton, N. R. J., Kubik, P. W. and Freeman, S. P. H. T., 2008. Southern Patagonian glacial chronology for the Last Glacial period and implications for Southern Ocean climate. Quaternary Science Reviews, 27, 284–294.

Kaplan, M.R., P.I. Moreno, M. Rojas, 2008. Glacial dynamics in southernmost South America during Marine Isotope Stage 5e to the Younger Dryas chron: a brief review with a focus on cosmogenic nuclide measurements, Journal of Quaternary Science 23, 6-7, 649-658.

Kilian, R., C. Schneider, Koch, J., M. Fesq-Martin, H. Biester, G. Casassa, M. Arevalo, G. Wendt, O. Baeza, and J. Behrmann, 2007. Palaeoecologiacal constraints on late Glacial and Holocene ice retreat in the Southern Andes (53°), Global and Planetary Change 59, 49-66.

Knap, W. H., Oerlemans, J. and Cadee, M., 1996. Climate sensitivity of the ice cap of King George Island, South Shetland Islands, Antarctica. Annals of Glaciology, 23, 154-159

Koch, J. and Kilian, R., 2005. 'Little Ice Age' glacier fluctuations, Gran Campo Nevado, southernmost Chile. The Holocene, 15, 20-28, doi: 10.1191/0959683605hl780rp.

Koppes, M,. and Montgomery D., 2009a. The relative efficacy of fluvial and glacial erosion over modern to orogenic timescales. Nature Geoscience, 2, 644-647.

Koppes, M. and Hallet, B., 2002. Influence of rapid glacial retreat on the rate of erosion by tidewater glaciers. Geology, 30, 1, 47-50.

Koppes, M. and Hallet, B., 2006. Erosion rates during deglaciation in Icy Bay, Alaska. Journal of Geophysical Research, 111, F02023, doi:10.1029/2005JF000349.

Koppes, M., Hallet, B. and Anderson, J., 2009b. Synchronous acceleration of ice loss and glacial erosion, Glaciar Marinelli, Chilean Tierra del Fuego. Journal of Glaciology, 55, 190, 207-220.

Koppes, M., Sylwester, R., Rivera, A., Hallet, B., 2010. Variations in sediment yield over the advance and retreat of a calving glacier, Laguna San Rafael, North Patagonian Icefield. Quaternary Research, 73, 1, 84-95, ISSN 0033-5894, doi: 10.1016/j.yqres.2009.07.006.

Kuylenstierna, J.L., G.C. Rosqvist and P. Holmlund, 1996. Late-Holocene glacier variations in the Cordillera Darwin, Tierra del Fuego, Chile, The Holocene 6, 3, 353-358.

Laberg, J. S., R.S. Eilertsen, and T.O. Vorren 2009, The paleo–ice stream in Vestfjorden, north Norway, over the last 35 k.y.: Glacial erosion and sediment yield, GSA Bulletin 121, 3, 434-447.

Lamy, F., Hebbeln, D., Röhl, U. and Wefer, G., 2001. Holocene rainfall variability in southern Chile: a marine record of latitudinal shifts of the Southern Westerlies. Earth and Planetary Science Letters, 185, 369-382.

Lamy, F., Kilian, R., Helge Arz, H.W., Francois, J.P., Kaiser, J., Prange, M. and Steinke, T., 2010. Holocene changes in the position and intensity of the southern westerly wind belt. Nature Geoscience, 3, 695-699.

Lopez, P., Chevallier, P., Favier, V. and Pouyaud, B., 2010. A regional view of fluctuations in glacier length in southern South America. Global and Planetary Change, 71, 85-108.

Lumley, S. H. and Switsur, R., 1993. Late Quaternary chronology of the Taitao Peninsula, southern Chile. Journal of Quaternary Science, 8, 161-165, ISSN 0267-8179.

Mammone, 1992. Modern particle flux and productivity in Andvord Bay, Antarctica. BA thesis, 98 pp., Hamilton College, Clinton, New York.

Markgraf, V., 1993. Paleoenvironments and paleoclimates in Tierra del Fuego and southernmost Patagonia, South America. Palaeogeography, Palaeoclimatology, Palaeoecology, 102, 53-68.

Mashiotta, T.A., 1992. Biogenic sedimentation in Andvord Bay, Antarctica: a 3000 year record of paleoproductivity. BA thesis, 86 pp., Hamilton College, Clinton, New York.

McCulloch, R.D., Bentley, M.J., Purves, R.S., Hulton, N.R.J., Sugden, D.E. and Clapperton C.M., 2000. Climatic inferences from glacial and palaeoecological evidence at the last glacial termination, southern South America. Journal of Quaternary Science, 15, 4, 409–417.

McCulloch, R.D., Fogwill, C.J., Sugden, D.E., Bentley, M.J., and Kubik, P.W., 2005a. Chronology of the last glaciation in central Strait of Magellan and Bahia Inútil, southernmost South America. Geografiska Annaler, 87A, 2, 289-312.

McCulloch, R.D., M.J. Bentley, R.M. Tipping, and C.M. Clapperton, 2005b. Evidence for lateglacial ice dammed lakes in the central Strait of Magellan and Bahía Inútil, southernmost South America, Geografiska Annaler 87A, 2, 335–362.

Mercer, J. H., 1965. Glacier variations in southern Patagonia. Geographical Review, 55, 3, 390-413.

Mercer, J. H., 1968. Variations of some Patagonian glaciers since the Late-Glacial. American Journal of Science, 266, 91-109.

Mercer, J.H., 1970. Variations of some Patagonian Glaciers since the Late-Glacial: II, American Journal of Science 269, 1-25.

Mercer, J.H., 1976. Glacial history of Southernmost South America, Quaternary Research 6, 125-166.

Michalchuk, B.R, Anderson J.B., Wellner, J.S., Manley, P.L., Majewski, W. and Bohaty, S., 2009. Holocene climate and glacial history of the northeastern Antarctic Peninsula: the marine sedimentary record from a long SHALDRIL core. Quaternary Science Reviews, 28, 3049-3065.

Michalchuk, B.R., 2006. Synthetic Seismograms and Physical Properties generated from Sediments in Maxwell Bay, Antarctica – A Study of Climate History, B. A. thesis, Department of Geology, Middlebury College, Middlebury, Vermont, U.S..

Milliken, K.T., Anderson, J.B., Wellner, J.S., Bohaty, S., and Manley, P., 2009. High-resolution Holocene climate record from Maxwell Bay, South Shetland Islands, Antarctica. Geological Society of America Bulletin, 121, 11/12, 1711-1725, doi: 10.1130/B26478.1.

Milliman, J. D. and Syvitski, J. P. M., 1992. Geomorphic/tectonic control of sediment discharge to the ocean: the importance of small mountainous rivers. Journal of Geology, 100, 525–544.

Mitchell, S. G., and D.R. Montgomery, 2006. Influence of a glacial buzzsaw on the height and morphology of the Cascade Range in Central Washington State, USA, Quaternary Research 65, 96-107.

Molnar, P., 2004. Late Cenozoic increase in accumulation rates of terrestrial sediment: How might climate change have affected erosion rates?. Annual Review of Earth and Planetary Sciences, 32, 67 -89.

Molnar, P., and P. England, 1990. Late Cenozoic uplift of mountain ranges and global climate change: chicken or egg?. Nature 346, 29-34.

Molnia, B.F., 1985. Processes on a glacier-dominated coast, Alaska, Geomorphology 57, 141-153.

Montgomery, D., G. Balco, and Willet, S.D., 2001. Climate, tectonics and the morphology of the Andes. Geology, 29, 7, 579-582.

Moreno, P.I., Francois, J.P., Moy, C.M. and Villa Martinez, R., 2010. Covariability of the southern Westerlies and atmospheric CO2 during the Holocene. Geology, 38, 727-730, doi: 10.1130/G30962.1.

Moreno, P.I., Jacobson Jr., G.L., Lowell, T.V. and Denton, G.H., 2001. Interhemispheric climate links revealed by a late-glacial cooling episode in Southern Chile. Nature, 409, 804-808.

Morris, E.M., and Vaughan, D.G., 2003. Spatial and temporal variation of surface temperature on the Antarctic Peninsula and the limit of viability of ice shelves. Antarctic Peninsula Climate Variability, AGU Antarctic Research Series, 79, 61-68.

Mulder, T. and Syvitski, J. P. M., 1995. Turbidity currents generated at river mouths during exceptional discharges to the world oceans. The Journal of Geology, 103, 3, 285-299.

Mulder, T., Syvitski, J. P. M., Migeon, S., Faugeres, J. C. and Savoye, B., 2003. Marine hyperpycnal flows: initiation, behavior and related deposits. A review. Marine and Petroleum Geology, 20, 861–882.

Muller, E.H., 1959. Glacial geology of the Laguna de San Rafael area, southern Chile. Bulletin of the Geological Society of America, 70, 1649.

Nelson, E. P., 1982. Post-tectonic uplift of the Cordillera Darwin orogenic core complex: evidence from fission track geochronology and closing temperature-time relationships, Journal of the Geological Society 139, 755-761, doi:10.1144/gsjgs.139.6.0755.

Nelson, P.H.H., 1975. The James Ross IslandVolcanic Group of north-east Graham Land. British Antarctic Survey Scientific Reports, 54, 1–62.

Nick, F.M., C.J. Van Der Veen, and J. Oerlemans, 2007. Controls on advance of tidewater glaciers: Results from numerical modeling applied to Columbia Glacier, Journal of Geophysical Research 112, F03S24, doi:10.1029/2006JF000551,

Orsi, T.H., and D.A. Dunn, 1991. Correlations between Sound Velocity and Related Properties of Glacio-Marine Sediments: Barents Sea, Geo-Marine Letters 11, 79-83.

Peizhen, Z., Molnar, P. and Downs, W. R., 2001. Increased sedimentation rates and grain sizes 2–4 Myr ago due to the influence of climate change on erosion rates. Nature, 410, 891-897, doi: 10.1038/35073504.

Pfeffer, W.T., 2007. A simple mechanism for irreversible tidewater glacier retreat, Journal of Geophysical Research 112, F03S25, doi:10.1029/2006JF000590,

Porter, C. and A. Santana, 2003. Rapid 20th century retreat of Ventisquero Marinelli in the Cordillera Darwin Icefield, Anales Instituto de la Patagonia 31, 17-26.

Powell, R.D., 1984. Glacimarine processes and inductive lithofacies modelling of ice shelf and tidewater glacier sediments based on Quaternary examples, Marine Geology 57, 1-52.

Powell, R.D.,1991. Grounding-line systems as second-order controis on fluctuations of tidewater termini of temperate glaciers. Glacial Marine Sedimentation; Paleoclimatic Significance, In: J.B. Anderson and G.M. Ashley, Eds., Geological Society of America Special Paper 261, 75-93.

Powell, R.D., and B.F. Molnia, 1989. Glacimarine sedimentary processes, facies and morphology of the south-southeast Alaska shelf and fjords, Modern Glacimarine Environments: Glacial and Marine Controls of Modern Lithofacies and Biofacies, R.D. Powell and A. Elverhųi, Eds., Marine Geology 85, 359-390.

Rabassa, J., A. Coronato, G. Bujalesky, M. Salemme, C. Roig, A. Meglioli, C. Heusser, S. Gordillo, F. Roig, A. Borromei, and M. Quattrocchio, 2000. Quaternary of Tierra del Fuego, southernmost South America: and updated review. Quaternary International 68-71, 217-240.

Rebesco, M., Camerlenghi, A., Geletti, R. and Canals, M., 2006. Margin architecture reveals the transition to the modern Antarctic Ice Sheet (AIS) at about 3 Ma. Geology, 34, 4, 301–304.

Rebesco, M., Larter, R.D., Barker, P.F., Camerlenghi, A. and Vanneste, L.E., 1997. The history of sedimentation on the continental rise west of the Antarctic Peninsula. In: Cooper, A.K., Barker, P.F., Eds., Geology and Seismic Stratigraphy of the Antarctic Margin 2. AGU Antarctic Research Series, 71, 28–49.

Reynolds, J. M., 1981. The distribution of mean annual temperatures in the Antarctic Peninsula. British Antarctic Survey Bulletin, 54, 123-133.

Rignot, E., Rivera, A. and Casassa, G., 2003. Contribution of the Patagonia Icefields of South America to Sea Level Rise. Science, 302, 5644, 434-437, doi: 10.1126/science.1087393.

Rivera, A., Benham, T., Casassa, G., Bamber, J. and Dowdeswell, J. A., 2007. Ice elevation and areal changes of glaciers from the Northern Patagonia Icefield, Chile. Global and Planetary Change, 59, 126–137.

Röthlisberger, F., 1986. 10 000 Jahre Gletschergeschichte der Erde. Verlag Sauerländer.

Ruckamp, M., Blindow, N., Suckro, S., Braun, M. and Humbert, A., 2010. Dynamics of the ice cap on King George Island, Antarctica: field measurements and numerical simulations. Annals of Glaciology, 51, 55, 80-90.

Sadler, P. M., 1999. The influence of hiatuses on sediment accumulation rates. GeoResearch Forum 5, 15–40.

Santana, A., C. Porter, N. Butorovic, and C. Olave, 2006. First climatologic antecedents of automatic weather stations (AWS) in the Beagle Channel, Magallanes, Chile, Anales Instituto Patagonia 34, 5-20.

Santana, A., C. Porter, N. Butorovic, and C. Olave, 2007. Climatic characteristics in the Brecknock Channel at 54°30' S latitude, Magallanes, Chile, Anales Instituto Patagonia 35, 1, 5-18.

Schneider, C., Glaser, M., Kilian, R., Santana, A., Butorovic, N. and Casassa, G., 2003. Weather observations across the Southern Andes at 53°S. Physical Geography, 24, 2, 97-119.

Schumer, R. and Jerolmack, D. J., 2009. Real and apparent changes in sediment deposition rates through time. Journal of Geophysical Research, 114, F00A06, doi: 0.1029/2009JF001266

Smellie, J. L., McArthur, J.M., McIntosh, W.C. and Esser, R., 2006. Late Neogene interglacial events in the James Ross Island region, northern Antarctic Peninsula, dated by Ar/Ar and Sr-isotope stratigraphy. Palaeogeography, Palaeoclimatology, Palaeoecology, 242, 3-4, 8, 169-187, ISSN 0031-0182, doi: 10.1016/j.palaeo.2006.06.003.

Smellie, J.L., 1999. Lithostratigraphy of Miocene–Recent, alkaline volcanic fields in the Antarctic Peninsula and eastern Ellsworth Land. Antarctic Science, 11, 362–378.

Smellie, J.L., Johnson, J.S., McIntosh, W.C., Esser, R., Gudmundsson, M.G., Hambrey, M.J. and van Wyk De Vries, B., 2008. Six million years of glacial history recorded in the James Ross Island Volcanic Group, Antarctic Peninsula. Palaeogeography, Palaeoclimatology and Palaeoecology, 260, 122–148.

Smith, R. C. and Stammerjohn, S. E., 1996. Surface air temperature variations in the western Antarctic Peninsula region. Foundations for ecological research west of the Antarctic Peninsula, Antarctic Research Series, 70, 105-121.

Smith, R. T., 2009. Evolution of the Antarctic Peninsula continental margin from Late Eocene to present: Seismic stratigraphic analysis related to the development of the Antarctic Peninsula Ice Sheet (APIS). PhD thesis, pp. 124, Earth Science Department, Rice University, Houston, Texas.

Smith, T. R., and Anderson, J. B., 2010. Ice sheet evolution in James Ross Basin, Weddell Sea margin of the Antarctic Peninsula: the seismic stratigraphic record, Geological Society of America Bulletin 122 p. 830-842.

Spotila, J. A., Buscher, J. T., Meigs, A. J. and Reiners, P. W., 2004. Long-term glacial erosion of active mountain belts: Example of the Chugach–St. Elias Range, Alaska. Geology, 32, 501-504, doi: 10.1130/G20343.1.

Stappung, C. A., 2000. Lluvias de diseño de sistemas de aguas lluvias en chile. Revista de Ingenieria de Chile, 429, 112, 1.

Stravers, J.A. and J.P.M. Syvitski, 1991. Land-sea correlations and evolution of the Cambridge Fiord marine basin during the last deglaciation of northern Baffm Island, Quaternary Research 35, 72-90.

Strelin, J., Casassa, G., Rosqvist, G. and Holmlund, P., 2008. Holocene glaciations in the Ema Glacier valley, Monte Sarmiento Massif, Tierra del Fuego. Palaeogeography, Palaeoclimatology, Palaeoecology, 260, 299-314.

Sugden, D.E., M.J. Bentley, C.J. Fogwill, N.J.R. Hulton, R.D. McCulloch, and R.S. Purves, 2005. Late-glacial glacier events in southernmost South America: A blend of 'northern' and 'southern' hemispheric climate signals?, Geografiska Annaler 87A, 2, 273-288.

Svendsen, J. I., J. Mangerud, and G.H. Miller, 1989. Denudation rates in the Arctic estimated from lake sediments on Spitsbergen, Svalbard, Palaeogeography, Palaeoclimatology, Palaeoecology 76, 153-168.

Syvitski, J. P. M. and Milliman, J. D., 2007. Geology, geography, and humans battle for dominance over the delivery of fluvial sediment to the coastal ocean. The Journal of Geology, 115, 1–19.

Syvitski, J.P.M., 1989. On the deposition of sediment within glacier-influenced fjords: oceanographic controls. Modern Glacimarine Environments: Glacial and Marine Controls of Modern Lithofacies and Biofacies, In: R.D. Powell and A. Elverhoi, Eds., Marine Geology 85, 301-329.

Thomson, S. N., Brandon, M. T., Tomkin, J. H., Peter , W., Reiners, P. W., Vasquez, C. and Wilson, N. J., 2010. Glaciation as a destructive and constructive control on mountain building. Nature, 467, 313–317, doi: 10.1038/nature09365.

Turner, J., Lachlan-Cope, T. A., Marshall, G. J., Morris, E. M., Mulvaney, R. and Winter,W., 2002. Spatial variability of Antarctic Peninsula net surface mass

balance. Journal of geophysical research, 107, D13, 4173, doi: 10.1029/2001JD000755,

Turner, K. T., Fogwill, C. J., McCulloch, R. D. and Sugden, D. E., 2005. Deglaciation of the eastern flank of the Northern Patagonia Icefield and associated continental-scale lake diversions. Geografiska Annaler, 87A, 2, 363-374.

Villalba, R., 1994. Tree-ring and glacial evidence for the medieval warm epoch and the Little Ice Age in southern South America. Climatic Change, 26, 183-197.

Villa-Martínez, R. and Moreno, P. I., 2007. Pollen evidence for variations in the southern margin of the westerly winds in SW Patagonia over the last 12,600 years. Quaternary Research, 68, 400-409.

Villa-Martínez, R., Villagran, C. and Jenny, B., 2003. The last 7500 cal yr B.P. of westerly rainfall in Central Chile inferred from high-resolution pollen record from Laguna Aculeo (34°S). Quaternary Research, 60, 284-293.

Warren, C. R., 1993. Rapid recent fluctuations of the calving San Rafael Glacier, Chilean Patagonia: climatic or non-climatic?. Geografiska Annaler, 75A, 3, 111-125.

Warren, C. R. and Sudgen, D. E., 1993. The Patagonian Icefields: a glaciological review. Arctic and Alpine Research, 25, 4, 316-331.

Wenzens, G., 1999. Fluctuations of outlet and valley glaciers in the Southern Andes (Argentina) during the Past 13,000 Years. Quaternary Research, 51, 238-247.

Whipple, K. X., 2009. The influence of climate on the tectonic evolution of mountain belts. Nature Geoscience, 2, 97-104, doi: 10.1038/NGEO413.

Willenbring J., Von Blanckenburg, F., 2010. Long-term stability of global erosion rates and weathering during late-Cenozoic cooling. Nature, 465, 211–214, doi:10.1038/nature09044.

Winchester, V. and Harrison, S., 1996. Recent oscillations of the San Quintin and San Rafael glaciers, Patagonian Chile. Geografiska Annaler, 78, 1, 35-49.

Appendix A

A1

Radiocarbon analysis included a total of 31 carbonate samples. All carbonate material, mainly bivalves, was picked and washed before analysis. Samples were processed by the National Ocean Sciences Accelerator Mass Spectrometer facility (NOSAMS) at Woods Hole Oceanographic Institute and at the W. M. Keck Carbon Cycle Accelerator Mass Spectrometry Lab at the University of California, Irvine. All results were calibrated using CALIB Radiocarbon Calibration Program Version 5.0 (Stuiver and Reimer, 1993; Stuiver et al., 2005) using the marine calibration curve for the southern hemisphere and using an additional reservoir correction of 140 years. This correction was used based on the assumption that surface samples represent modern deposition.

Area	Lab	Core	Depth [cm]	Sed. Facies	14C age [yr BP]	(+- yr)	D13C	Reservoir [yr]	calibrated age [cal BP]
Outer Basin	UCI	NBP0505_JPC67	70	SM	1735	15	–	140	1160
	WHOI	NBP0505_JPC67	195	SM	2950	40	3.3	140	2560
	WHOI	NBP0505_JPC67	266	SM	3760	35	3.71	140	3520
	WHOI	NBP0505_JPC67	351	SM	5070	55	3.37	140	5260
	WHOI	NBP0505_JPC67	398	SM	5270	55	2.08	140	5490
	WHOI	NBP0505_JPC67	486	SM	7860	40	2.8	140	8190
	UCI	NBP0505_JPC67	707	SM	10,760	20	–	140	11,930
	WHOI	NBP0505_JPC67	770	SM	11,400	60	1.57	140	12,850
	UCI	NBP0505_JPC67	915	SM	11,615	50	–	140	12,990
	WHOI	NBP0505_JPC67	940	SM	12,050	60	–6.12	140	13,350
	UCI	NBP0505_KC66	105	SM	2080	85	–	140	1490
	UCI	NBP0505_KC66	275	SM	3635	45	–	140	3380
	WHOI	NBP0505_JPC77	15	SM	635	30	0.8	140	120
	WHOI	NBP0505_JPC77	255	SM	4830	40	2.22	140	4920
	WHOI	NBP0505_JPC77	400	SM	7710	40	2.04	140	8030
	WHOI	NBP0505_JPC77	540	SM	10,550	50	1.73	140	11,490
	WHOI	NBP0505_JPC77	722	SM	13,050	65	3.06	140	14,620
	WHOI	NBP0505_JPC77	782	SM	13,650	70	3.43	140	15,500
Medial Basin	WHOI	NBP0505_JPC47	1117	PM	780	30	1.68	140	290
	WHOI	NBP0505_JPC52	273	PM	670	30	1.12	140	160
	WHOI	NBP0505_JPC63	461	PM	735	25	2.3	140	230
	WHOI	NBP0505_JPC63*	525	PM	660	30	0.12	140	150
	WHOI	NBP0505_JTC70	91	PM	615	30	1.12	140	100
	WHOI	NBP0505_JPC75	565	PM	660	25	1.28	140	150
Ainsworth Fjord	UCI	NBP0505_JPC57	109	PM	660	15	–	140	150
	UCI	NBP0505_JPC57	325	PM	685	15	–	140	180
	UCI	NBP0505_JPC57	875	PM	860	20	–	140	370
	WHOI	NBP0505_JPC57	993	D	7840	40	2.81	140	8170
	WHOI	NBP0505_JPC60	482	D	8080	45	1.5	140	8400
	WHOI	NBP0505_JPC71	463	PM	595	35	0.67	140	80
	WHOI	NBP0505_JPC71	1036	PM	815	30	2.69	140	330

SM: Silty Mud Lithofacies; PM: Pebbly Mud Lithofacies; D: Diamicton Lithofacies. (*) out of sequence.

Medial basin Accumulation Rate:

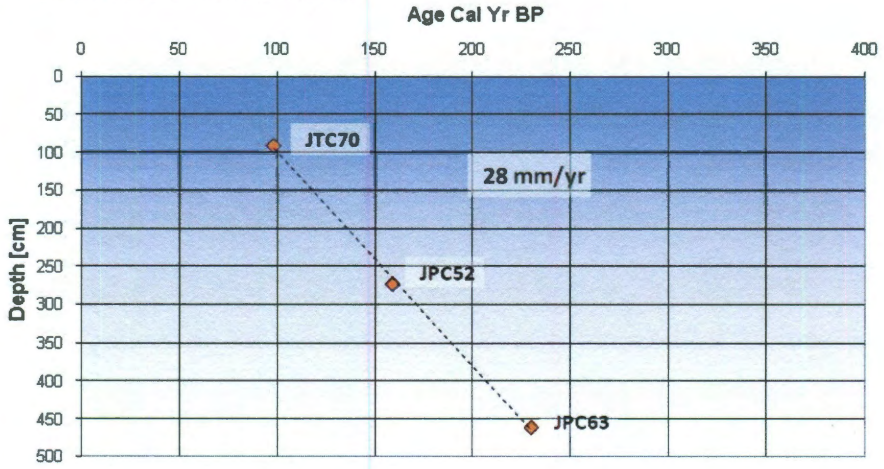

Outer Basin Age Model (JPC67):

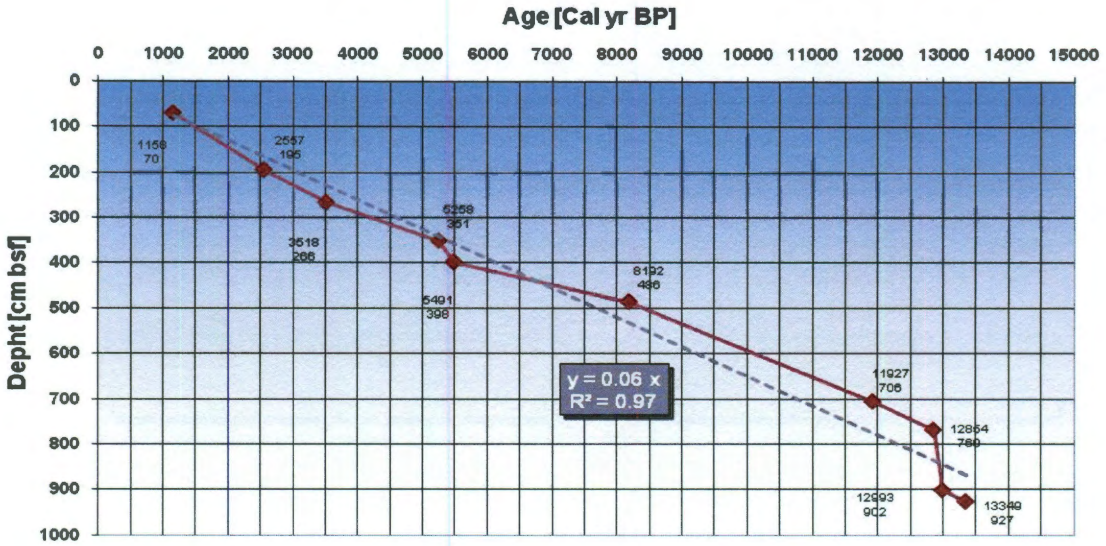

References

Stuiver, M., Reimer, P.J., 1993. Extended 14C database and revised CALIB radiocarbon calibration program, Radiocarbon 35, 215-230.

Stuiver, M., Reimer, P.J., Reimer, R.W., 2005. CALIB 5.0. [http://calib.qub.ac.uk/calib/]

A 2

Table showing the dataset used to construct Figure 5. In yellow are the silty sediments used in combination with data from the SHALDRIL project in Maxwell Bay, King George Island, Antarctica, to estimate the range of densities of glacimarine sediments for similar geologic settings.

Reference	*Sediment Type*	*density* g/cm^3	*Vp* m/s	*note*
Hamilton EL, 1971	Coarse sand	2.03	1836	continental terrace (shelf and slope)
	fine sand	1.98	1742	
	very fine sand	1.91	1711	
	silty sand	1.83	1677	
	sandy silt	1.56	1552	
	sand-silt-clay	1.58	1578	
	clayey silt	1.43	1535	
	silty clay	1.42	1519	
	clayey silt	1.38	1535	abyssal plain (turbidite)
	silty clay	1.26	1521	
	clay	1.26	1505	
	clayey silt	1.41	1531	abyssal hill (pelagic)
	silty clay	1.37	1507	
	clay	1.42	1491	
	silty mean	1.47	1550.6	
Hamilton EL et Bachman, 1982	Coarse sand	2.03	1836	continental terrace (shelf and slope)
	fine sand	1.96	1759	averaged values
	very fine sand	1.88	1709	
	silty sand	1.78	1658	
	sandy silt	1.77	1644	
	silt	1.74	1615	
	sand-silt-clay	1.58	1582	
	clayey silt	1.49	1546	
	silty clay	1.48	1517	
	silty mean	1.64	1593.7	
Hamilton EL et Bachman, 1982	clayey silt	1.45	1528	Abyssal plain
	silty clay	1.36	1515	averages values (for all)
	clay	1.35	1503	
	silt	1.45	1546	Bering sea and Okhotsk sea
	clayey silt	1.23	1534	
	silty clay	1.21	1525	
	clayey silt	1.35	1522	Abyssal hill
	silty clay	1.34	1508	
	clay	1.41	1493	
	silty mean	1.34	1525.4	
Orsi TH et Dunn DA, 1991	sand	2.1	1734	Barent sea surface sediment average
	silty sand	1.4	1640	
	clayey sand	1.89	1620	
	sand-silt-clay	1.74	1575	
	clayey silt	1.64	1545	
	sandy clay	1.57	1531	
	silty clay	1.54	1510	
	clay	1.45	1496	
	silty mean	1.58	1567.5	

A3

To estimate the uncertainty derived from the use of a particular interpolation method to produce the raster seismic surfaces (SS) implicit in equation (3), we tested several methods available in ArcGis 9.3. If we assume that the swath bathymetry (SB) is the best possible image of the sea floor, the sea floor surface produced by the interpolation of the seismic data should be as similar as possible to SB.

Table 1 shows that all interpolation methods applied over the seismic dataset produced sea level-sea floor volumes smaller than the equivalent volume calculated from the SB dataset. The maximum difference was produced by the Natural Neighbors method (-1.9%), followed closely by TIN. The best approximation was obtained using a Spline interpolation with the "Tension" option (it adds the first derivative to the curvature minimization criteria; parameter used: weight=0.1, Number of points=10, cell size 50m). Hence, we used this method to build isopach maps and to calculate erosion rates. Figure 1 shows the swath bathymetry and the basement 3D surfaces obtained by this method.

Table: Second term in equation (3): $[P_A * V_p^w * (\Sigma_{ij} T_{ij}^w) - P_A * (\Sigma_{ij} B_{ij})]$

Interpolation method	SS Volume m^3	SS/SB %	[(3):SS-SB]/SB %
Triangular Irregular Network (TIN)	6985385152.3	98.5%	-1.5%
Inverse Distance Weighted (IDW)	7045249678.0	99.3%	-0.7%
SPLINE-regularized	6971989633.4	98.3%	-1.7%
SPLINE-Tension	7080765273.3	**99.8%**	**-0.2%**
Kriging	7041876302.3	99.3%	-0.7%
Natural Neighbors	6954911877.5	98.1%	-1.9%
Swath Bathymetry (SB)	7092676770.7	100.0%	0.0%

Note: $SS = P_A * V_p^w * (\Sigma_{ij} T_{ij}^w)$; $SB = P_A * (\Sigma_{ij} B_{ij})$

The following figure show surfaces representing the sea floor (data obtained from the swath bathymetry survey) and the acoustic basement (data from the seismic survey). The dots show the location of the discrete points used to map the seismic surfaces.

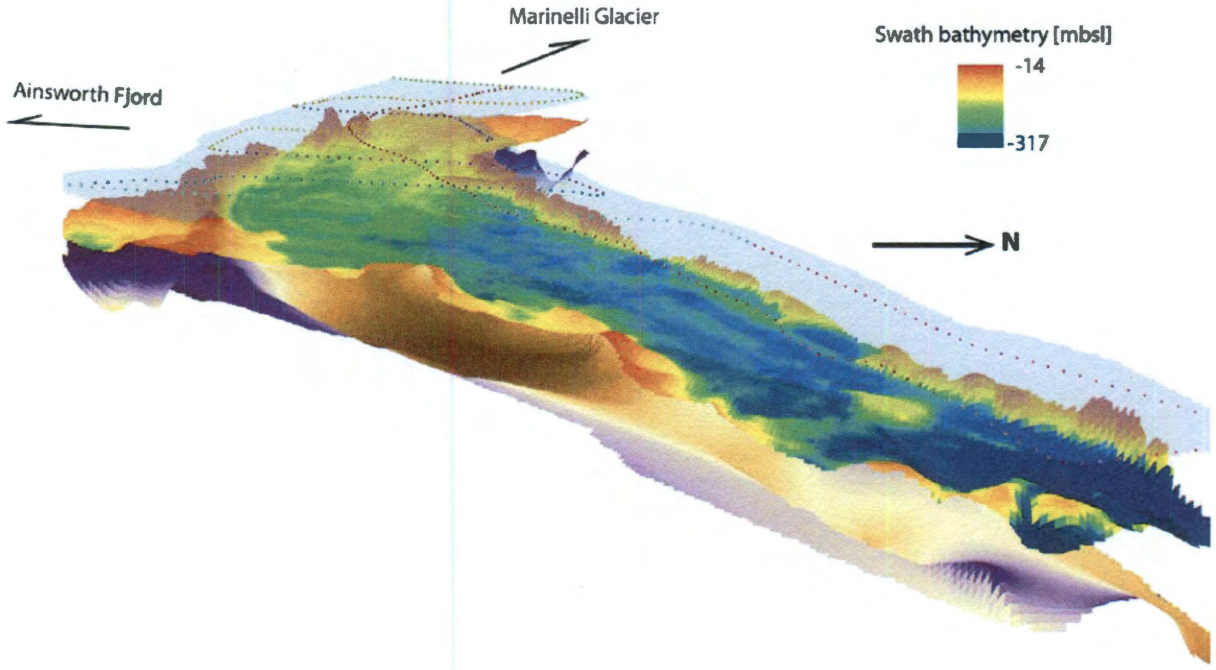

A 4

We argued in section 7.2 that *Koppes and Hallet*'s [2006] "long term" erosion rates, which were derived assuming a steady state condition (no retreat) of the glaciers, are limited to the last glacial event (Little Ice Age) and thus represent an approximation of basin wide erosion rates over centennial timescales.

As stated in the same section, in order to estimate the correct time span (T) that apply to the "lomg term" erosion rates estimated by *Koppes and Hallet* [2006], we arbitrarily multiplied the length of the monitored time period by a factor of 10. This has the implicit assumption that all these glaciers have behaved similarly during the last centuries keeping their relative erosion rates constant (i.e. Er's increased or decreased similarly through time for all of them). The following table shows the results of such approximation of T, the magnitude of centennial Er was estimated after Koppes et al. (2006):

Table: short and long term erosion rates of Alaskan glaciers (from Hallet et al. [1996]).

	Region	Glacier	T [yr]	Er [mm/yr]	Reference
Short Term	SE Alaska	Lituya/N. Crillon	33	45.2	Jordan, 1962
	SE Alaska	Crillon	35	12.0	Powell, 1991
	SE Alaska	Icy Bay	54	16.7	Molnia, 1985
	SE Alaska	Muir Inlet	80	16.0	Stravers and Syvitski, 1991
	SE Alaska	Grand Pac./Margerie	86	6.0	Merrand, 1994
	SE Alaska	Johns Hopkins	87	47.2	Cai, 1994
	SE Alaska	Hubbard	700	13.7	Carlson, 1989
Long Term	SE Alaska	Lituya/N. Crillon	330	11.3	Er after Koppes et al, 2006
	SE Alaska	Crillon	350	3.0	Er after Koppes et al, 2006
	SE Alaska	Icy Bay	540	4.2	Er after Koppes et al, 2006
	SE Alaska	Muir Inlet	800	4.0	Er after Koppes et al, 2006
	SE Alaska	Grand Pac./Margerie	860	1.5	Er after Koppes et al, 2006
	SE Alaska	Johns Hopkins	870	11.8	Er after Koppes et al, 2006
	SE Alaska	Hubbard	7000	3.4	Er after Koppes et al, 2006
Notes: Timescale factor is 10, thus T'=T*10 and Er'=Er/4 according to Koppes et al. (2006)					

If these short and long term data are visualized in a log-log plot as the one in Figure 10, the data will follow approximately a power law function $y = 94.406x^{-0.424}$ and will overlapping with the data points from Marinelli glacier. The following is such a plot, the red dots are the short-term Er and the blue ones correspond to the equivalent long-term Er according to our estimates:

Graph: <Er> v/s short and estimated long term time-spans:

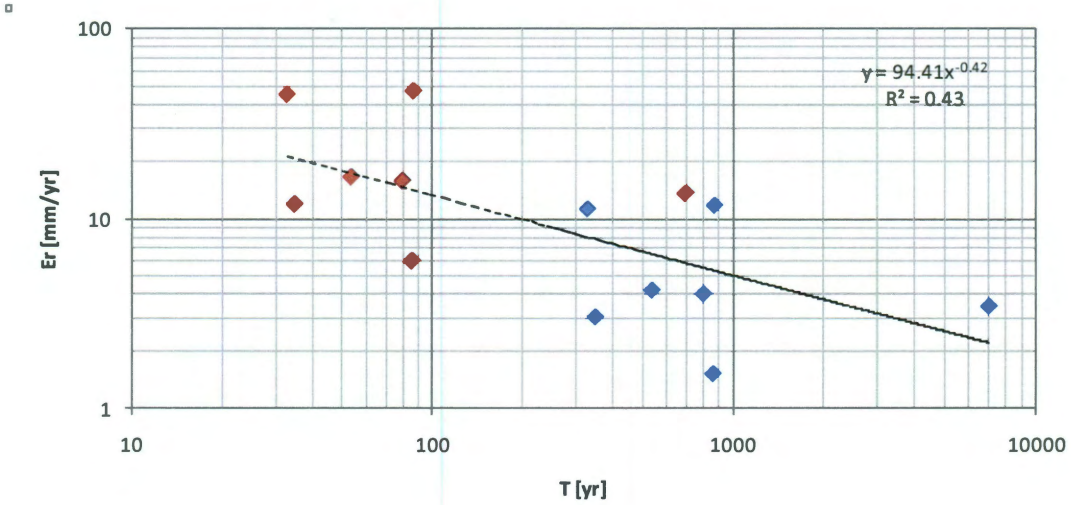

In order to test the sensitivity of this estimates respect to the multiplicative factor used to estimate T, we tried other factors in the vicinity of 10. For doing so, we used the interval [2,20] that contains probably all possibly reasonable factors to use. The following table and plot show that the log-log slope of the Er vs T plots is relatively insensitive to the multiplicative factor within the interval [2,20], and that the reduction factor for Er corresponding to a ten-fold increase in time span using 10 as multiplicative factor is close to the median.

Table: Multiplicative factor and decrease of <Er> for a ten-fold increase in time span (T).

Multiplicative factor of T	exponent of the best fit power - law curve	reduction factor to estimate <Er> given a ten-fold increase in T	percentage of <Er> decrease given a ten-fold increase in T
2	-0.379	2.4	58.2%
3	-0.439	2.7	63.6%
4	-0.454	2.8	64.8%
5	-0.455	2.9	64.9%
6	-0.451	2.8	64.6%
7	-0.444	2.8	64.0%
8	-0.438	2.7	63.5%
9	-0.431	2.7	62.9%
10*	**-0.424**	**2.7**	**62.3%**
11	-0.418	2.6	61.8%
12	-0.412	2.6	61.3%
13	-0.407	2.6	60.8%
14	-0.402	2.5	60.4%
15	-0.397	2.5	59.9%
16	-0.392	2.5	59.4%
17	-0.388	2.4	59.1%
18	-0.384	2.4	58.7%
19	-0.38	2.4	58.3%
20	-0.377	2.4	58.0%
*: factor used in the "Discussion" section.			

Finally, all reasonable multiplicative factors produce Er reduction factors higher than those obtained for the glaciers from Svalbard (1.8 and 2.2; see section 7.2).

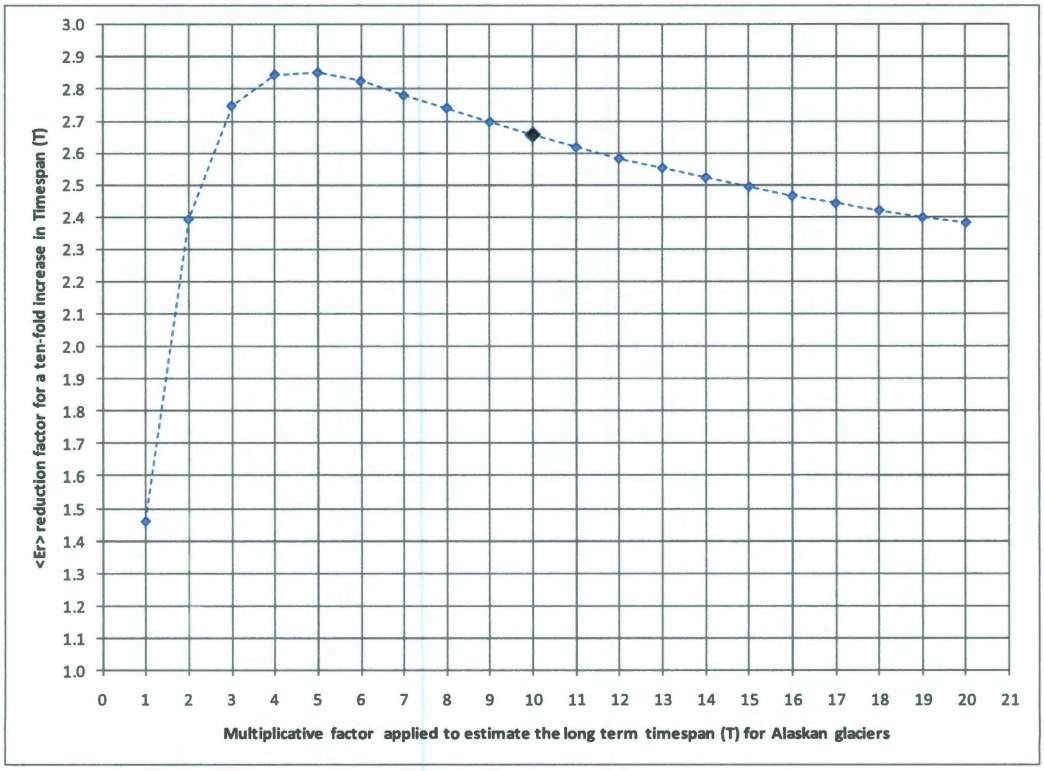

Appendix B

B1: Methodology, details

The sub-bottom profiler system used was a Bathy2000; only gain adjustments were made to this dataset before interpretation. The single channel seismic data were collected using a 50 cubic inch air gun coupled with a single-channel streamer. Seismic data were recorded using OYO DAS and Triton Elics data loggers, with minimal processing (bandpass filtering and gain adjustment). The two seismic datasets were combined and analyzed together in order to define seismic units. For doing so, time dependent records were transformed to depth sections using a P-wave velocity of 1500 m/s, and analyzed in a GIS suite (ArcGIS 9.3) to compare features in the horizontal axis.

The swath bathymetry data were manually edited and processed onboard using the Unix suite MBSystem to remove anomalous beams and to produce real-time plots, working maps, and ASCII files. These data were used to assist in selecting the coring sites, study the submarine geomorphology, and correct the sea floor depth in the seismic profiles.

Thirteen samples were analyzed at the National Ocean Sciences Accelerator Mass Spectrometry Facility (NOSAMS) to obtain radiocarbon ages. Samples were of two types: complete or fragments of mollusks shells, and plant material composed of leaves and small pieces of twigs (Table 3.1). Ages were calibrated with Oxcal 4.1 using curve SHCal04, and a reservoir age of 480 yr was calculated as the difference between the linear interpolations of plant and carbonate radiocarbon ages for the core interval where

both types of samples occurred (JPC14: 200-700 cm; in the following figure note the similar slopes of the two lines that interpolate the ages obtained from plant material and carbonate shells).

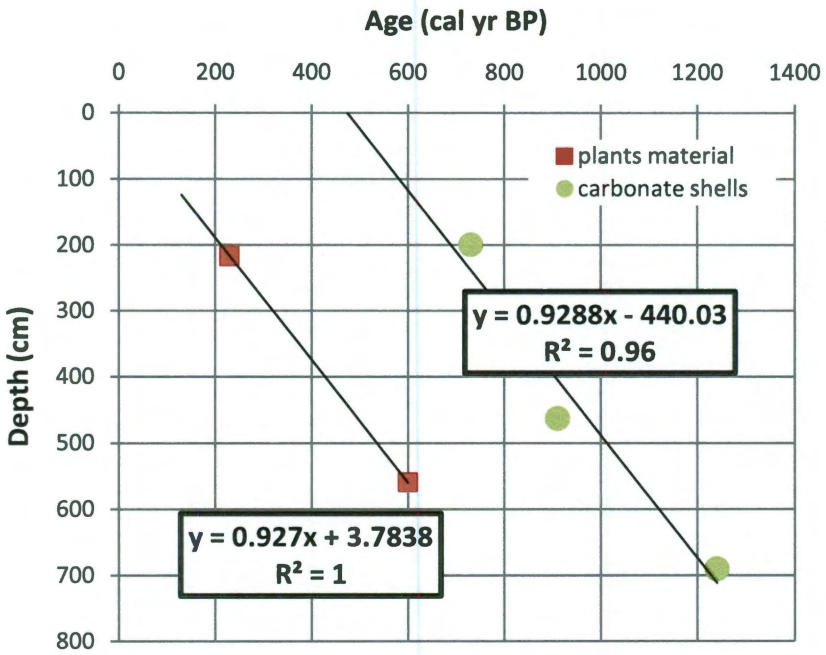

Grain-size was measured on the terrigenous fraction using a Coulter LS200 laser grain-size analyzer. To isolate the terrigenous fraction, samples were treated with boiling H_2O_2 and HCl to remove organic matter and carbonate, respectively. No alkaline treatment was applied since diatoms were never observed in smear slides made throughout the core. Prior to analysis, samples were boiled with 300 mg of sodium pyrophosphate ($Na_4P_2O_7$ $10H_2O$) to ensure complete disaggregation of the particles.

Total Organic Carbon (TOC) was measured on selected samples using a PDZEuropa ANCA-GSL elemental analyzer at the UCDavis Stable Isotope Facility. Before analysis, samples were decarbonated with 1N Sulfurous Acid.

Physical properties including magnetic susceptibility, gamma ray density and fractional porosity were measured at the Antarctic Marine Geology Facility at Florida State University on a GEOTEK™ Multi Sensor Core Logger (MSCL). X-ray radiographs were also analyzed to study sedimentary structures and to search for carbonate material for radiocarbon analysis.

Sediment discharge from Gualas River was estimated from the volume of seismic units imaged in the 3.5 kHz and air-gun seismic profiles (Figures 3.2, 3.3, 3.4a, 3.4b and Appendix B2). These volumes were transformed into rock-equivalent volumes using densities between 2.2-2.4 $*10^3$ kg/m^3 according to the values measured with the MSCL, and an estimated 2.7 $*10^3$ kg/m^3 for the parental rock (mainly granitoids; SERNAGEOMIN, 1:1000000 Digital Map, 2003). This volume was divided by the estimated time span of accumulation using the age model from core JPC14. Finally, using the grain size distributions of the same core, total yields of sand, silt and clay represented by each unit were obtained by calculating the volumetric percentage of each size fraction.

B2: Seismic Line 9, chirp sub-bottom profiler system (Bathy2000).

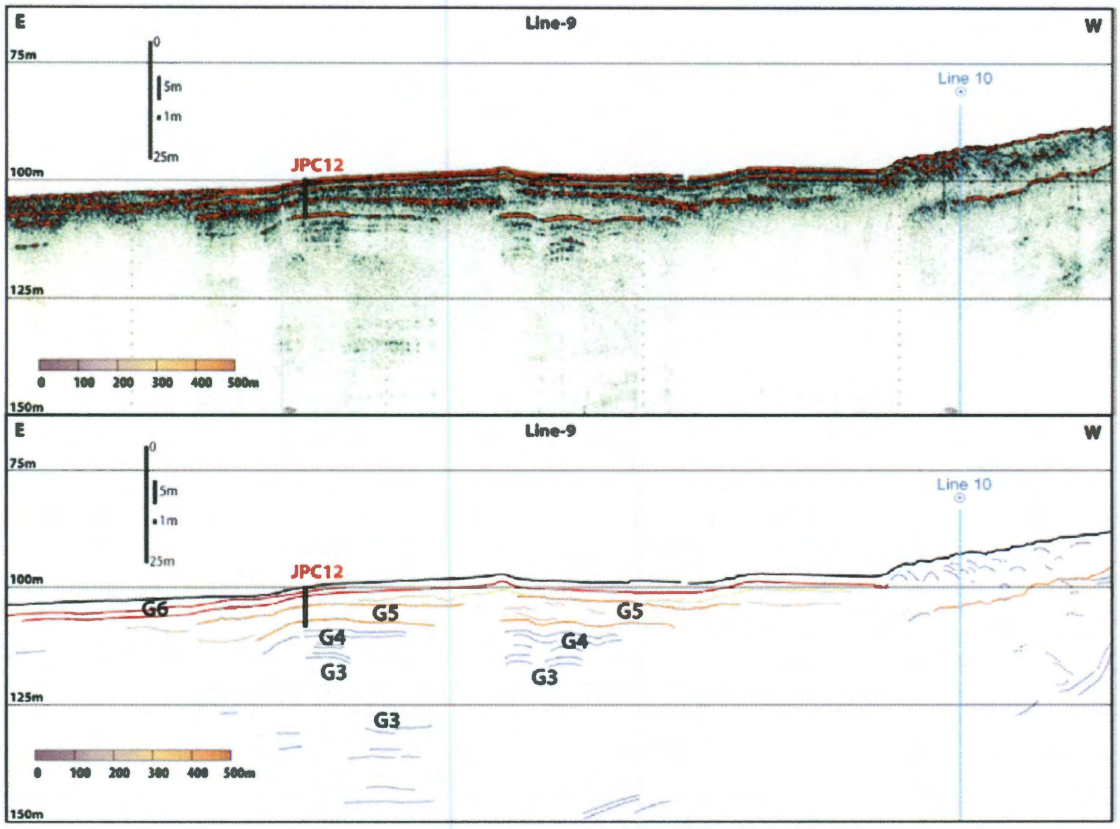

B3: Seismic units, details.

Seismic Unit G1

In the western part of Line 5, near the two arcuate moraines that surround Golfo Elefantes (Figures 3.3 and 3.4b), there is about 25m of subhorizontal low amplitude reflections,. This unit is believed to have formed by settling from suspension of sediments in a low energy (distal) environment. Further study is needed to establish the age and nature of this unit but it could reflect interglacial sedimentation during the waning stages of the local LGM.

Seismic Unit G2

Unit G2 is characterized by relatively strong reflections roughly parallel to the interpreted (acoustic) basement (Figure 3.3). This unit was not sampled by the cores since it occurs at depths greater than 15 m below the sea floor. It resembles other seismic units that are believed to be composed of ice-proximal sediments in other Patagonian fjords, including Marinelli Fjord (daSilva, 1997; Boyd, 2008; Fernandez et al., 2011), and Fjord Europa (unpublished seismic records). In areas where this unit is imaged, it appears to rest directly on bedrock or moraine deposits (acoustic basement) and is laterally continuous and of uniform thickness over large areas. The only exception occurs in the far western portion of Line 5, where the unit seems to lose lateral continuity or has been displaced by normal faulting at ~16 mbsf.

Seismic Unit G3

Unit G3 is composed of parallel, near horizontal reflections of medium-low amplitude, and transparent intervals of variable thickness (>2m). These reflections onlap the sinuous and relatively well defined contact with underlying unit G2. Unit G3 filled depressions in the sea floor, resulting in a smoother bathymetry. Unit G3 is interpreted to have formed by settling from suspension from a relatively dense plume of sediments across the lower areas of Golfo Elefantes.

Seismic Unit G4

Unit G4 has variable thickness (<10m), with a low-relief upper boundary (Figure 3.4a and 3.4b). In general, G4 is characterized by discontinuous strong reflections when visible. As seen in the center of Lines 3, 5, and 10, unit G4 onlaps underlying unit G3 (Figure 3.4a and 3.4b), although the contact is difficult to follow due to its irregular and discontinuous shape. In general, its thickness decreases to the west and north, but in the northern part of the section (Line 3) it thickens, exhibiting a lenticular shape. In this area, the seismic architecture resembles a stack of lenticular bodies. This, along with the increase in thickness of the unit in this area and the fact that the sea floor slopes toward the east, indicates a transport direction from east to west. Around the center of Golfo Elefantes, where Lines 3, 10 and 5 intersect and this unit onlaps underlying unit G3, it shows deformed reflections that might be produced by gas disturbances.

In the southern part of the basin, Lines 3 and 10 show parallel reflections of variable intensity that extend to near 50 m below the sea surface (Figure 3.3 and Appendix B2). Unfortunately low penetration in the center of the lines prevents direct correlation between unit G4 and parallel reflections of the southern section. However, G6 can be easily identified by two strong reflections that define its upper and lower boundaries (~2.25 m thickness). Underlying G6, there is a sequence of low amplitude and high frequency reflections similar in character to unit G5 in the center of the basin. This sequence is interrupted by a strong reflection at ~9 mbsf that is correlated with the top of unit G4; either a strong reflection at ~16 mbsf or the change of the seismic facies to a low amplitude/frequency sequence at ~18 mbsf might correspond to the lower portion of G4 (Appendix B2). G4 was also imaged in Line 9, which extends from southeast Golfo Elefantes E-W across the basin and through the location of JPC12. It imaged the upper boundary of unit G4 at ~7-8 mbsf, whereas its lower boundary is located at ~15-16 mbsf (Appendix B2). Hence, in the southern part of Golfo Elefantes, unit G4 is between 7 and 9 m thick, more than double its thickness at the location of JPC14.

Based on the overall thinning of the section towards the north and west, we interpret sediment supply to have been mainly from the south and east, predominantly from the south in the southern part of the basin and from the east in the northern part. The contact with the underlying unit in the northern part of the basin exhibits an erosional (irregular) geometry, indicating that the upper part of the underlying unit might be missing. Near the center of the basin, the contact is obscured by gas disturbance, whereas in the southern part of the basin it is concordant and difficult to identify. At the location

of core JPC14, the seismic architecture suggests that only the top 3 meters of this unit were sampled (Figure 3.4b).

Seismic Unit G5

Unit G5 is characterized by medium-low amplitude reflections alternating with transparent intervals indicating thin bedding of approximately 40 cm thickness (the approximate vertical resolution of our equipment). This unit downlaps at low angles onto the underlying unit G4 and thins to the north in lines 3 and 10. It maintains low angles of downlap towards the west in line 5, thinning in the same direction. Therefore, the sediment supply is from SE to NW. A data wipeout near the center of line 5 is likely due to the presence of gas in the sediment.

Seismic Unit G6

The youngest seismic unit, G6, is bounded by two strong continuous and roughly parallel reflections separated by up to~2.5 m (from peak to peak) in the central part of the basin and that loose continuity and pinch out toward the north (lines 3 and 10; Figure 4a) and, to a lesser extent, to the west (lines 5 and 4; Figure 4b). This indicates that the source of sediments was from the south and the east. The internal reflections (between one and three) of this unit show lower intensity and some discontinuities; they are parallel to the lower boundary in line 5 but downlap at low angles onto it in lines 3 and 10. This suggests that the main sediment supply is from south in the central part of the basin.

B1: Gran size distribution of seismic units

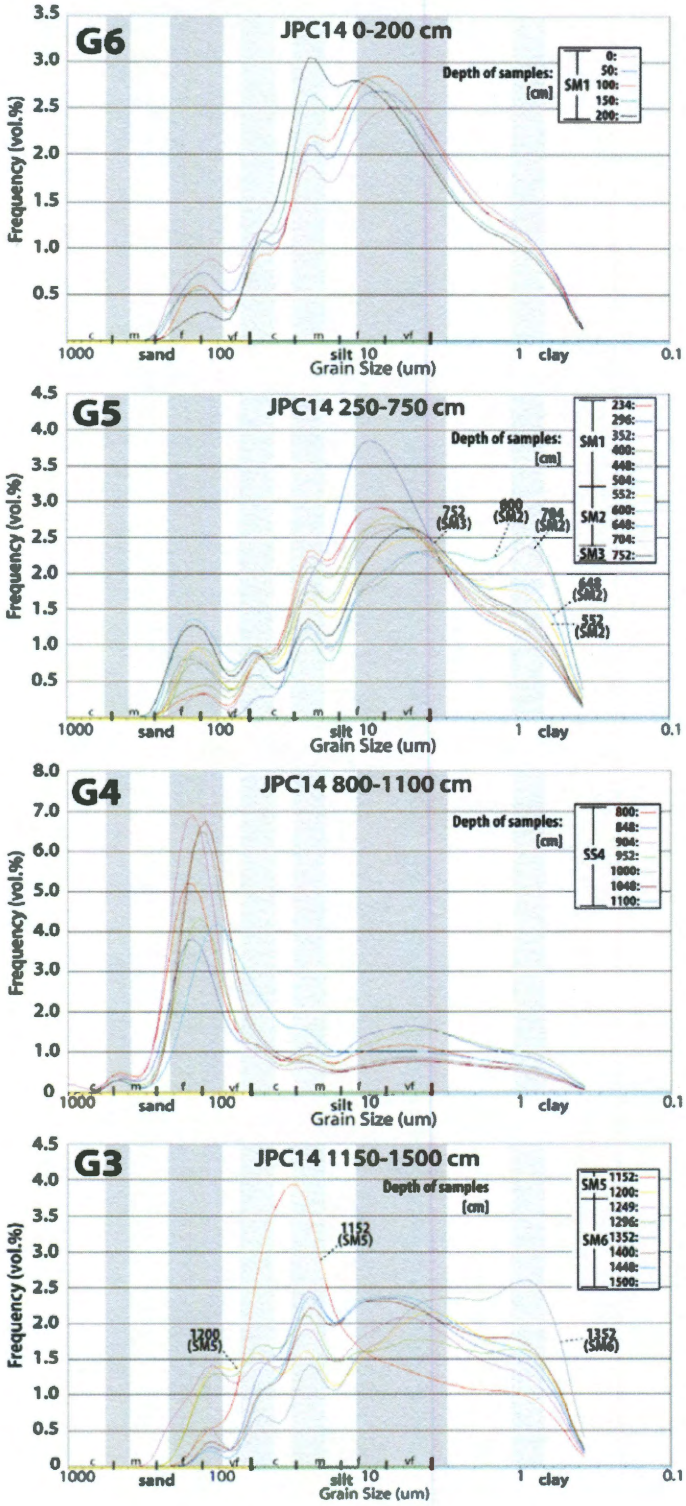

The figure shows the grain size distribution curves of selected samples from core JPC14 (50 cm sample interval) grouped according to respective seismic units. The dark gray strips show that the characteristic grain populations of G4 are all present in the other units, except for the medium-coarse sand population. The lighter gray strips show that some of the characteristic populations of units G3, G5 and G6are also present, although in low proportion, in G4.

The grain size distribution of samples from unit G6 shows a predominance of silt and a slight negative (longer tail towards the fine fraction) to near symmetrical distribution that results from the association of different proportions of an unsorted suspension mode (silts and clays) and a well sorted saltation mode (fine to very fine sand) (see Figure).

The grain size distribution of G5 ranges from fine sand to clay (see Figure). Samples of G5 belonging to the bottom of sedimentary unit SM1 show similar grain size distributions than samples of G6. In contrast, samples of G5 that belong to sedimentary units SM2 and SM3 (~520.5-796.5 cm) are positively skewed (i.e., longer tail towards the coarse fraction; see Figure) and composed dominantly of clay with some silty laminations <0.5 cm thick and sand content between 10-20%. This, plus poor sorting near the bottom of unit G5, indicate high turbidity during transport and deposition in a quiescent setting.

The grain size distribution of unit G4 shows a distinct pattern relative to the rest of the sampled units, with strong negative skewness (i.e., longer tail toward the fine fraction) and a clear main mode corresponding to fine-very fine sand with a fine tail of silt and clay, although the same populations of grains can be distinguished in all the samples as shown in the Figure (gray stripes). Thus, G4 is characterized by relatively high sand content. However, this unit has the unique presence of pebbles at 997 cm and 1031 cm and a gravelly layer at 1085 cm, which, along with a small proportion of medium-coarse sand, may represent a small influx of ice-rafted debris (IRD) to the basin.

The overall grain size distribution of unit G3 is similar to the upper part of G5 (SM1) with near symmetrical grain size distribution. One exception is a mud interval

with ~30% of clays (see Figure 3.5) that has a positive skewness (i.e. longer tail towards the coarse fraction) and a distribution resembling sediments at the bottom of unit G5 (SM2 and SM3). Toward the contact with the upper unit (G4), the grain size distribution resembles that of G4 but with the mode in the silt fraction and very little sand.

Appendix C

C1

Table showing estimated 1970 temperature at several Antarctic Peninsula stations. The dataset corresponds to the READER database and it is accessible free of charge at: http://www.antarctica.ac.uk/met/READER/data.html

1970 was chosen because of the large number of stations that reported data around that time and because it is previous to the warming trend observed in all the datasets of the studied stations. The estimation is the approximate value of the interpolated data for 1970. Recent temperatures are estimated as the 1995 to most recent measured year within the dataset. This was done because temperature increase seems to reach a plateau after 1995 but interannual variability is quite high.

Station	lat(S)	long(W)	Average 1995 to recent T	last year with data	1970 aprox. Temperature	Difference: (1995 to recent)- 1970 aprox. T
Faraday	65.4	64.4	-2.5	2010	-4.3	1.8
Bellingshausen	62.2	58.9	-2	2010	-2.8	0.8
Ohiggins	63.3	57.9	-3.2	2008	-4.1	0.9
Marambio	64.2	56.7	-7.8	2009	-9.3	1.5
Arturo Prat	62.5	59.7	-1.8	2003	-2.9	1.1
Esperanza	63.4	57	-4.4	2010	-5.5	1.1
Marsh	62.2	58.9	-2.1	2009	-2.7	0.6
Ferraz	62.1	58.4	-1.5	2009	***	***
King Sejong	62.2	58.7	-1.5	2005	***	***
Jubany	62.2	58.6	-1.5	2008	***	***
Great Wall	62.2	59	-1.9	2005	***	***
Rothera	67.5	68.1	-3.8	2010	-6	2.2

The following plots show the estimated temperatures for 1970 and 1995 to recent (in C°). The dashed blue line represents the center line of the Antarctic Peninsula.

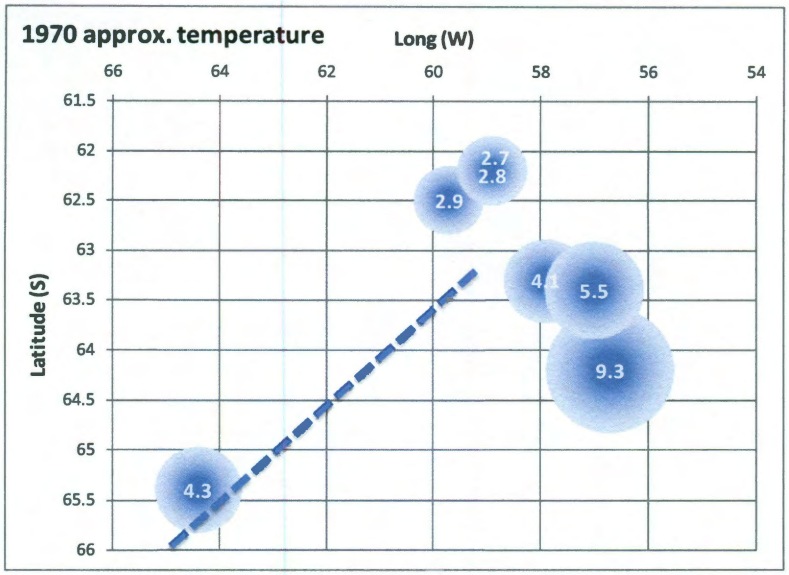

The following plots show temperature vs latitude and longitude. Faraday Station temperatures are off trend on the latitude plot, and seem to be higher than expected for its latitude. However, on the temperature vs longitude plot, even though Faraday Station temperatures are still off trend, the temperature difference with respect to the longitude of the closest station is smaller than respect to the latitude of the closest station. This is the result of a strong longitudinal trend in temperature distribution.

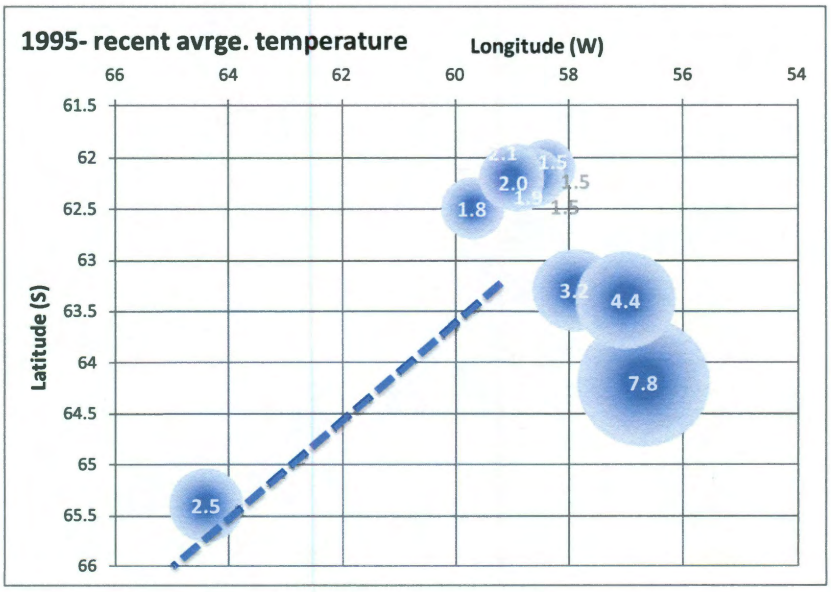

Temperature versus latitude

Temperature versus longitude

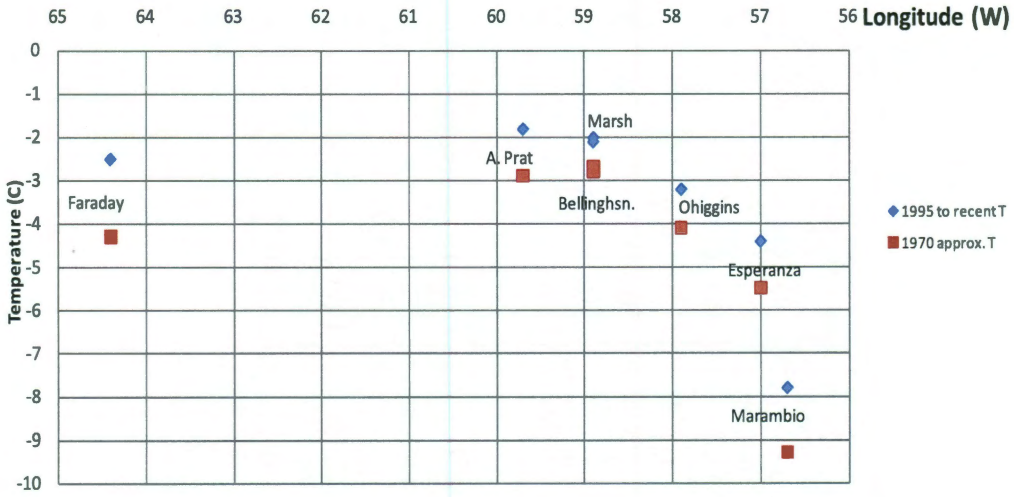

The following plots show the temperature difference between our estimated 1970 temperature and the 1995 to recent average. The top plot shows the location of the stations and their respective warming (in C°). The bottom plot shows that there is a strong correlation between warming and latitude: warming magnitude increases with latitude. This justifies our decision to analyze our millennial scale erosion rates using our estimated 1970 approximate temperature, since the use of more recent data would produce internal variability related to recent (transient?) differential climate behavior that might not represent long term internal differences.

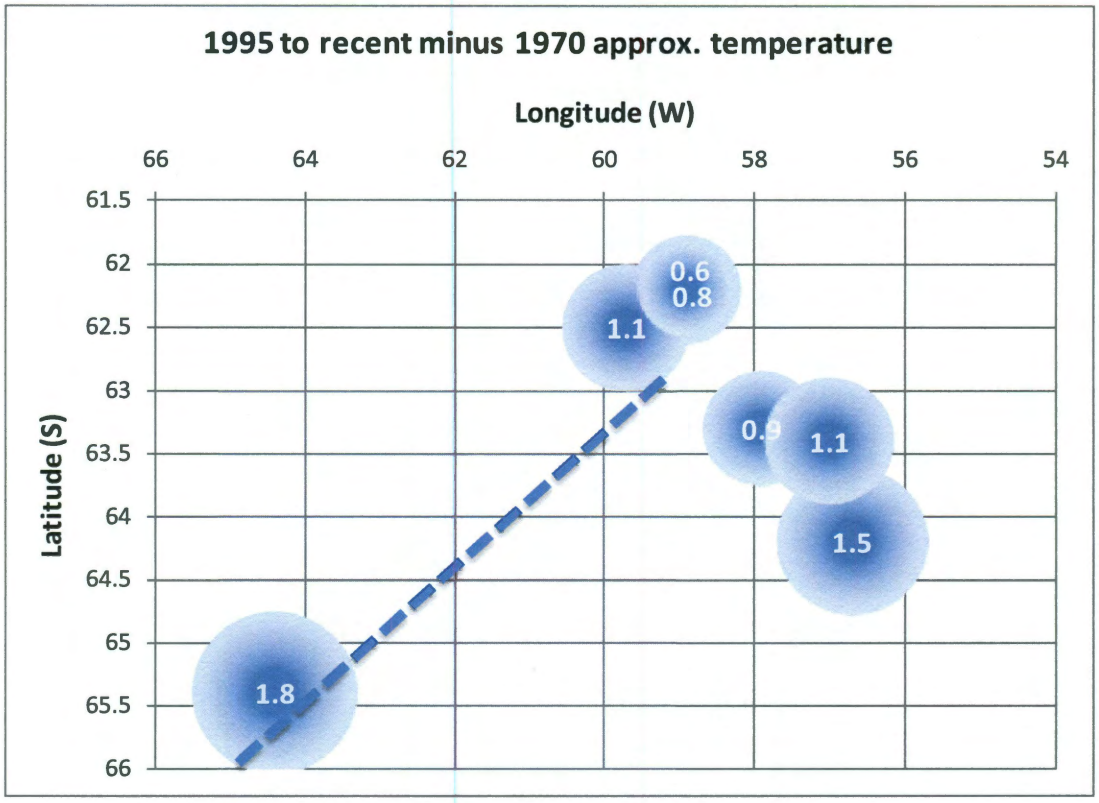

Difference between the "1995 to recent" and the approximate 1970 temperature as a function of latitude, showing that recent warming increases with latitude

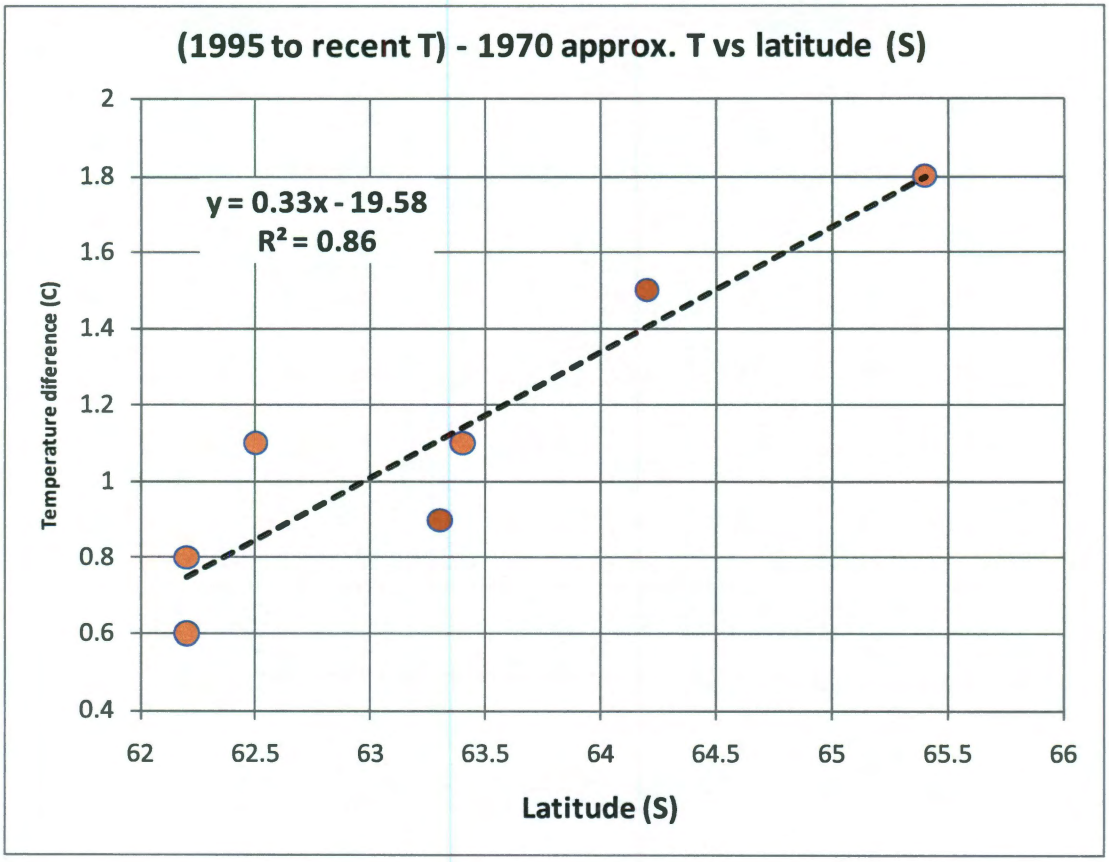

C2: Isopach maps

San Rafael Glacier area:

Europa Glacier and Europa Fjord:

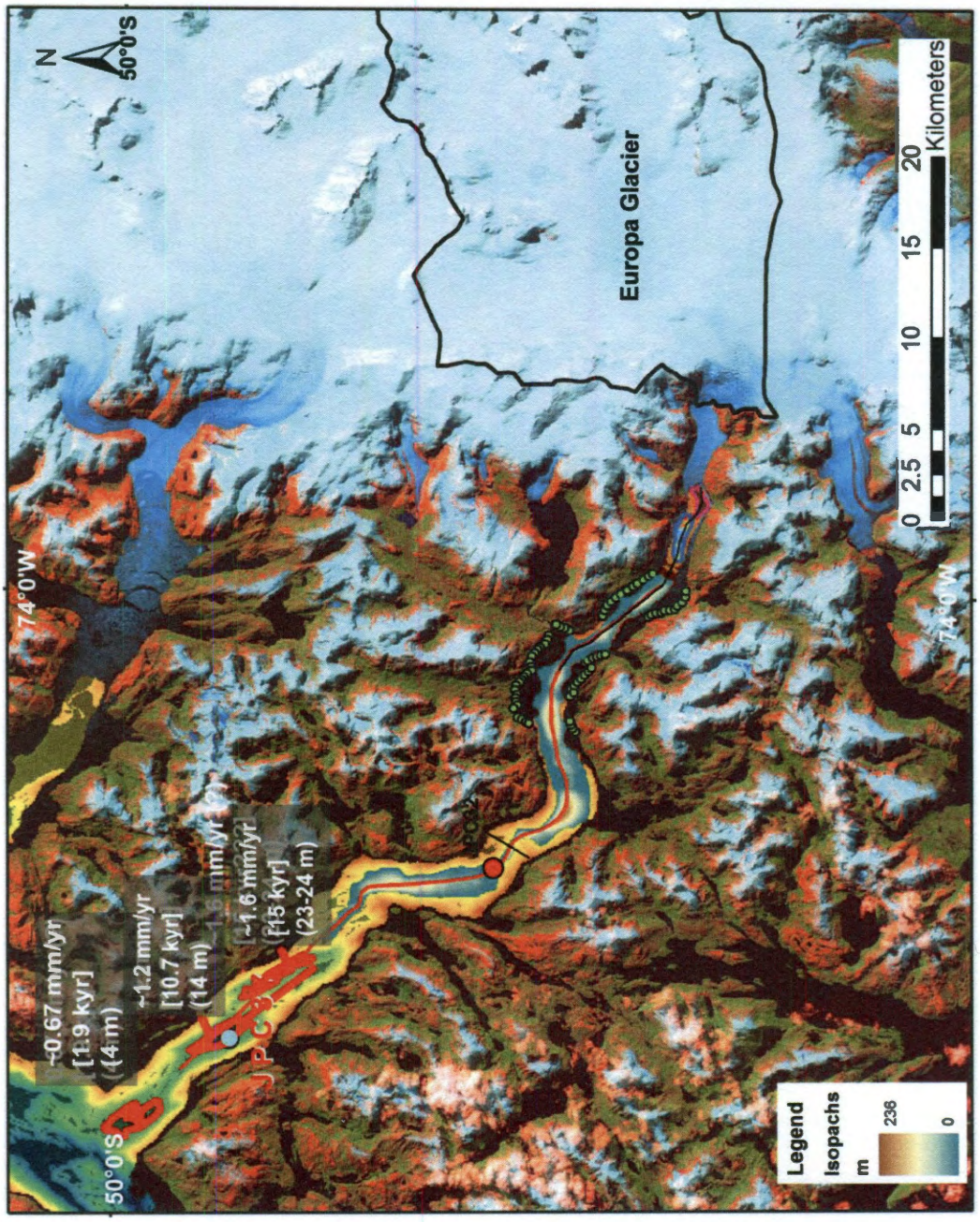

Cores and along fjor seismic lines (red) are shown.

Marinelli Glacier area:

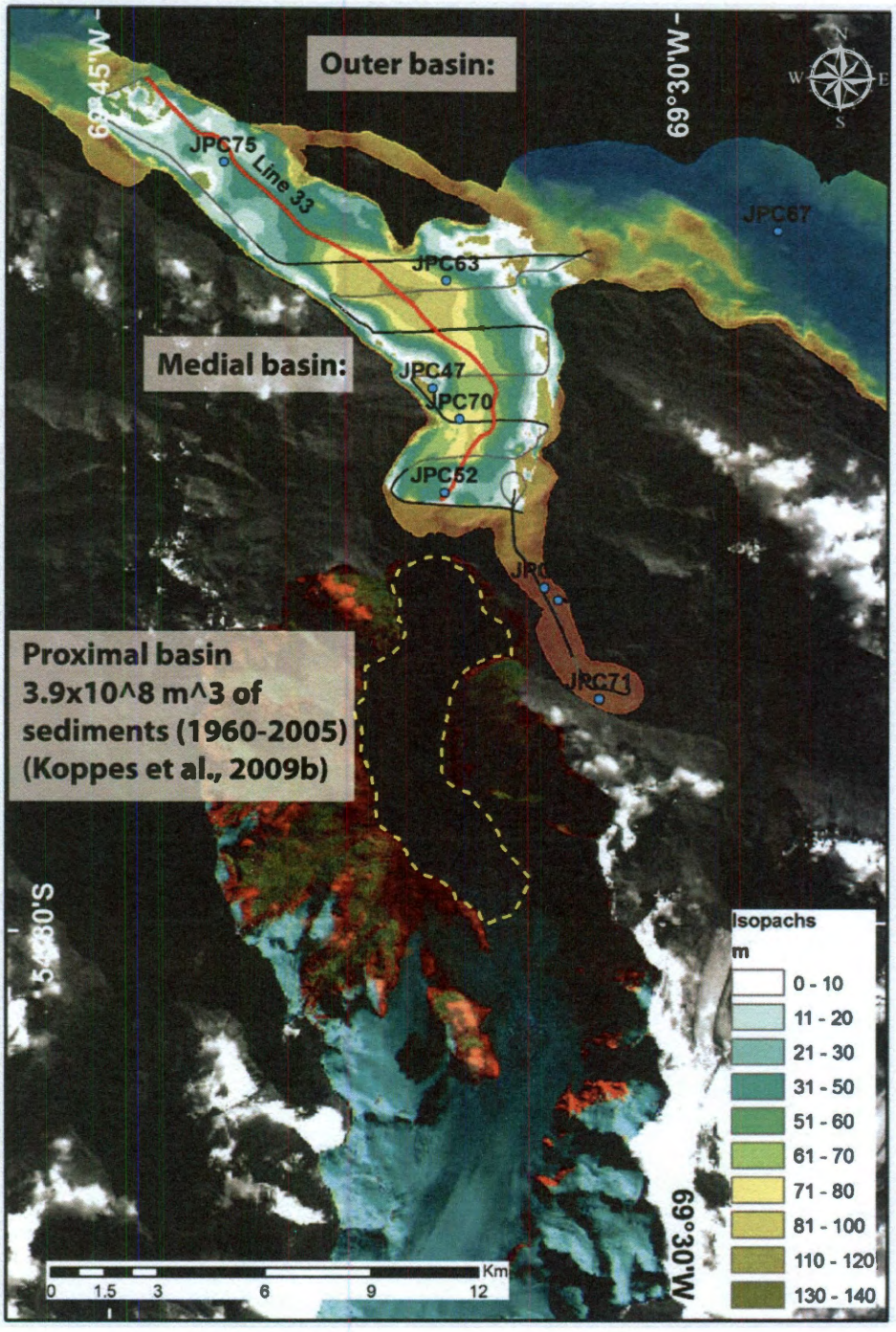

Seismic lines and cores used for the estimation of isopachs are shown.

Maxwell bay:

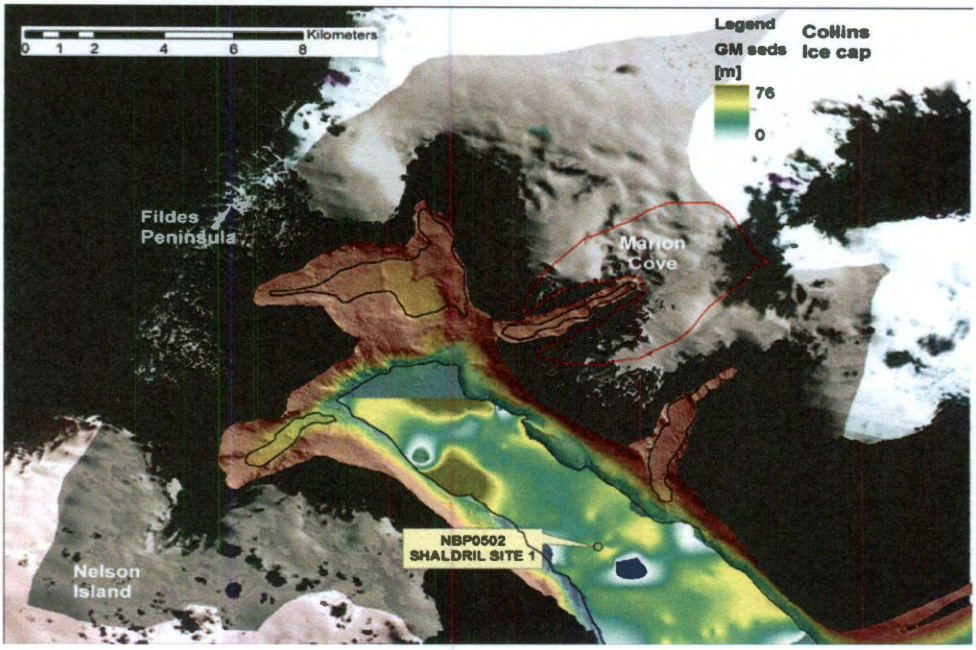

Herbert Sound:

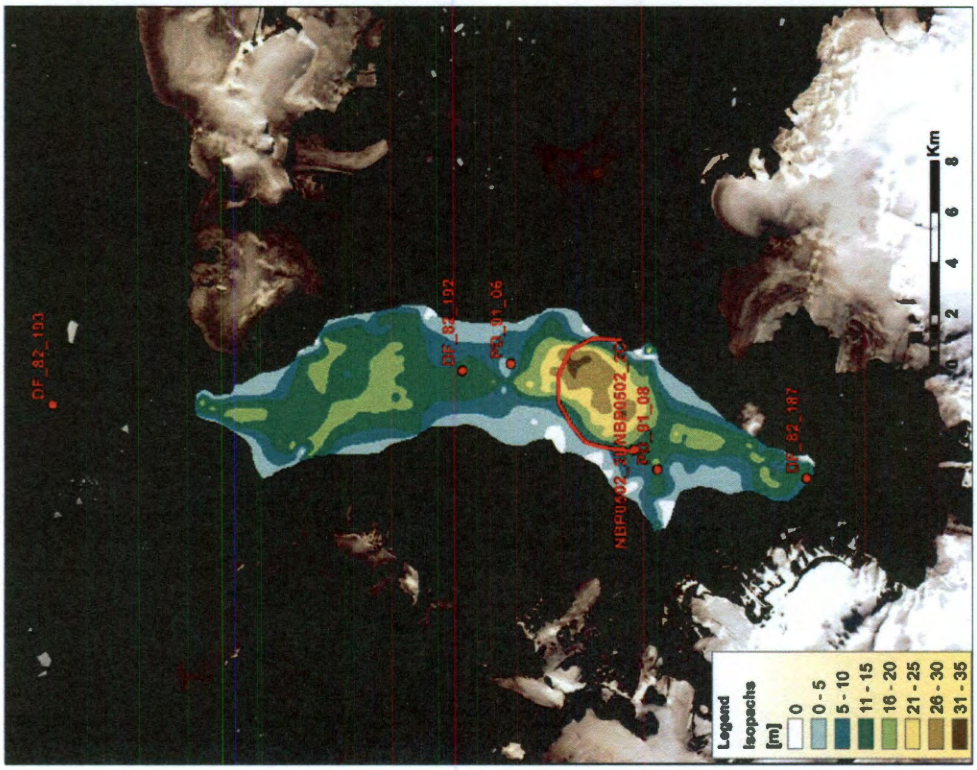

Anvord Bay:

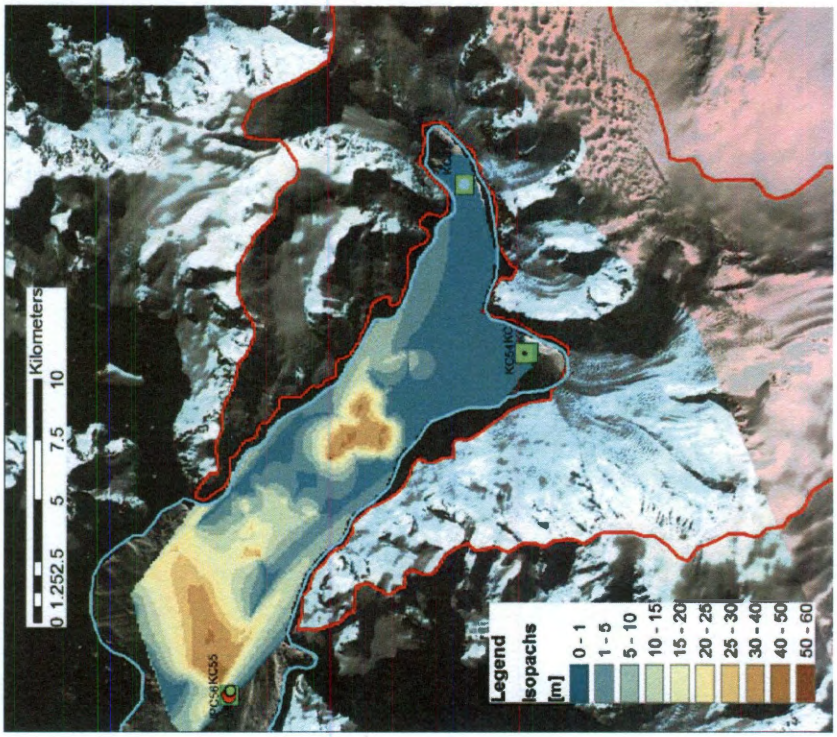

Lapeyrere Bay:

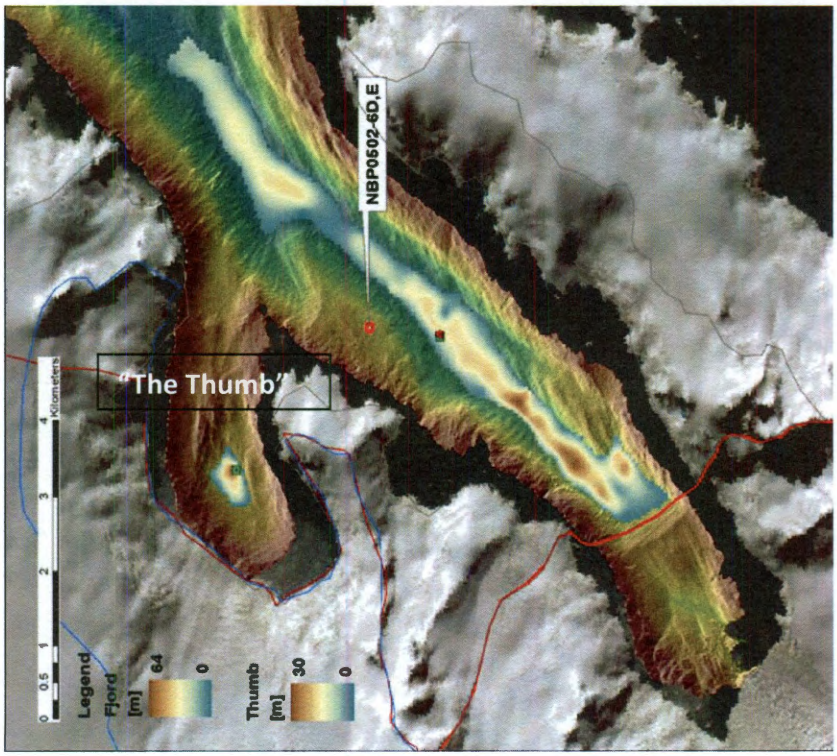

C3

This plot shows all estimated linear sedimentation rates vs the timespan they cover. Additionally, the representativeness of 2000 yr windows among the cores is shown. Representativeness is defined by the summation of all the cores that contain the 2000 yr window. If only a fraction of the interval is represented in a core, this fraction ([0 1]) is added to the summation. The no correlation of sed. rates with time span implies that the "Saddler effect" is negligible. The best representativeness correspond to the Holocene, with between 4 and 8 cores sampling any given 2000 years interval.